A LAGRANGIAN ANALYSIS OF MIDLATITUDE AIR-SEA INTERACTION ASSOCIATED WITH MEOSCALE OCEANIC EDDIES

A Dissertation

by

JESSE MATTHEW STEINWEG-WOODS

Submitted to the Office of Graduate and Professional Studies of
Texas A&M University
in partial fulfillment of the requirements for the degree of

DOCTOR OF PHILOSOPHY

Chair of Committee,	Ramalingam Saravanan
Committee Members,	Ping Chang
	John Nielsen-Gammon
	Steven Quiring
Head of Department,	Ping Yang

May 2016

Major Subject: Atmospheric Sciences

ABSTRACT

Oceanic eddies, approximately 80 km in diameter in the mid-latitude Atlantic Ocean, are frequently generated along the Gulf Stream. These eddies contain a sea surface temperature anomaly as they spin and break away from the main current. Oceanic eddies have been shown to effect the lower atmosphere in several regions in prior studies, influencing rainfall rates, cloud cover, and surface wind speeds in satellite observations. Eddy features are located using an automated detection algorithm and the atmosphere surrounding each eddy's location is studied. Coupled global and regional models, utilizing both atmospheric and oceanic components, are tested to investigate their capability of demonstrating the atmospheric response compared to observations.

It is found that the atmospheric influence of oceanic eddies is primarily limited to the boundary layer, with an exception for vertical motion influence that can extend beyond it. Eddies with a positive sea surface temperature anomaly core increase the formation of low-level clouds and rainfall slightly downstream of the eddy center, with clouds forming consistently at a height of approximately 850 hPa in models and reanalysis data. The vertical mixing mechanism is shown to be the cause of the wind response to oceanic eddy influence. This is based on a dipolar pattern of wind divergence aligning with the sea surface temperature gradient, along with a change in horizontal wind speed close to the top of the boundary layer due to vertical momentum transfer.

The results show coupled models overestimate the coupling strength between sea surface temperatures and the atmospheric response compared to observations. This indicates coupled models are capable of adequately simulating the atmospheric response, as long as the oceanic component's resolution is eddy resolving. In the regional model, parameterized convection showed a very similar result to explicitly resolving the convection. Therefore, the atmospheric response to oceanic eddies can be simulated properly even if the convection has been parameterized.

ACKNOWLEDGEMENTS

I would like to sincerely thank my advisor, Dr. Ramalingam Saravanan, for all of his support and flexibility during my time at Texas A&M. He helped guide me when I was lost, yet he trusted me enough so that I could find my own path. He has also helped craft me into a better scientist that will serve me well in my own career, especially when the time comes for me to be skeptical of results that seem too good to be true.

I also want to thank my committee members, Dr. Ping Chang, Dr. John Nielsen-Gammon, and Dr. Steven Quiring. I have learned valuable lessons from all three of you, and your constructive feedback during my time here has been most appreciated. I am very glad you all agreed to serve on my committee.

I also appreciate the constructive conversations and helpful information gleaned from Dr. Jen-Shan Hsieh and my fellow student Tarun Verma. Both of them gave great feedback to help me try new techniques when I was stuck and Dr. Hsieh was especially helpful in providing the data I needed. In addition, Dr. Gyorgyi Gyarmati was of great assistance in solving computing issues on the cluster, especially when I needed additional storage space.

I wish to thank my family and friends for the continuous support they gave me, being a good source of help whenever I was doubting myself and celebrating every small victory with me. Finally, I wish to thank my dear wife, Dr. Yangyang Liu. She has been such an incredible beacon of inspiration for me, and she has kept me going when things were hard. Knowing that I could count on her every day to be understanding and kind

means everything to me. With her at my side, getting this dissertation finished was a lot easier.

TABLE OF CONTENTS

Page

Page

LIST OF FIGURES

Page

Page

Page

LIST OF TABLES

Page

1. INTRODUCTION

1.1 Oceanic Eddies and Atmospheric Impact

Mesoscale oceanic eddies, with an approximate radius of 40 km, form most commonly along strong oceanic currents such as the Kuroshio Extension east of Japan or the Agulhas Current along Africa's southern coast. As a rotating eddy spins away from the main oceanic current, it can trap inside of itself a region of cold or warm water, depending on the direction of rotation. In the northern hemisphere, anticyclonic eddies typically contain local positive sea surface temperature (SST) anomalies of warmer water, with cyclonic eddies having negative SST anomalies of colder water.

There is a well-documented influence from SST anomalies on wind speed. This response, however, depends on the scale. On synoptic and larger horizontal scales (> 1000 km), SST and surface wind speed are negatively correlated spatially. This is due to the ocean responding to latent and sensible heat fluxes from the winds, which tend to decrease the SST as the wind speed increases (Xie 2004). However, on the mesoscale (< 1000 km), a positive correlation exists between SST and surface wind speed. This implies that spatial SST variation must be responsible (Chelton and Xie 2010). This correlation has been observed in Gulf Stream rings, where positive SST anomalies were found to increase surface winds by 10-15% compared to the background mean (Park et al. 2006). The wind response in these mesoscale features persists, even after synoptic

systems traverse through the area, and can last over time scales of at least a few weeks (Park and Cornillon 2002).

Variations in SST fronts across differing regions of the planet can even have an influence extending far beyond the boundary layer. Over the Gulf Stream in the North Atlantic, it was found that SST fronts altered vertical wind velocities existing even in the upper troposphere, and rainfall rates were also increased directly over the Gulf Stream's location (Minobe et al. 2008, Minobe et al. 2010). In the Kuroshio Extension region, the Pacific storm track is affected based on how much the Kuroshio Extension current meanders. This indicates that even smaller scale SST variability can have an impact on deep convection (O'Reilly and Czaja 2015). In the same region, X. Ma et al. (2015) found that mesoscale oceanic eddies alter convection patterns at a great distance. Rainfall variability during the winter on the Northern Pacific U.S. coast was affected by the eddies.

Although much smaller in size than SST fronts across major ocean currents, oceanic eddies have their own small fronts that can affect the atmosphere in a noticeable way. As oceanic eddies propagate, there is a clear SST signal associated with them that directly aligns with a local sea surface height (SSH) anomaly (Hausmann and Czaja 2012). This small SST anomaly associated with the eddy can impact the atmosphere surrounding its location. Frenger et al. (2013) examined these SST anomalies associated with mesoscale eddies in the Southern Ocean and observed an influence on the lower atmosphere, including changes in cloud cover, surface winds, and rainfall rates. Cyclonically rotating eddies were found to cause a local reduction in cloud cover,

surface winds, and rainfall rates, while anticyclonically rotating eddies had an opposite effect of equal magnitude (see Figure 1.1). Byrne et al. (2015) investigated the atmospheric response to oceanic eddies as well over the Brazil-Malvinas Confluence region. Their study included a coupled regional model and found that anticyclonic eddies can also increase the boundary layer height and local heat fluxes. Both studies agreed on the atmospheric response involving clouds, rainfall, and wind speed.

This atmospheric influence can even extend beyond the boundary layer. After examining eddies in the Kuroshio Extension region, J. Ma et al. (2015) found a response in a deepening boundary layer over warm eddies, with a shrinking boundary layer over cold ones. Vertical velocity anomalies were found to exist beyond the boundary layer, primarily downstream of the eddy core, and transient zonal momentum transport is enhanced up to 850 hPa. This indicates some limited influence at mid-levels, but it doesn't seem to extend to the upper troposphere.

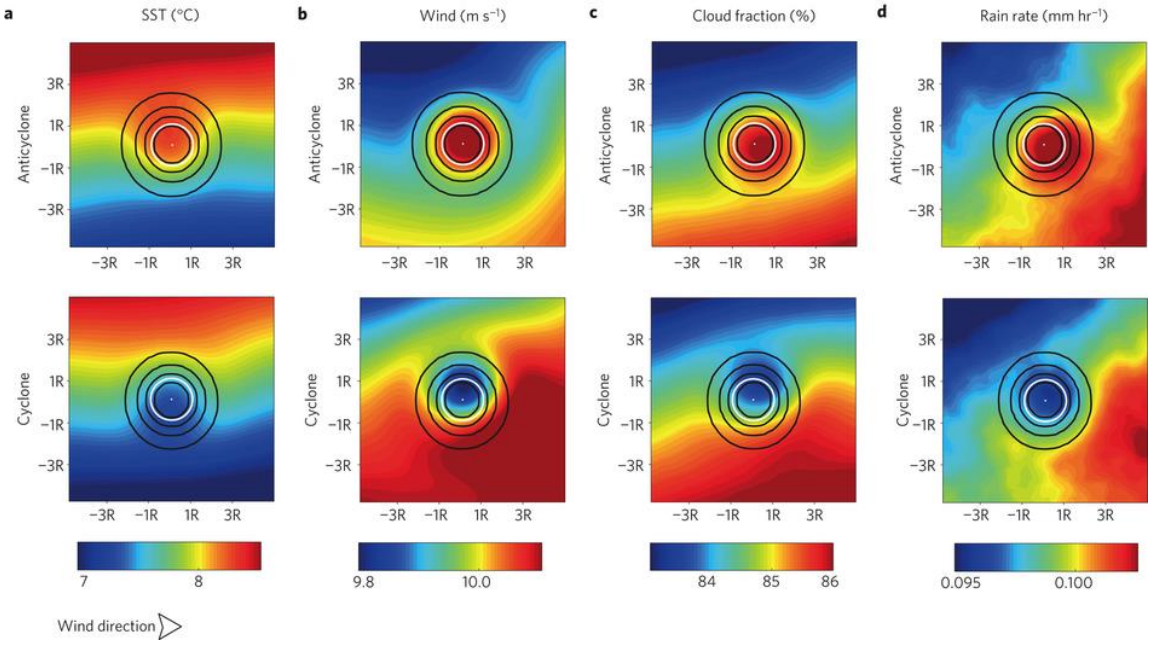

Figure 1.1. Composites of the atmosphere response to oceanic eddies by eddy type for SST, wind speed, cloud fraction and rainfall rate. The axes represent the distance from the composite center in terms of eddy radii. White circles represent the eddy core of one radius, while black circles represent sea level anomaly contours. From Frenger et al. (2013).

1.2 Oceanic Eddy Formation

Oceanic eddies tend to form along major oceanic currents, such as the Gulf Stream, Kuroshio Extension, and Agulhas Current (see Figure 1.2). Baroclinic instability and horizontal shear from the mean flow can cause eddies to form, spinning away from the main current. Most of the ocean's kinetic energy is dominated by this eddy activity (Ferrari and Wunsch 2009), given that eddies can persist on average for about a month, which is much longer compared to their atmospheric counterpart. Eddy formation can,

however, be disrupted by wind stress. This is especially true of cyclonic eddies with larger SST gradients (Jin et al. 2009).

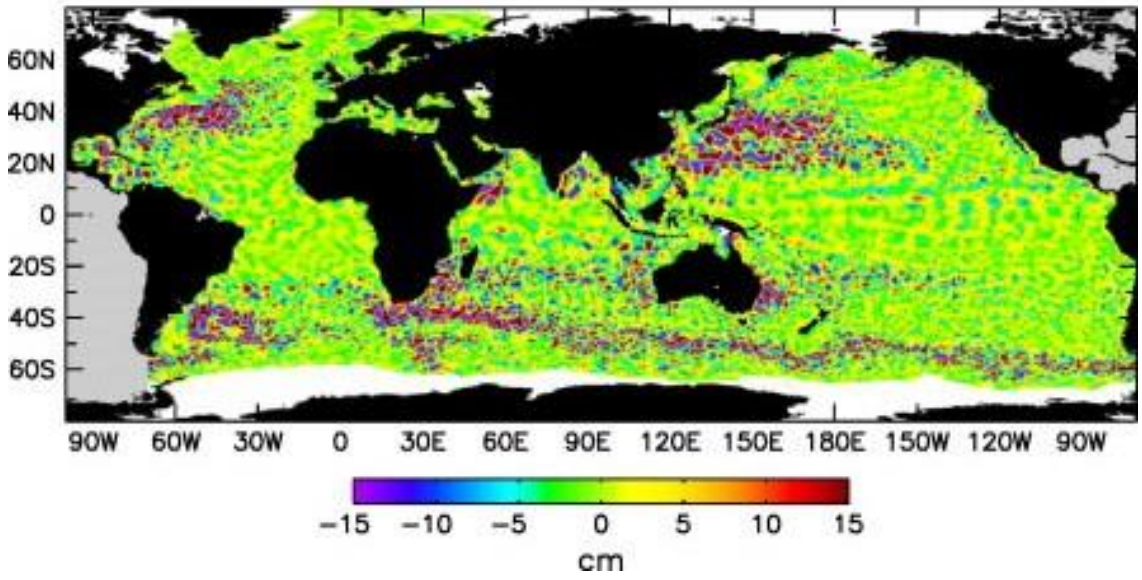

Figure 1.2. Sea surface height anomalies showing the locations of major eddy presence throughout the world's oceans. Areas with larger magnitude sea surface height anomalies are eddies in the figure. Modified from Chelton et al. 2011.

The ratio between frequencies of anticyclonic and cyclonic eddy formation can vary by region. Byrne et al. (2015) found that the two formed in even quantities in the Brazil-Malvinas Confluence. In the subtropical region of the Kuroshio Extension, cyclonic eddies outnumbered anticyclonic by about 4% (Liu et al. 2012). However, in the Gulf Stream, cyclonic eddies were found to occur more frequently than anticyclonic eddies at a rate of approximately 48% (Kang and Curchitser 2013). An example

distribution of detected eddies in the region can be seen in Figure 1.3. Anticyclonic eddies tend to be shorter lived in the region, which may explain the imbalance in eddy type frequencies. Because of this imbalance, eddies with a positive SST anomaly will be less common. This means most atmospheric influence will come from cold core eddies in the North Atlantic compared to a more even contribution by eddy type in the Kuroshio Extension region.

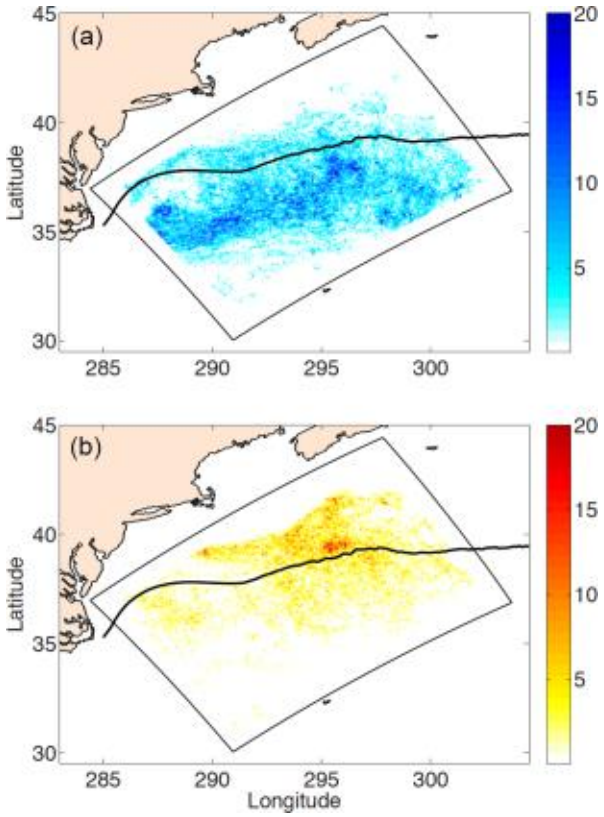

Figure 1.3. Distributions of eddies by type for (a) cyclonic and (b) anticyclonic in the North Atlantic for the period 1958-2007 in simulations. Notice that cyclonic eddies overall were more frequent. From Kang and Curchitser (2013).

1.3 Air-Sea Interaction Associated with Oceanic Eddies

How oceanic eddies will affect the atmosphere can depend partially on the environments in which they form. Yu et al. 2007 analyzed the air-sea heat fluxes for the world's oceans and found that fluxes were strongest in the Kuroshio Extension and Gulf Stream regions, while these fluxes were weaker in the Southern Ocean. This could mean eddies have a greater effect on the atmosphere where the air-sea fluxes are largest. Part of the reason for the stronger fluxes could be attributed to the greater mixed layer depths in these same regions (de Boyer et al. 2004).

The response of the atmosphere in the boundary layer to changes in SST has been well studied in several of these different regions, such as the eastern equatorial Pacific (de Szoeke and Bretherton 2004), the Gulf Stream (Song et al. 2006), the Agulhas Current (O'Neill et al. 2005 with observations and O'Neill et al. 2010 with a model), and globally (Shimada and Minobe 2011). For example, in the Agulhas Current, O'Neill et al. (2005) found that the boundary layer tended to deepen over warmer waters.

This can be explained by a wind response to the warmer SST, which decreases the stability profile of the atmosphere. Positive SST anomalies have been found to increase the boundary layer height through these changes in stability (Small et al. 2008). Negative SST anomalies can also lower the boundary layer height. An example of this was shown in Bourras et al. (2004), where a local SST minimum resulted in greater wind speeds close to the boundary layer while simultaneously reducing wind speeds at the

surface (see Figure 1.4). Other studies have observed this behavior as well (Chelton et al. 2004, Seo et al. 2008).

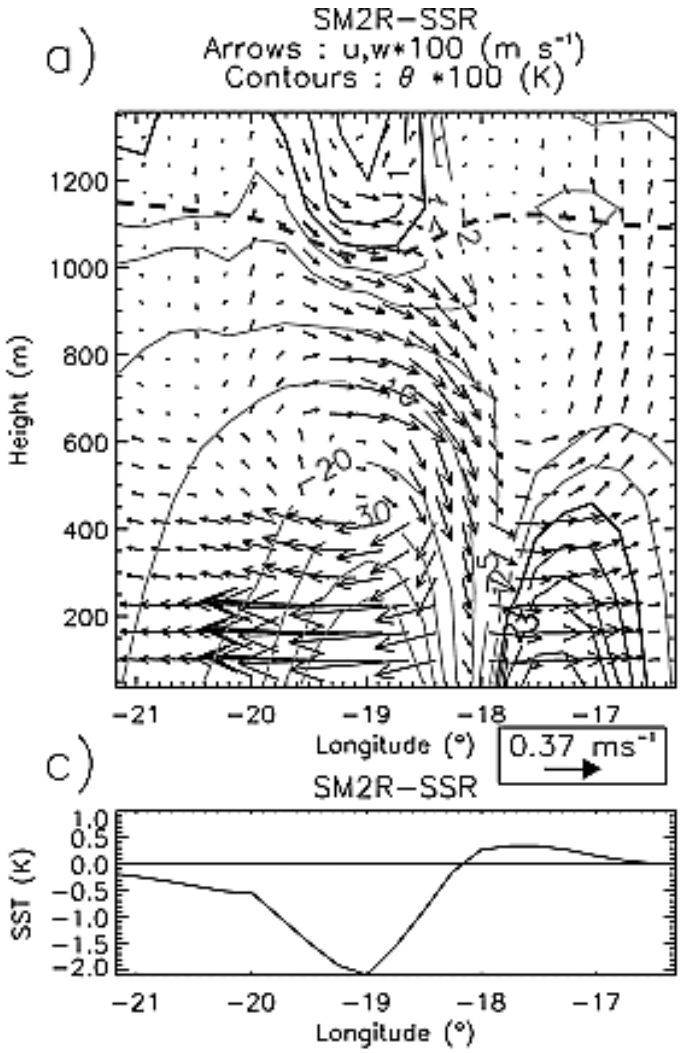

Figure 1.4. Boundary layer response to a cold core mesoscale oceanic eddy in a model simulation. The boundary layer height is indicated by the horizontal dashed line. Adapted from Bourras et al. (2004).

There has been great debate in the literature as to what exactly is the mechanism behind this wind response to SST anomalies. Studies such as Small et al. (2008) and Putrasahan et al. (2013) have posited that vertical mixing and pressure adjustment are both plausible mechanisms to explain the atmospheric response to these SST anomalies found in oceanic eddies. It was found in Lindzen and Nigam (1987) that positive SST anomalies could lead to a reduction in sea level pressure, causing convergence of winds at the center of pressure reduction.

However, Skyllingstad et al. (2007) found that turbulent mixing was primarily responsible as the atmosphere adjusted to SST anomalies. The background wind speed is thought to be more important for determining which mechanism dominates, with greater background wind speeds making pressure adjustment less likely (Spall 2007). This is similar to the results found in Shimada and Minobe (2011), where the pressure adjustment mechanism was most dominant along SST fronts where the wind was not blowing across the front.

In addition, Byrne et al. (2015) argues that the horizontal scale of the SST anomaly also plays a role. Smaller scale SST anomalies are more likely to have the vertical mixing mechanism dominate. Given the round shape of the SST fronts in mesoscale oceanic eddies, along with the small horizontal scale, the vertical mixing mechanism seems to be more applicable for mesoscale oceanic eddies than other types of SST fronts.

1.4 Impact of Eddies on Climate and Modeling Studies

To accurately model the interaction between SST anomalies and wind speed correctly, high resolutions are required. Due to their great computational requirements, most General Circulation Models (GCM) have resolutions that are not fine enough to resolve oceanic eddies. As a result, the effect these eddies can have on the atmosphere, along with other climate feedbacks, is not properly accounted for. In GCMs that are not eddy resolving, the magnitude of wind stress anomaly is underestimated (Bryan et al. 2010, Maloney and Chelton 2006), thereby not correctly accounting for heat exchange between the ocean and atmosphere (see Figure 1.5). SST coupling with wind speed and wind stress is underestimated by a factor of two to four in several models due to resolutions that are too coarse (Chelton and Xie 2010).

To address this problem, a combination of factors must be considered. Changing the planetary boundary layer (PBL) mixing parameterization was shown to alter the accuracy of coupling coefficients between SST and winds in the Agulhas Current region (Perlin et al. 2014). It is also possible that the mesoscale eddies can be parameterized if the resolution is too coarse for them to be explicitly resolved. Bryan et al. (2014) attempted to see if parameterizations were adequate compared to model results, but their results were inconclusive. In Griffies et al. (2015), mesoscale eddy parameterizations underestimated upward heat transport in the ocean compared to eddies that were explicitly resolved. This may partially explain the negative SST bias found in Delworth et al. (2012), where the SST was greater in the Southern Ocean when using a higher

resolution model. The negative SST bias can also result in negative biases of rainfall (Iizuka 2010) due to the SST being too cold compared to observations in coarse resolutions.

Having an accurate representation of the SST anomalies associated with mesoscale oceanic eddies is crucial to properly simulate the atmosphere in weather and climate models. Because of these underlying issues from underestimating wind speed, any response by the atmosphere from mesoscale SST anomalies associated with oceanic eddies will also be underestimated, as these winds have an influence on vertical mixing. In addition, feedbacks from changes in cloud cover and rainfall may also lead to inaccuracies regarding the ocean response. If the SST boundary condition is smoothed, it can cause an underestimation of storm track activity as a consequence (Taguchi et al. 2009).

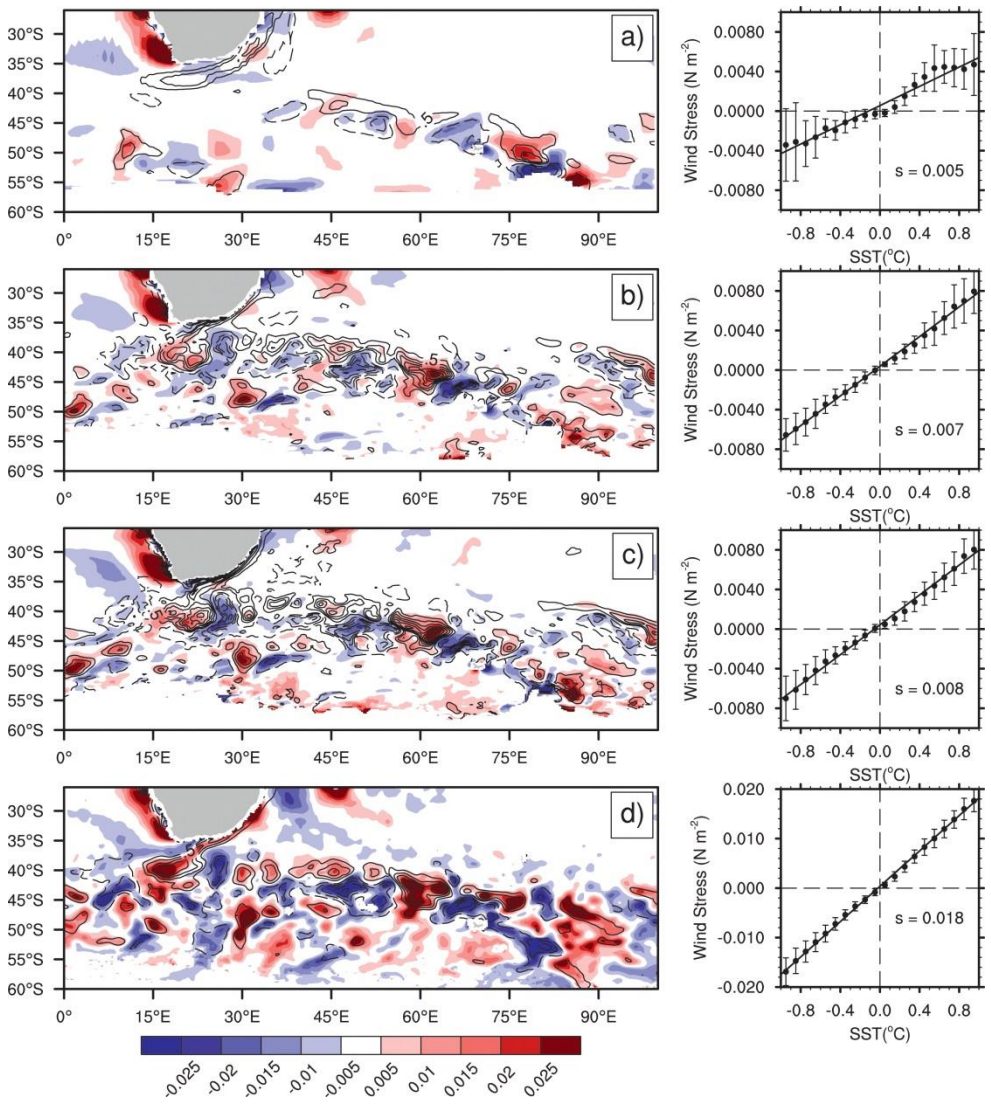

Figure 1.5. High-pass filtered wind stress (in color, N m^{-2}) and SST contours for (a) 1.0° ocean and 0.5° atmosphere, (b) 0.1° ocean and 0.5° atmosphere, (c) 0.1° ocean and 0.25° atmosphere, and (d) observations. From Bryan et al. (2010).

The overall possible effect on climate from oceanic eddies is unclear. While they are capable of locally decreasing cloud cover (Frenger et al. 2013) in the cold core case, oceanic eddies are also capable of acting as a sink for carbon by pulling phytoplankton down into the ocean (Omand et al. 2015). Both types of eddies would be capable of reducing the overall CO_2 concentration in the atmosphere, while cold core eddies would reduce cloud cover which could increase the planet's overall radiation budget. Oceanic eddies can also transport SST anomalies great distances, decreasing the temperature gradient between the poles and the equator. This area of research would require high resolution global climate models capable of simulating the eddies fully, which is computationally expensive and therefore has not been studied in great detail as of yet.

1.5 Motivation and Summary of Remaining Chapters

Because of the uncertainty regarding climate effects from oceanic mesoscale eddies, further research is required. In order to decrease the uncertainty, a GCM that can simulate the atmospheric response to oceanic eddies effectively is required first. No previous studies have investigated whether a GCM can do this correctly, especially a coupled climate model between the atmosphere and ocean at eddy resolving resolutions. Comparing the results of this model to observations would give an indication into the model's capabilities.

While several areas of the ocean have been studied for atmospheric response to oceanic eddies in great detail (Southern Ocean for Frenger et al. 2013, Kuroshio

Extension for J. Ma et al. 2015, and the Brazil-Malvinas for Byrne et al. 2015), no major study has yet focused on the atmospheric response in the North Atlantic over the Gulf Stream. It is important to ascertain whether the atmospheric response to oceanic eddies varies by region. There could be possible differences in which mechanism dominates the wind response to SST, along with the magnitude of the coupling between the ocean and atmosphere.

These other previous studies have also been focused primarily on the near-surface atmospheric influence, primarily within the boundary layer. Only J. Ma et al. (2015) has investigated beyond the boundary layer, but their study was limited to reanalysis data and did not look into the response of cloud formation or the moisture profile. It needs to be determined whether oceanic eddies have a response beyond the boundary layer, and if so how deep into the atmosphere the response is detectable.

Another question that needs further answering is what resolution of the atmospheric component of a model is necessary to properly simulate the atmospheric response. Bryan et al. (2010) showed that increasing the oceanic component of a coupled model to eddy resolving resolutions helped solve the problem of underestimating wind stress coupling. However, increasing the atmospheric component's resolution decreased the bias very little.

This study will attempt to answer these questions and fill in the gaps of previous work. The area under investigation is centered on a region bounded by 25^{o}-55^{o} N, 20^{o}-80^{o}W, which is primarily where the Gulf Stream flow is most longitudinal. Models coupled between the ocean and atmosphere are used to investigate the atmospheric

response at eddy resolving resolutions, which are at or below ¼ degree. Oceanic eddy features are identified using an eddy detection algorithm on a daily timescale. Atmospheric data are then collocated to the same location as the identified features to investigate the influence on a variety of atmospheric variables. The results of the models are then compared to satellite observations, when available. In addition, the vertical profile above the oceanic eddies is also examined to better quantify what influence these small scale SST anomalies have on the boundary layer and how far that influence extends vertically.

It is found in the study results that low-level cloud production centered at a pressure level of 850 hPa occurs consistently downstream from the eddy's center in warm core eddies. The imprint of the eddy is more easily seen for these low-level clouds than in other previous studies, given that the cloud production is investigated in both the horizontal and vertical dimensions. An increase in resolution of the atmospheric component in the coupled models seems unnecessary as long as the atmosphere resolution is at least eddy resolving.

In terms of how this work will be structured, Chapter 2 discusses the methodology in detail, such as how the eddy detection algorithm works along with which datasets were used for observation and reanalysis. Further details of the coupled models are also made available. Chapter 3 focuses on the near-surface results of the atmospheric response, comparing observational satellite data to the coupled models. Coupling coefficients between the ocean and atmosphere are also investigated. Chapter 4 discusses how far above the surface an eddy's influence exists, along with how the

regional coupled model's results compare with reanalysis data. Chapter 5 summarizes the key conclusions and offers a final discussion of remaining questions.

2. METHODOLOGY

Most previous work has focused on air-sea interactions at larger scales, such as SST fronts (Minobe et al. 2008), where the fronts are less transient than mesoscale oceanic eddies. Attempts to study this interaction at the mesoscale (Bryan et al. 2010) usually involve assessing the correlation between SST and atmospheric response averaged over a particular area of interest. Sometimes, the SST variability is simply smoothed in order to simulate the difference in atmospheric response between normal mesoscale eddy activity and little to no activity (Putrasahan et al. 2013). Although this method of research can find correlations, the resolution is limited using these spatial smoothing techniques. It is also possible that non-eddy features will be eliminated in the smoothing process, including SST fronts. In order to actually visualize the atmospheric response and understand the underlying physics at the mesoscale, greater precision is required. This involves identifying individual eddies and focusing on the atmospheric environment in close proximity to the eddy location.

In order to improve the accuracy of regional and global prediction models, understanding the interaction between the ocean and atmosphere at the mesoscale is critical. As previously discussed, even at small spatial scales, modeling this interaction correctly can help minimize bias, especially when it comes to accurately modeling the wind response to SST anomalies. It is necessary to understand how models currently simulate this interaction and how they perform compared to observations.

For this study, to investigate how well models can simulate the ocean/atmosphere interaction at small spatial scales, coupled models will be used. One is global while the other is regional. This is done mainly to ascertain whether a greater horizontal resolution in the atmospheric component of a coupled model is necessary to properly simulate the atmospheric response to mesoscale oceanic eddies.

2.1 Eddy Detection

To locate eddy features in the eastern extension of the Gulf Stream, an automated detection algorithm is preferred. A popular method for eddy detection involves use of the Okubo-Weiss parameter (Okubo 1970, Weiss 1991). This was the primary method used in Frenger et al. (2013) and Byrne et al. (2015) for identifying eddy features. However, the method is known for problems with identifying too many false positives and frequently requires smoothing of the sea level anomaly (SLA) data with respect to an annual mean to use (Yi et al. 2014), which can result in losing some of the eddies.

J. Ma et al. (2015) decided to use SST instead of SLA data to detect eddies. Their paper cites the identification method from Dong et al. (2011). This methodology looks for signatures of rotation, based on changes in direction of longitudinal and latitudinal motion, of the thermal wind. The thermal wind is derived from the SST field. However, in order to utilize the thermal wind, the SST field is first smoothed using a Gaussian smoothing technique. This has the potential of eliminating smaller eddies as well, unfortunately. In addition, the SST field can be quite noisy compared to the SLA field,

since SST fronts and other small scale features can lead to false positives in detection of eddies. The SLA field has a more direct physical response to eddy formation, and therefore is less likely to include erroneous features.

Ideally, it would seem best to use a detection algorithm that does not require preprocessing of the data and can also distinguish separate eddy features that are in close proximity to one another. That is why this study utilizes an adaptation of the algorithm developed in Faghmous et al. (2012) called 'EddyScan.' Similar to Chelton et al. (2011), it utilizes thresholds of connected SLA contours to detect closed features. The thresholds are done in 1 cm steps from -100 cm to +100 cm, which allows eddy features surrounded by a larger amplitude background to be detected successfully. In order to be considered an eddy feature, the algorithm requires a minimum pixel size of nine and a minimum amplitude of 1 cm. The feature must contain a minimum/maximum. In addition, the algorithm takes into account the convexity of the detected features. This allows a separation of eddies close together so that they are not erroneously identified as a single detected feature. An example of this is shown in Figure 2.1.

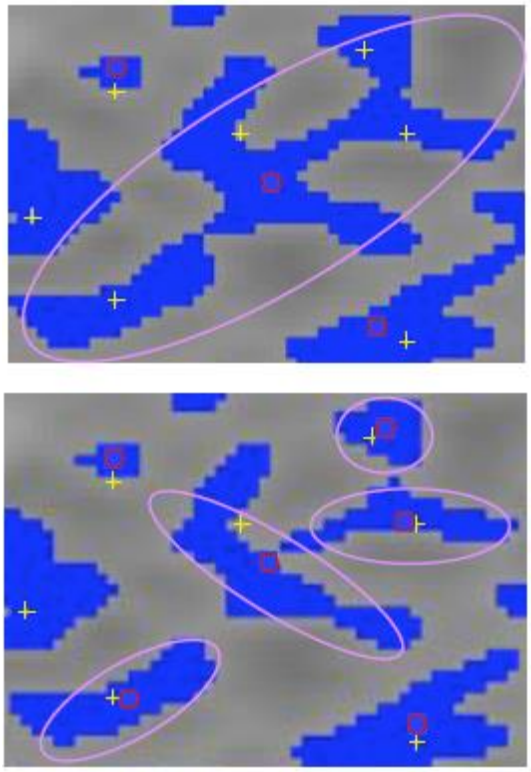

Figure 2.1. An example of the convexity criterion in "EddyScan." The top portion shows a detected feature without the convexity requirement. The bottom portion shows a successful application of the convexity parameter, which separates the detected feature into four separate eddies. From Faghmous et al. (2012).

The algorithm needed to be customized, however, in order to get an optimal result. An initial problem was that the algorithm's minimum amplitude of 1 cm was far too sensitive. Instead of only detecting eddy features near the Gulf Stream, a large number of eddies were also detected far away from any major ocean current. Since eddies from along major ocean currents, these detected features are most likely noise and are undesirable. To correct for this, the minimum amplitude was originally increased

from 1 cm up to 10 cm. While this initially corrected the problem, there were still too many eddies being detected. Since anticyclonic eddies tend to be larger than cyclonic eddies, the minimum amplitude threshold of an eddy feature was increased to 10 cm for any features larger than 75 pixels, increasing along a sliding scale up to a maximum of 25 cm as the size decreased below 75 pixels. This was done to allow the larger, anticyclonic eddies to remain after filtering while reducing noise from smaller cyclonic eddy features.

This seemed to improve things, yet smaller eddies were still being missed in sample timesteps. The minimum eddy size was decreased from the standard nine pixels to five pixels, which successfully allowed small eddies with strong SLA amplitudes to pass through the filter. The combination of changing the minimum amplitude settings along with the minimum pixel count resulted in far fewer eddies along the coastline as well. This was a problem with the 'EddyScan' algorithm, which was admitted by the authors in Faghmous et al. (2012). The simplest method for dealing with false positive eddies close to the coast was to simply remove any that had a recorded center there. An example of the algorithm's final tuned detection process can be seen in Figure 2.2.

These parameters were tuned on observational satellite data of SLA, with these same settings used in the coupled model results as well for a standardized comparison between datasets. The output from all model results was regridded to the same grid as the observational data before running the detection algorithm (0.25^{o}x0.25^{o}). This was necessary due to the tuning of parameter settings being done on SLA data at this resolution.

Finally, the eddy centers detected by the algorithm were readjusted to the local maximum of minimum of SLA. Sometimes the algorithm would detect an eddy center not located at the local SLA maximum or minimum inside of a detected feature's bounding box, so this adjustment was done to better locate the eddy's center of rotation. This technique proved helpful for rotating the eddy composites as discussed later in Chapter 3.

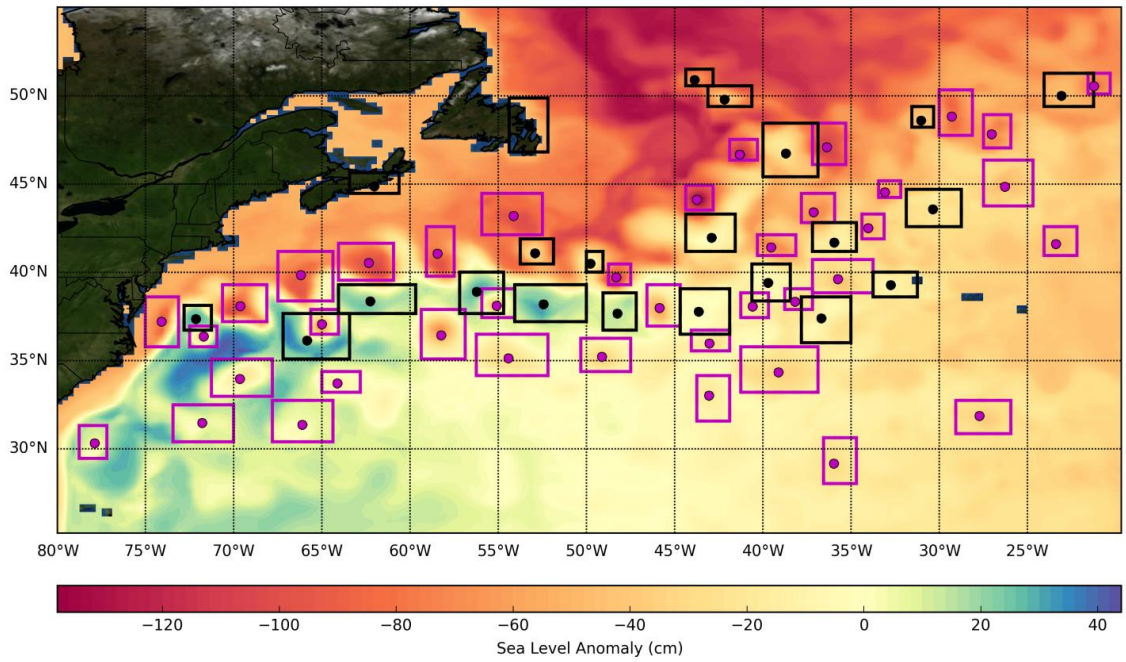

Figure 2.2. An example of the eddy detection algorithm from sea level anomaly data on January 1, 2006 inside the study domain. Anticyclonic eddies containing positive sea level anomalies are highlighted with black boxes, while cyclonic eddies with negative sea level anomalies are highlighted with magenta boxes. The detected eddy center is indicated by a small circle inside each box. Eddies erroneously detected too close to land were removed in the final calculations.

2.2 Models

The first model comes from the Community Earth System Model (CESM). It utilizes the Community Atmospheric Model version 5 with a spectral element for the dynamical core over a global domain. This is then coupled to the Parallel Ocean Program (POP2) model for the oceanic component. The atmospheric component has grid spacing of ¼ degree, while the oceanic component has grid spacing at 1/10 degree. There are 30 vertical levels in the atmosphere, with 60 vertical levels in the ocean (Small et al. 2014).

The run was done for 100 years starting at year 2000 ("present-day") greenhouse gas conditions. However, the data being investigated for this study comes from the date range of March 2, year 45 to October 1, year 49 due to daily temporal frequency output being saved in this time period, but with very limited vertical levels available. The unusually high resolution for a global GCM in this run provides the ability to investigate oceanic mesoscale eddies when most model runs are at too coarse of a resolution to be eddy resolving.

The second model experiment involves a coupling of the Weather Research and Forecasting model (WRF) with the Regional Ocean Modeling System (ROMS) for the oceanic component (Shchepetkin and McWilliams 2005). There were two separate runs, with both runs being completed by Dr. Jen-Shan Hsieh at Texas A&M University. The first involved both the ROMS and WRF components having a grid spacing of 9 km, while a second run included an inner nest for WRF of 3 km. The WRF component had 28 vertical levels, while the ROMS component had 50 vertical levels. The planetary

boundary layer scheme employed was the Yonsei University (YSU) scheme (Hong et al. 2006). Both runs took place in the date range of December 1, 1981 to April 1, 1982. The domain area for both components, along with the 3km nest, can be seen in Figure 2.1. Initial and boundary conditions for both runs in the WRF model used NCEP Reanalysis (R2) data (Kanamitsu et al. 2002). For ROMS, initial conditions were a monthly mean from the Simple Ocean Data Assimilation (SODA) dataset (Carton et al. 2000). Lateral boundary conditions used the annual mean instead. A winter run was done due to stronger ocean/atmosphere coupling. This is caused by greater wind magnitudes and a decrease in vertical stability during the winter months (Putrasahan et al. 2013).

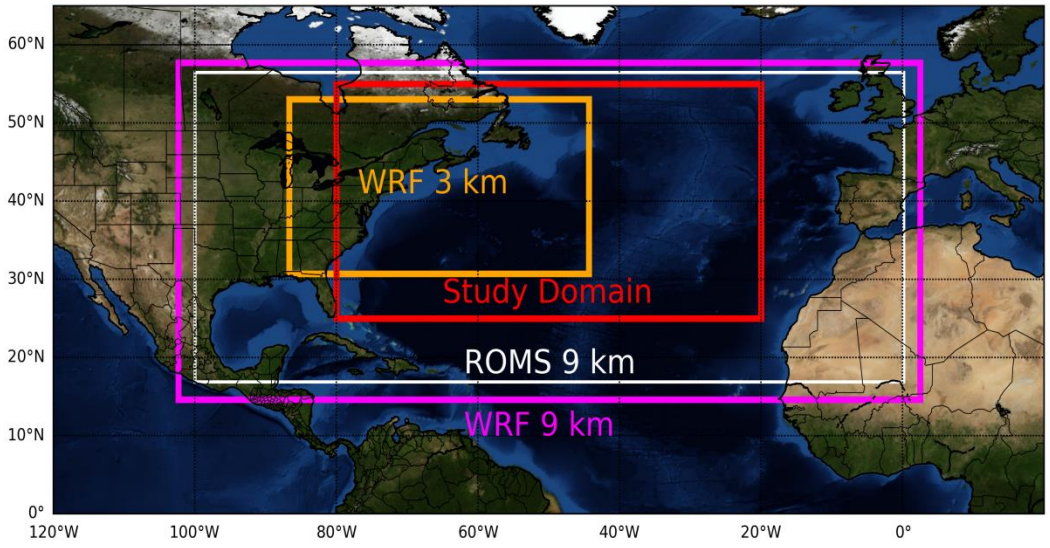

Figure 2.3. The domains of the WRF 9km, ROMS 9km, and WRF 3km nest are shown. The domain used for the study is shown in the red box.

2.3 Surface Observations and Reanalysis Data

To validate the output of the coupled models, satellite observations of the surface were used when available. The SLA data used for eddy detection comes from the Archiving, Validation, and Interpretation of Satellite Oceanographic (AVISO) dataset at ¼ degree horizontal resolution and daily temporal resolution. The SST data comes from the Reynolds' SST dataset (Reynolds et al. 2002). Rainfall data is from the Tropical Rainfall Measuring Mission (TRMM) satellite, product 3B42. Winds at a height of 10 meters come from the Cross-Calibrated Multi-Platform (CCMP) wind product (Atlas et al. 2011). Radiative cloud fraction data is from the Level-3 Aura/OMI daily global TOMS-Like Total Column Ozone gridded product (OMTO3e) from the OMI science team.

All of these datasets were chosen due to having a common horizontal resolution and daily temporal resolution, except for the CCMP winds which are every six hours. They are also available throughout the entire domain investigated in this study, with the exception of rainfall data from TRMM that is only available up to 50^{o}N. Since different products are only available at specific time periods, a 5-year period of alignment was chosen, encompassing the date range of January 1, 2006 to December 31, 2010.

For the response in the vertical, reanalysis datasets are used to validate the output from the coupled regional model runs. Two different datasets were used as a comparison. The first is the Climate Forecast System Reanalysis (CFSR) dataset (Saha et al. 2010). With a horizontal resolution of 0.5 degrees, it is not quite eddy resolving but is close compared to more coarse alternative reanalysis datasets available. It also has 37

pressure levels available, allowing a high-resolution comparison to WRF results in the vertical dimension. The model used in CFSR employs a non-local vertical diffusion scheme within the planetary boundary layer. Available until the end of 2010, the same 5-year period of alignment used for the observational surface data is also used here.

The second reanalysis dataset utilized comes from the Year of Tropical Convection (YOTC) project (Waliser et al. 2012). Although its time span is quite limited (May 2008 to April 2010), it is of a slightly greater horizontal resolution than the CFSR data at a grid spacing of 0.219° x ~0.225° and 25 pressure levels, which is now eddy resolving. This data should provide an increased spatial resolution at the expense of a smaller time range. The model used in YOTC is based on the European Center for Medium-Range Weather Forecasting (EMCWF) model, which utilizes a K-diffusion turbulence closure above the surface layer (Köhler et al. 2011). A summary of all datasets used in the study is provided in Tables 2.1 and 2.2.

Source	Time Range	Spatial Resolution	Temporal Resolution	Observed Variable
AVISO	Jan 2006 – Dec 2010	0.25^o	Daily	SLA
TRMM	Jan 2006 – Dec 2010	0.25^o	Daily	Rainfall
OMI/Aura	Jan 2006 – Dec 2010	0.25^o	Daily	Cloud Fraction
Reynolds'	Jan 2006 – Dec 2010	0.25^o	Daily	SST
CCMP	Jan 2006 – Dec 2010	0.25^o	Every 6 hours	Surface Winds

Table 2.1. A summary of the observational datasets used in this study.

Dataset	Time Range	Spatial Resolution	Temporal Resolution
CSEM Coupled Model	Jan 2006 – Dec 2010	0.25^oatmosphere, 0.1^o ocean	Daily
WRF/ROMS Coupled Model	Jan 2006 – Dec 2010	9 km (3 km nest) atmosphere, 9 km ocean	Every 2 hours
CFSR	Jan 2006 – Dec 2010	0.5^o	Every 6 hours
YOTC	May 2008 – Apr 2010	0.219^o x 0.225^o	Every 6 hours

Table 2.2. A summary of the model and reanalysis datasets used in this study.

2.4 Distribution of Detected Eddies

Although SLA data was used to identify eddies, the SST anomaly of the eddy core is what really influences the atmosphere and determines the magnitude of the air-sea interaction. Anticyclonic eddies usually have a positive SST anomaly, while cyclonic eddies usually have a negative SST anomaly. The reason for this is due to the direction of rotation usually associated with eddy formation. The Gulf Stream is oriented latitudinally from west to east, but sometimes the current can be pushed north or south due to winds, baroclinic instability, and other factors. If the current turns south, it can entrap colder waters north of the current, with a cyclonic rotation that is eventually "pinched" off. If the current turns north, it can entrap warmer waters south of the current, with a rotation that is anticyclonic. A schematic diagram demonstrating this process is shown in Figure 2.4.

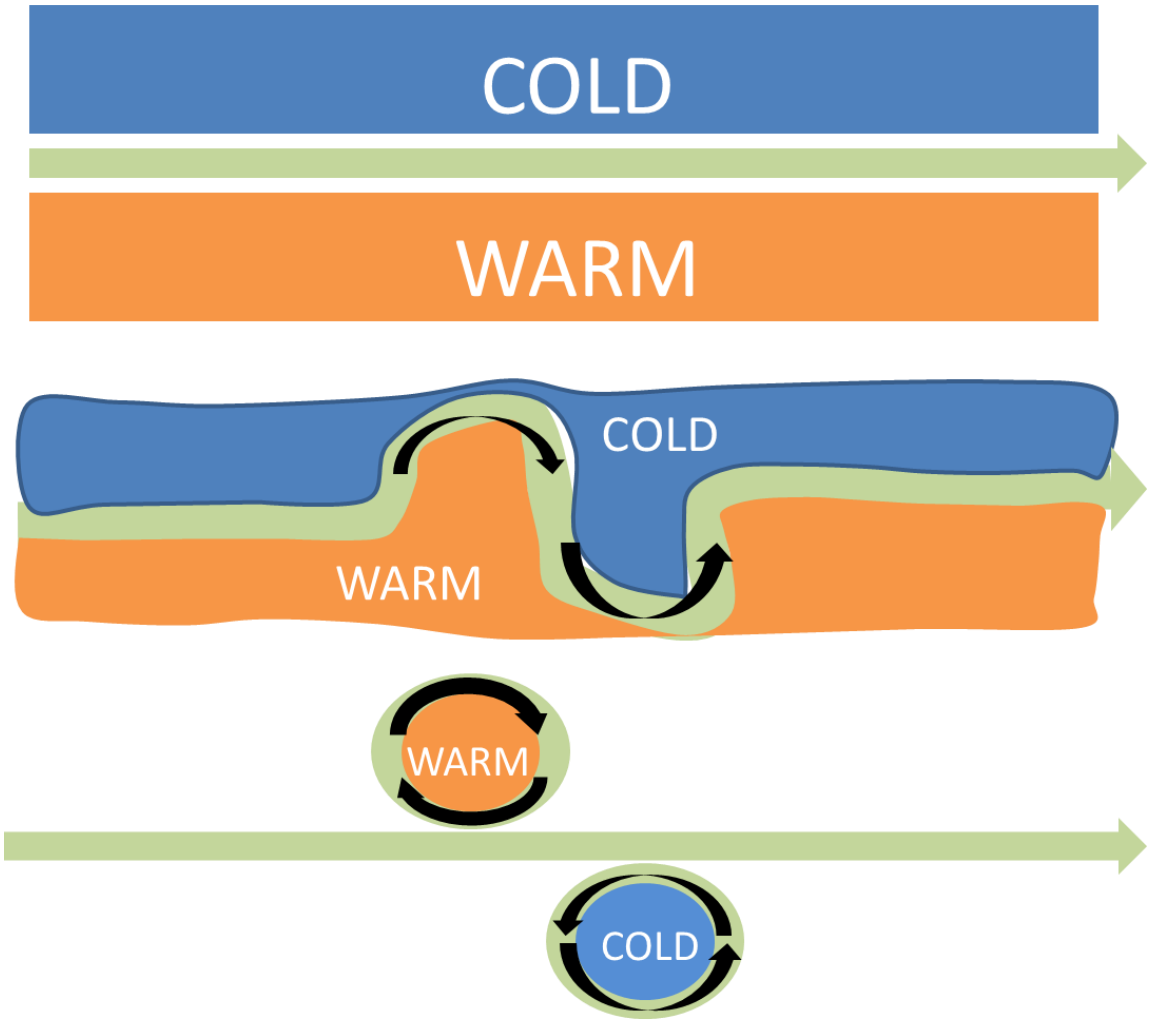

Figure 2.4. An example of the eddy formation process. The current begins with colder water to the north separated by warmer water to the south in the Northern Hemisphere. As the current beings to fluctuate, some of the water becomes trapped, and portions of the current can become constrained as bends in the current come closer together. Finally, an eddy forms, with an area of warmer or colder SST trapped inside due to the centripetal forces of rotation.

For each of the four datasets (observations, CESM, WRF 9 and WRF 3), the detected eddies were collocated with SST to determine whether the eddy had a warm or cold core. The magnitude of the SST anomaly inside each eddy is plotted in Figure 2.5. While there were a few exceptions, the vast majority of anticyclonic eddies had positive SST anomalies, while most cyclonic eddies had negative SST anomalies. The SST anomaly magnitude had more variation in the case of anticyclonic eddies than cyclonic eddies, with the greatest amount of variance found in the WRF 3 run. This could simply be due to the fact that the WRF runs were only for the winter months, while the observations and CESM had a timespan of multiple years. The WRF runs also had eddies with stronger SST anomalies overall than the CESM and observations. In the next chapter, these detected eddy features will be utilized to better understand the atmospheric response in close proximity to the eddy's location.

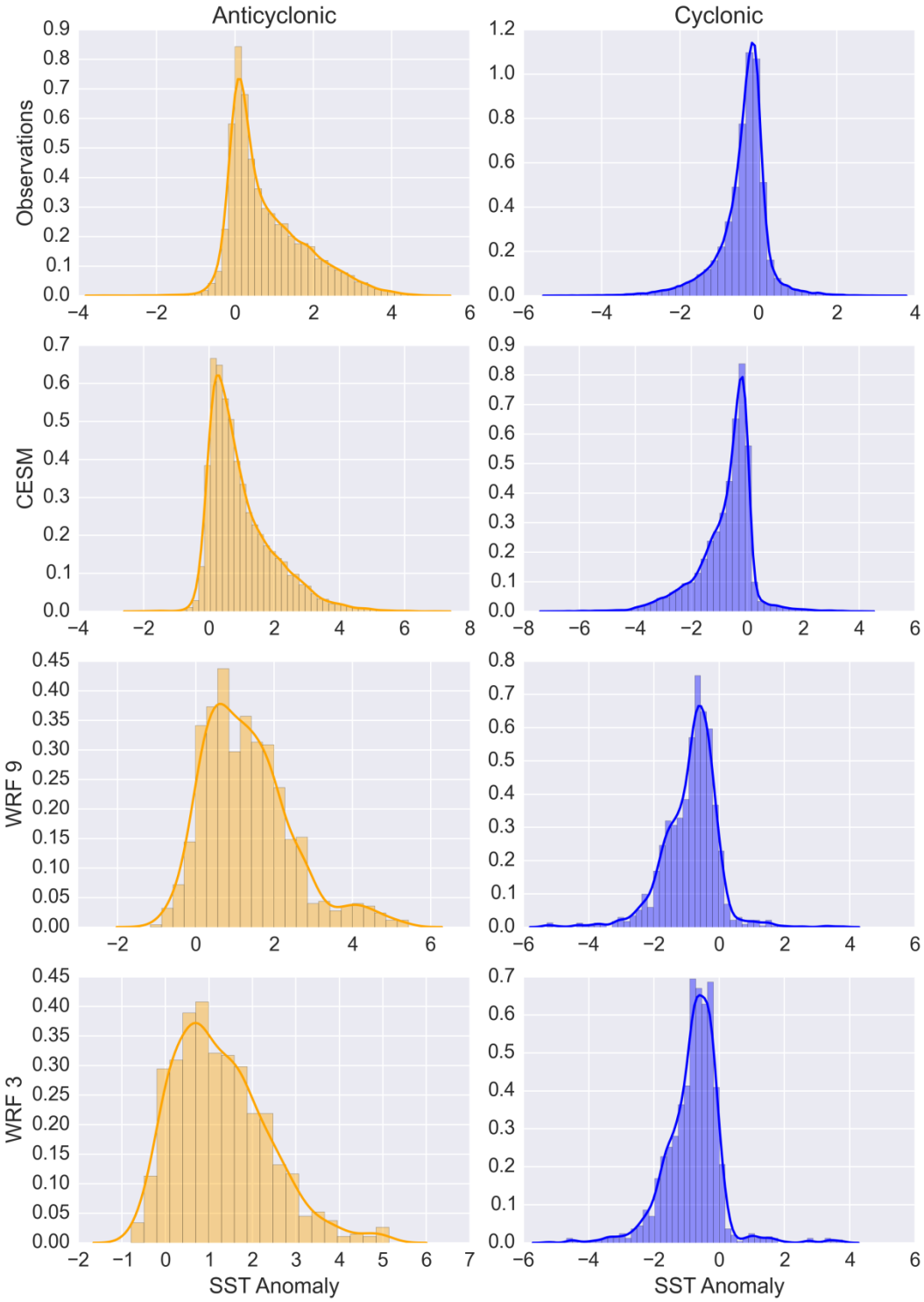

Figure 2.5. Histograms of SST anomaly by eddy type for observations and coupled models.

3. NEAR-SURFACE ATMOSPHERIC RESPONSE

This chapter will focus on the atmospheric response to oceanic eddies near the surface. In the work of Frenger et al. (2013), anticyclonic eddies in the Southern Ocean, typically having a positive SST anomaly core, increased cloud cover, rainfall, and surface winds. Cyclonic eddies, with a negative SST anomaly core in most cases, had an opposite effect. Similar results were also found in Byrne et al. (2015) and J. Ma et al. (2015) in the Brazil-Malvinas Confluence region and Kuroshio Extension respectively. It was also found in all three studies that the primary mechanism causing the surface wind response to SST was the vertical mixing mechanism. This was due to a dipolar SST gradient along-flow component pattern that overlapped with a similar wind divergence pattern, indicating convergence was not occurring due to pressure adjustment. This behavior, however, has yet to be studied for the North Atlantic region.

In order to determine what effect oceanic mesoscale eddies have upon the atmosphere in the North Atlantic, composites of the mean atmospheric profile surrounding the eddy's location can be calculated. This will reveal how the atmospheric response differs depending upon whether the SST anomaly in the eddy center is positive or negative, in addition to the magnitude of the response. It will also show whether the GCM and regional coupled models are capable of simulating the same response found in observations. The composites can also reveal whether model resolution changes the coupling strength of the SST anomaly inside the eddy core with the atmosphere above.

3.1 Surface Composite Methodology

Using a technique similar to Frenger et al. (2013), a mean composite was calculated showing the average spatial distribution of atmospheric variables in the same location as the oceanic eddies. Initially, an eddy radius has to be calculated for each detected feature. To do so, there are a few steps. First, the bounding box coordinates for a particular eddy detected from the algorithm are inspected. Once the eddy has been re-centered (see section 2.1 for further details), the maximum and minimum values of SLA inside the eddy's bounding box along the same latitude and longitude axes as the eddy center are obtained, depending upon whether the eddy in question is labeled anticyclonic or cyclonic. The minimum number of grid points necessary to "travel" outwards from the eddy center until the midpoint between the maximum and minimum of SLA has been reached is considered the eddy radius in both the latitudinal and longitudinal directions. This is done because most eddies have an elliptical shape that is not perfectly round. Given the relation between the area of a circle and the area of an ellipse, we can calculate an "equivalent" sized radius as

$$r = \sqrt{ab}$$

where a and b are the number of grid points outward in both directions from the eddy center to the midpoint value of SLA. Once this eddy radius has been calculated, a new

square bounding box of four eddy radii is drawn outwards from the eddy center. This becomes the coordinate range used for our initial atmospheric composite.

After the new bounding box coordinates have been obtained, atmospheric data and SST inside of the box's location are then rotated based upon the mean lowest level wind direction inside of the box's domain. This is done to see the upwind and downwind effects of the atmospheric response, which would not be possible if the composites were averaged normally without any rotation. Last, the data are interpolated to a common sized box and the overall mean composite is calculated.

To allow a comparison between the observations and model results, the zonal mean is subtracted from the final composite box along each row, somewhat similar to a technique utilized in J. Ma et al. (2015). This allows the magnitude of the anomaly caused by the oceanic mesoscale eddy's imprint to be more easily quantified in comparison between datasets. Subtracting the zonal mean wasn't necessary for Frenger et al. (2013), as they were investigating observations only. A consequence of subtracting the zonal mean across the entire box, however, is that positive anomalies found in the center of the box can also introduce negative anomalies on either side of the center and vice versa. These are an artifact that can affect the interpretation of the results, but subtracting this zonal mean is necessary since the local environments generated by the model output may be different from observations.

In order for the comparison among the model results and observations to be standardized, only eddies occurring in the winter months (December-March) are calculated in the composite since the two regional WRF/ROMS runs were limited to this

time period. Any calculations involving rainfall are limited to the WRF 3 km inner nest domain, as convective parameterizations were turned off during this run inside the nest. This allows total rainfall to be calculated among the four datasets equally, as rainfall in the two WRF runs is the sum of the convective and non-convective rainfall instead of a single total. Boundary effects outside of the 3 km nest would have caused an issue in summing these totals.

For the eddy composites to be compared by type, they were separated based on a warm core/cold core dichotomy. To be categorized, the mean zonal SST anomaly was calculated inside of a square box one eddy radius outwards from the composite center. If this mean anomaly located over the eddy core was positive, the eddy was categorized as warm core and vice versa. The composites were then averaged together based on this separation.

The distributions of detected eddy radius for winter months (December – March) given this dichotomy of warm core and cold core are shown in Figure 3.1. Using the equivalent sized radius technique, the results show that features most commonly have a radius of two grid points, or approximately 56 km after converting the ¼ degree grid spacing to kilometers. Features with a radius of approximately 83 km and 111 km were more frequently seen in warm core eddies than cold core eddies, so overall warm core eddies are slightly larger on average in size. No eddies detected had a size larger than six grid points, or approximately 167 km. The overall mean was approximately 70 km for warm core and 61 km for cold core.

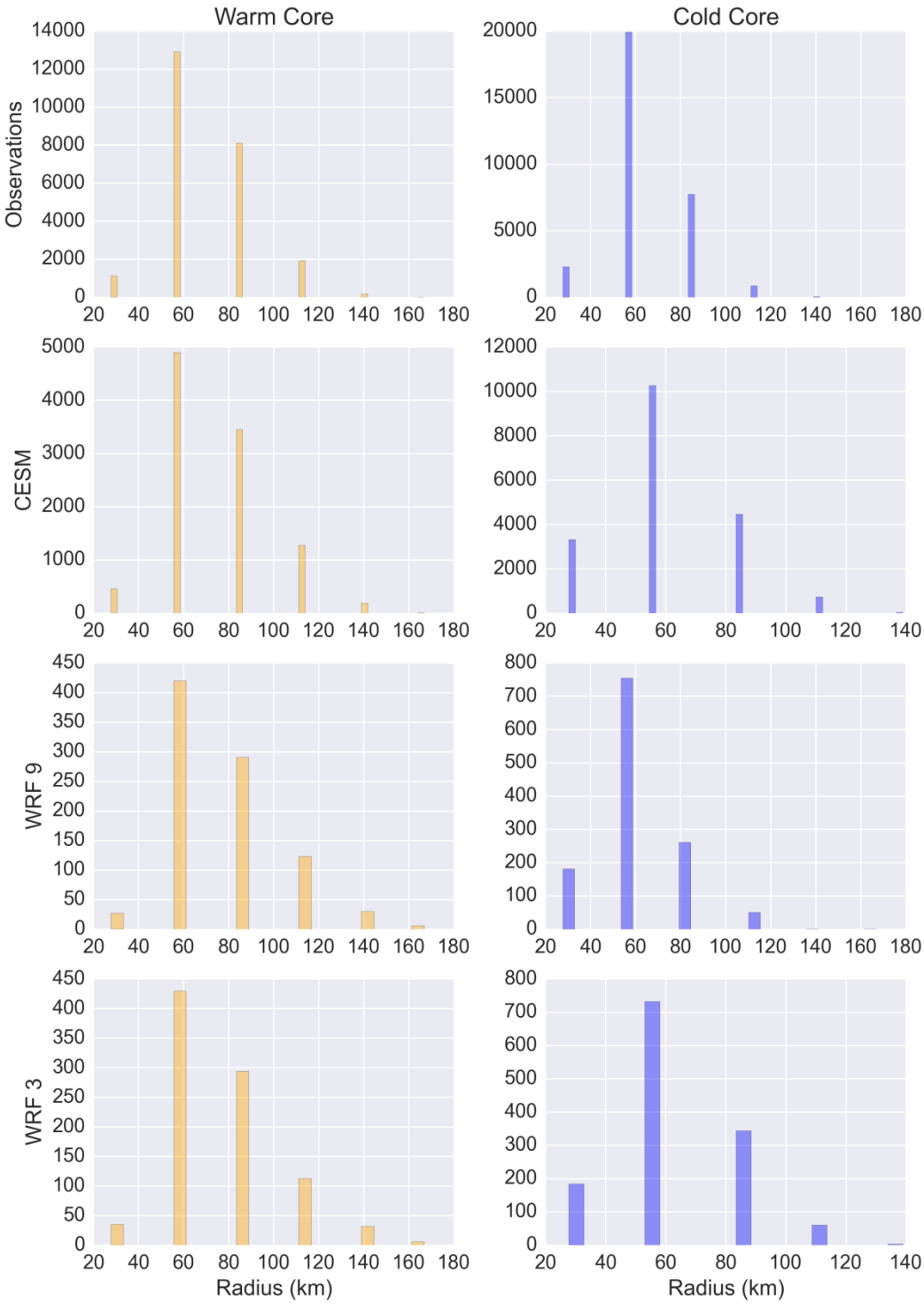

Figure 3.1. Distribution of detected eddy radius for the winter months of December-March by eddy type. The radius was converted to kilometers by an approximation of 111 km/degree.

Investigating the speed of the background wind these eddies are found in can help reveal if there are any inherent differences by eddy type. Figure 3.2 shows the distribution of background wind at the surface, where the background wind is defined as the mean inside the outer two-radius edge of each four eddy radius composite box. The background wind is very similar between eddy types, with the most common background wind speed being 7-9 m/s for both types. On average, background mean wind speeds were slightly higher in the warm core eddy environments of 10.5 m/s across observations and models, with cold core eddy environments having a mean wind speed of 10.1 m/s. Therefore, the background wind near eddies is not a significant factor in the difference between eddy types.

3.2 Coupling Coefficients

Using the same basic technique of calculating the mean zonal anomaly of each eddy composite, a linear relationship can be found between the SST anomalies and anomalies of other atmospheric variables inside the one eddy radius center. To do this, a straight-line ordinary least squares fit of the relationship between SST anomalies and atmospheric anomalies was calculated. Similar to J. Ma et al. (2015), the fits were tested for statistical significance using the F-test.

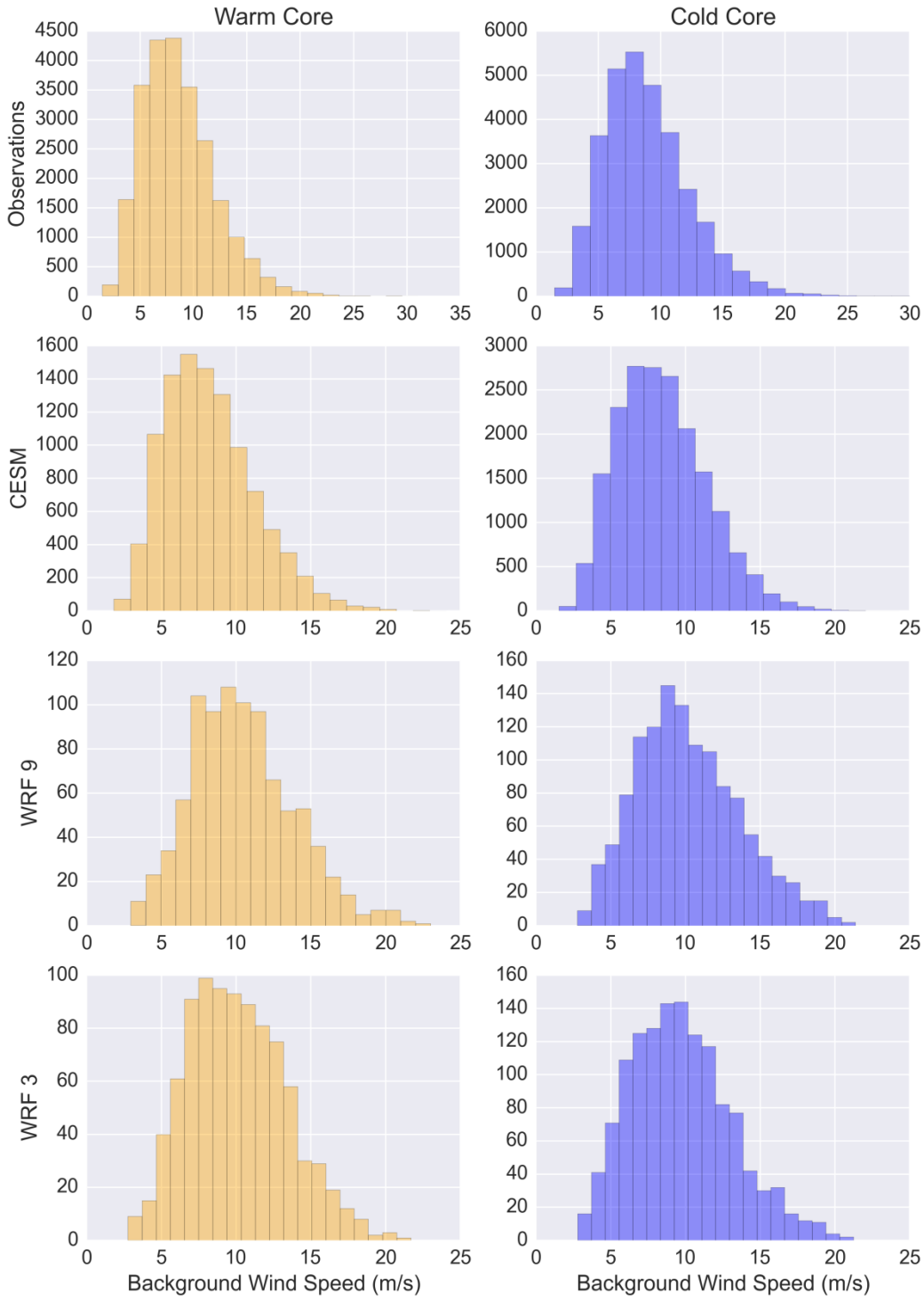

Figure 3.2. Background wind speed at the surface by eddy type. The background is defined as mean wind speed inside the outer two eddy radii of each four eddy radius composite.

For any significance testing of these results, the degrees of freedom had to be altered from a simple count. This is because the eddy features are detected each day but cannot be considered independent. Since eddies were not tracked throughout their lifetime in this study, the assumption is made that eddies are considered independent after a time period of four weeks. According to Kang and Curchitser (2013), most eddies in the Gulf Stream have a lifetime of 2-8 weeks, so four weeks seems like a reasonable approximation of independence.

The total number of eddies detected varied based upon which dataset was being investigated. Limiting the eddies to only the winter months, the observational dataset contained approximately 17,500 eddy detections, or an average of about 30 eddies present on any given day. The CESM coupled run consisted of approximately 8,200 eddy detections, or about 17 eddies per day. The two WRF runs had a similar number of eddies as compared to the CESM (about 18 per day for the WRF 9 run and 19 per day for the WRF 3 inner nest run). Warm core eddies were not as frequent as cold core for all four datasets, with cold core eddies occurring at a rate approximately 30% greater than warm core in the Gulf Stream region. The eddies detected in CESM were more imbalanced, with cold core eddies occurring at a ratio of 2:1 compared to warm core eddies.

The coupling coefficients obtained for this study are shown in Table 3.1. As a comparison to cloud fraction, the surface solar flux is used instead for the model runs since cloud fraction data was not saved in the CESM run and the WRF runs contained cloud fraction at several vertical levels instead of an overall summed fraction. For

surface winds, the models seem to show a coupling coefficient that is stronger than observations. This was also the case for rainfall, although the coefficients obtained for the two WRF runs were not statistically significant due to the run's short length and the restricted domain of the 3 km nest. Resolution did not seem to impact the coupling coefficients much between the two WRF runs for either latent heat flux or boundary layer height.

Variable Type	**Observations**	**CESM**	**WRF 9km**	**WRF 3km**
Wind Speed ($m\ s^{-1}\ ^oC^{-1}$)	0.17	0.28	0.20	0.22
Rainfall Rate ($mm\ day^{-1}\ ^oC^{-1}$)	0.10	0.14	*0.18**	*0.17**
Cloud Fraction ($\%\ ^oC^{-1}$)	1.02			
Surface Solar Flux ($W\ m^{-2}\ ^oC^{-1}$)		-1.25	-0.42	-0.74
Latent Heat Flux ($W\ m^{-2}\ ^oC^{-1}$)		28.21	38.52	38.62
Boundary Layer Height ($m\ ^oC^{-1}$)			37.16	38.36

Table 3.1. Coupling coefficients between SST anomalies and anomalies of the variable type listed. Values in italics with an asterisk were not a statistically significant linear fit in the F-test (p-values > 0.01).

The coefficients were a bit different than those reported by other papers, though no determination was made regarding whether those differences were statistically

significant. The rainfall rate coefficients were much less than those found in J. Ma et al. (2015) (0.66-0.71 mm day^{-1} $^{o}C^{-1}$) and were slightly less than those found in Byrne et al. (2015) (0.16-0.25 mm day^{-1} $^{o}C^{-1}$). Frenger et al. (2013) had a rainfall rate coupling of 0.17 mm day^{-1} $^{o}C^{-1}$, which is exactly the same as the WRF 3 km run. Cloud fraction coefficients were also about half as much as Frenger et al. (2013) (~2% C^{-1}) and Byrne et al. (2015) (2.2-3.6% C^{-1}). The coefficients for the boundary layer were also smaller than Byrne et al.(2015) (80 m C^{-1}) and Ma (55-57 m C^{-1}). Despite this, the latent heat flux coefficients were actually slightly greater in this study than in J. Ma et al. (2015) (19-20 W m^{-2} $^{o}C^{-1}$) and Byrne et al. (2015) (21 W m^{-2} $^{o}C^{-1}$). The only study that explicitly calculated surface wind coupling coefficients was J. Ma et al. (2015), and their coefficient was very similar to this study, ranging from 0.18-0.39 m s^{-1} $^{o}C^{-1}$.

The linear regression fits for surface winds, clouds/surface solar flux, and rainfall are shown for additional detail in Figures 3.3-3.5. The plots show the univariate linear regression fit, with a 95% confidence interval around the fit obtained through bootstrapping. Points along each line are the result of binning, with 95% confidence intervals also drawn via bootstrapping for each bin. For the linear relationship with wind (Figure 3.3), the fit appears quite linear across observations and model results. In clouds and surface solar flux (Figure 3.4), the linear relationship is not as strong, especially for the WRF results due to the shorter length of available data increasing the variability of the coupling strength. Rainfall (Figure 3.5) was noisy, indicating that the response isn't necessarily linear to SST anomalies.

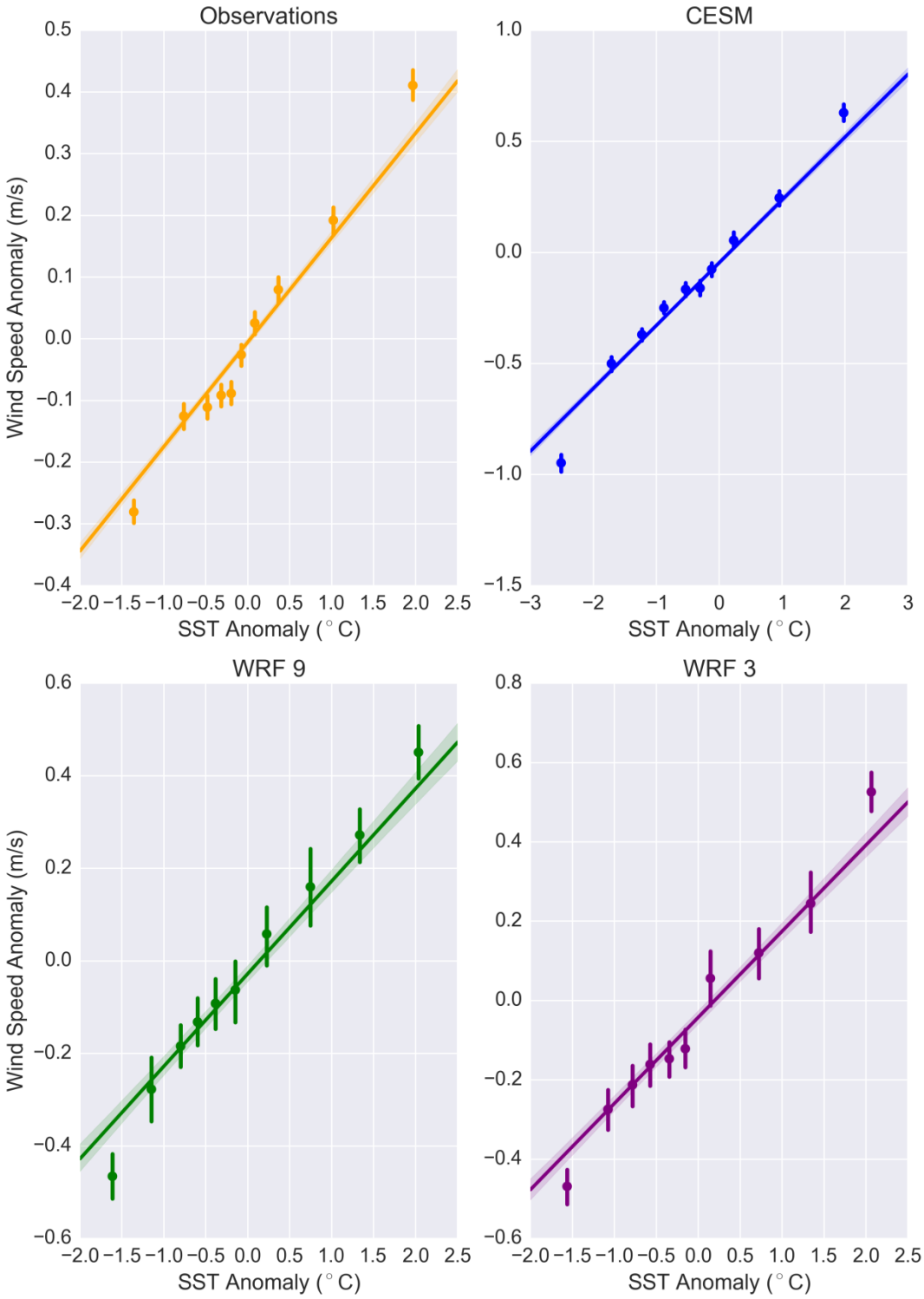

Figure 3.3. Linear fit of coupling strength between SST anomalies and surface wind anomalies for observations and model results. Confidence intervals are drawn at 95% based on bootstrapped samples.

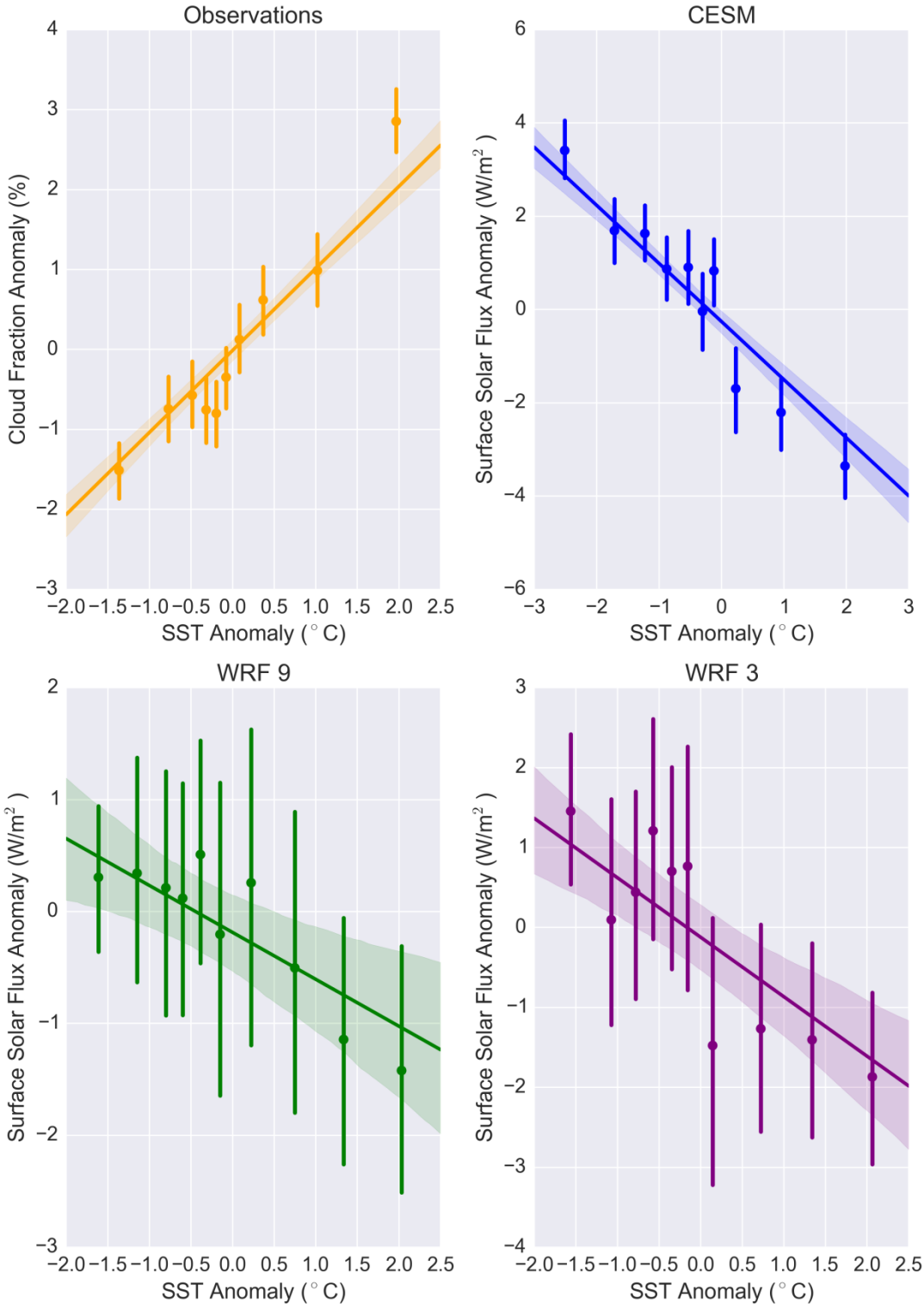

Figure 3.4. Same as Figure 3.3, except for cloud fraction and surface solar flux anomalies.

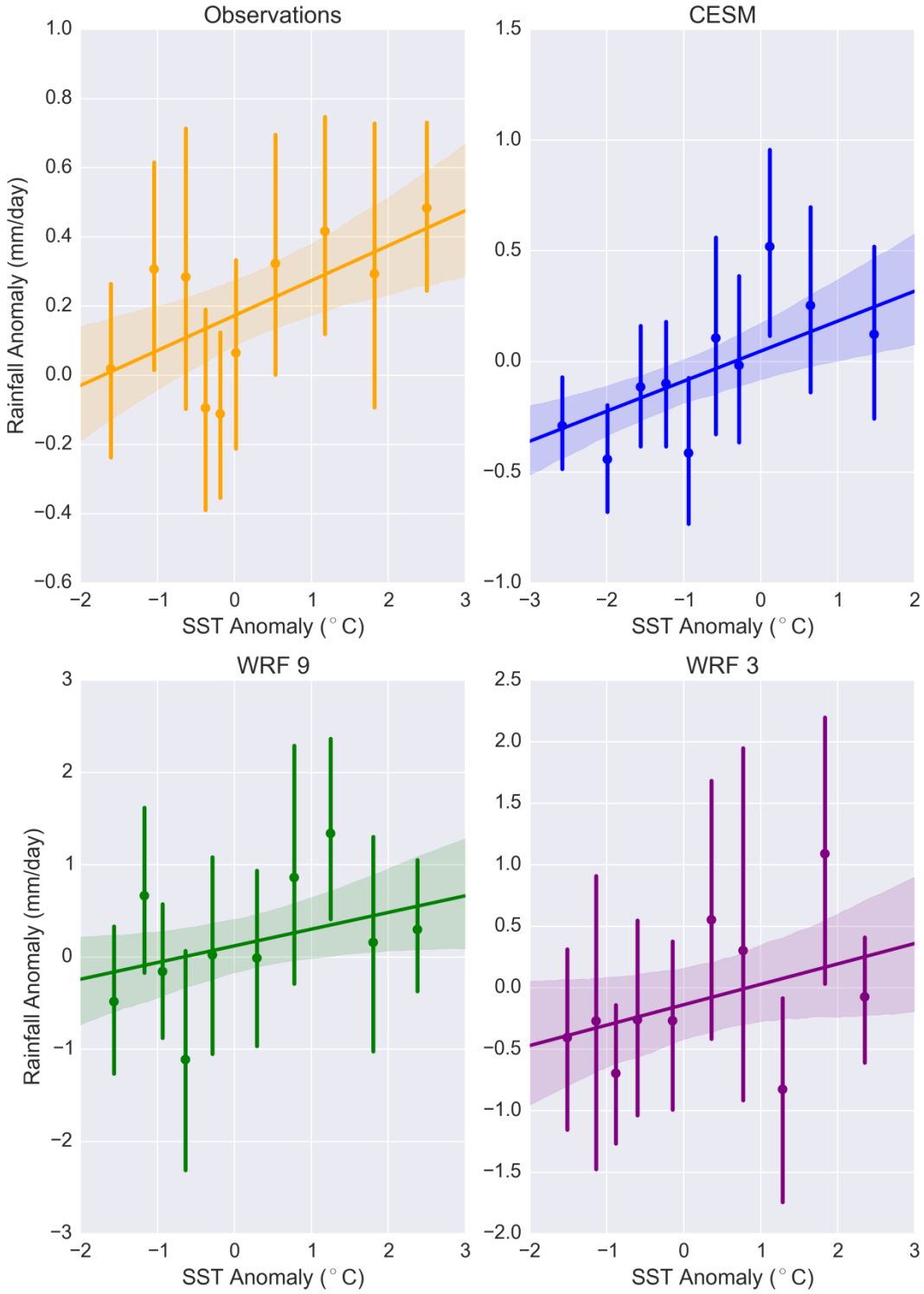

Figure 3.5. Same as Figure 3.3, except for rainfall anomalies.

3.3 Surface Composite Results

The SST composites (Figure 3.6) show great overlap between the eddy core and the temperature anomaly in both warm core and cold core eddy cases. This applies to observational data and model output. All of the model results tended to have a stronger SST anomaly compared to observations, especially CESM. This may be due to observations of SST and SLA being independent of each other, meaning errors in measurement could reduce the anomaly magnitude. In the coupled models, however, the SLA and SST need to be dynamically consistent with each other. The WRF 9 km run had the closest pattern to observations in terms of the SST gradient found across the eddy center. As alluded to by Frenger et al. (2013), the strong overlap in shape and location of these anomalies to the eddy location means the atmosphere is responding to the eddies themselves instead of the larger SST fronts the eddies are encompassed by.

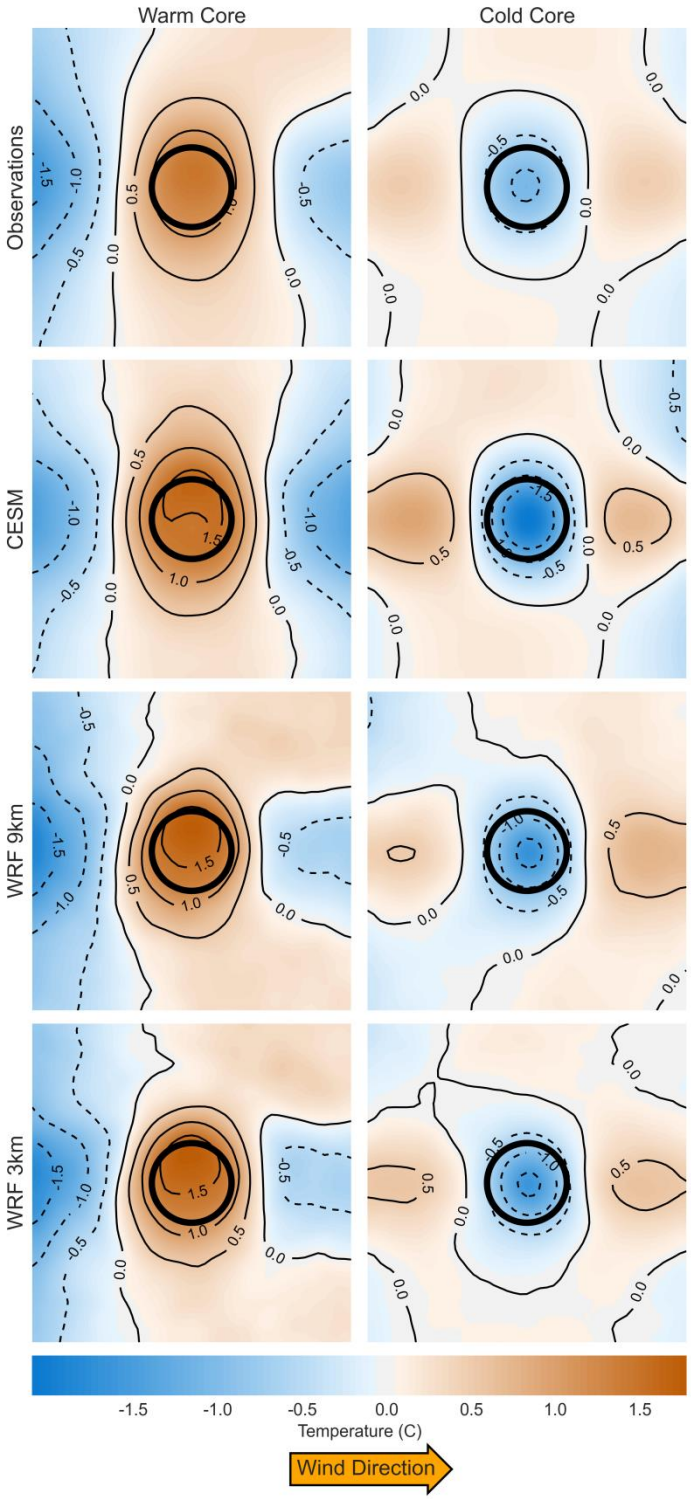

Figure 3.6. Composites of SST anomaly overlaid with the average eddy radius for both eddy types. The black circle represents the scaled eddy size of one eddy radii in relation to the background. Wind is from the left side of each composite, heading towards the right. Contour lines are spaced at 0.5°C intervals.

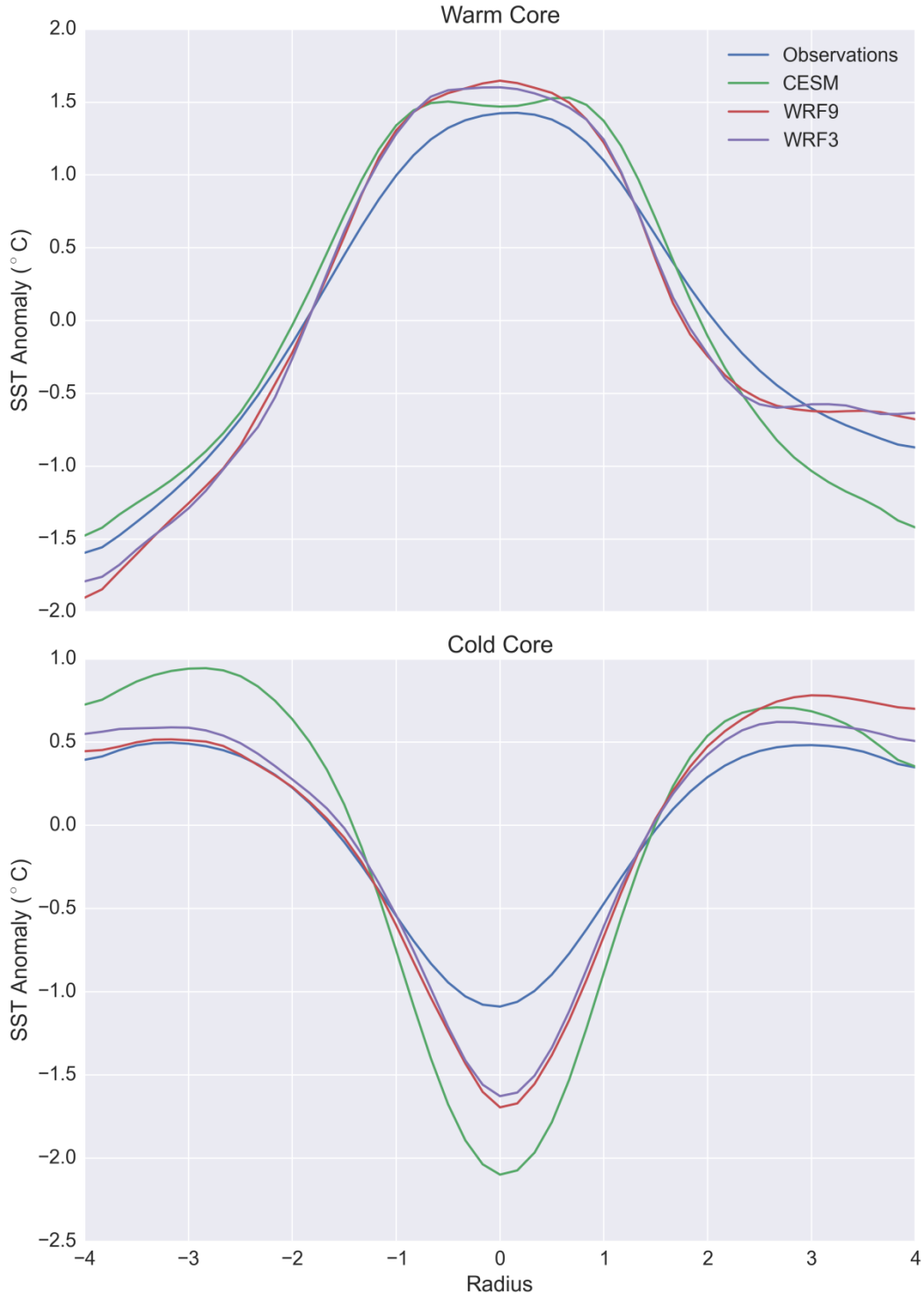

Figure 3.7. Based on Figure 3.6, except a chord is drawn through the center of each composite along a horizontal along-stream axis. The eddy radius distance is plotted on the x-axis and is based on a single composite radii indicated by the black circle from Figure 3.6.

A more detailed plot of the SST anomalies by eddy type is shown in Figure 3.7. Observations show the weakest overall anomalies compared to the models in both eddy types. Overall, the anomalies are fairly symmetric by type, with an exception for CESM having stronger cold core anomalies. Cold core eddies also seem to have a smaller core size, which is to be expected since most cold core eddies are of the smaller cyclonic eddy type.

Figure 3.8 shows a similar pattern with 10-meter wind speeds. Although the exact location of the wind speed anomaly varies in relation to the eddy center, the same anomaly pattern is shown in the observations and model results. An explanation for this change in surface winds is discussed in Bourras et al. (2004), where local SST minima resulted in greater wind speeds close to the boundary layer while simultaneously reducing wind speeds at the surface. The opposite pattern is also found with local SST maxima. The CESM showed a greater difference in the wind pattern between eddy types than the two WRF runs did.

The horizontal cross-section of the previous figure is shown in Figure 3.9. While most of the peak wind speed anomalies are directly over the eddy center in cold core eddies, the warm core eddy wind speed anomalies are shifted slightly downstream of the eddy center. A possible explanation for this is that warm core eddies tend to have vertical momentum transfer from the stronger winds above at the top of the boundary layer. The anomalies in CESM were the strongest for both core types, while observations had the weakest anomalies in both types. Cold core anomalies were stronger in the models than warm core anomalies, with the opposite true for observations.

Since latent heat fluxes from the surface are not available in satellite observations, only the model results are compared. There is strong overlap between the eddy center and the contouring of latent heat fluxes. Figure 3.10 shows the warm core and cold core eddy flux anomalies, indicating that the higher resolution WRF runs result in a larger flux anomaly for warm core eddies. Resolution seemed to matter less for cold core eddies. Due to increased evaporation from warmer SST found in the warm core eddies, the latent heat flux anomaly is strongly positive, while cold core eddies have a negative latent heat flux anomaly. This strong coupling has been observed in several other studies (Bryan et al. 2010, Liu et al. 2007, Vecchi et al. 2004). The heat exchange between the atmosphere and ocean cannot be modeled properly if the model is not able to resolve eddies, which could change the overall accuracy of the model. This is especially true at smaller spatial scales.

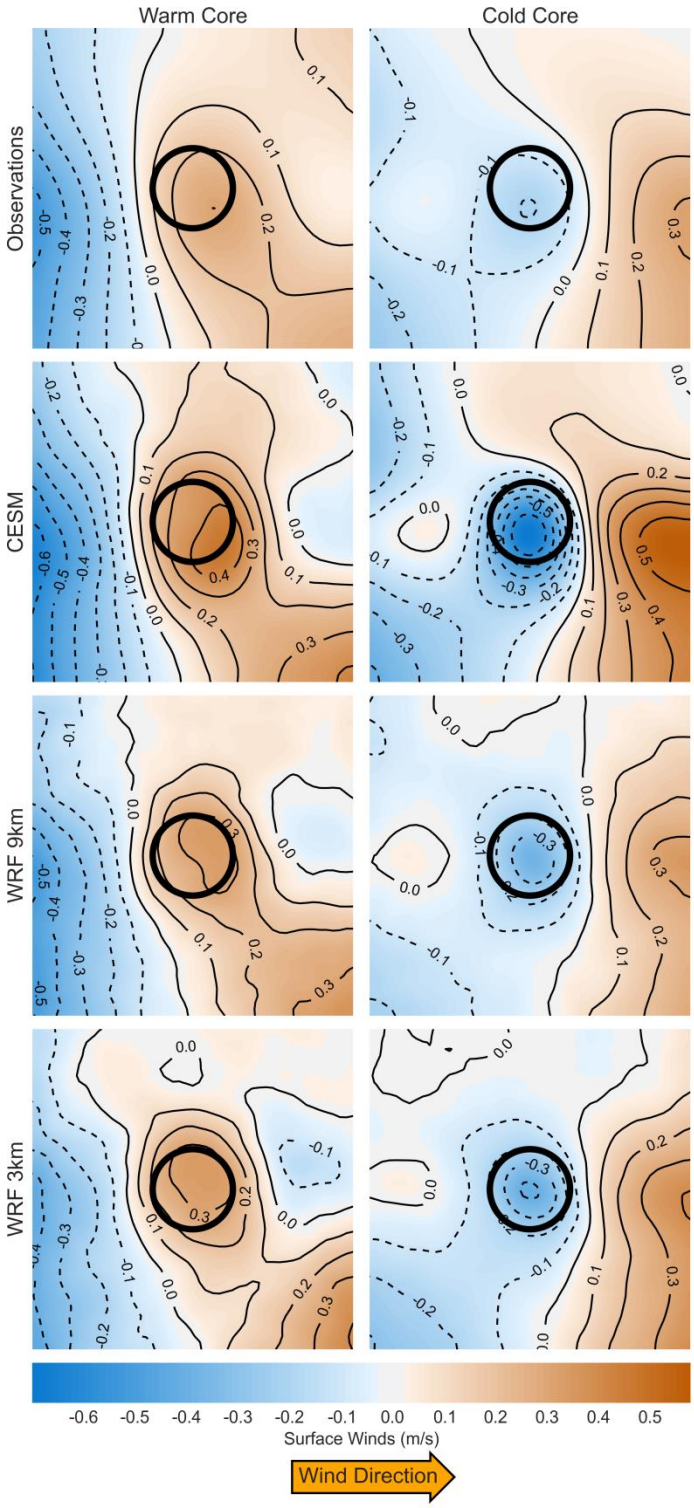

Figure 3.8. Same as Figure 3.6, except for 10-meter wind speed. Contour lines are spaced at 0.1 m/s intervals.

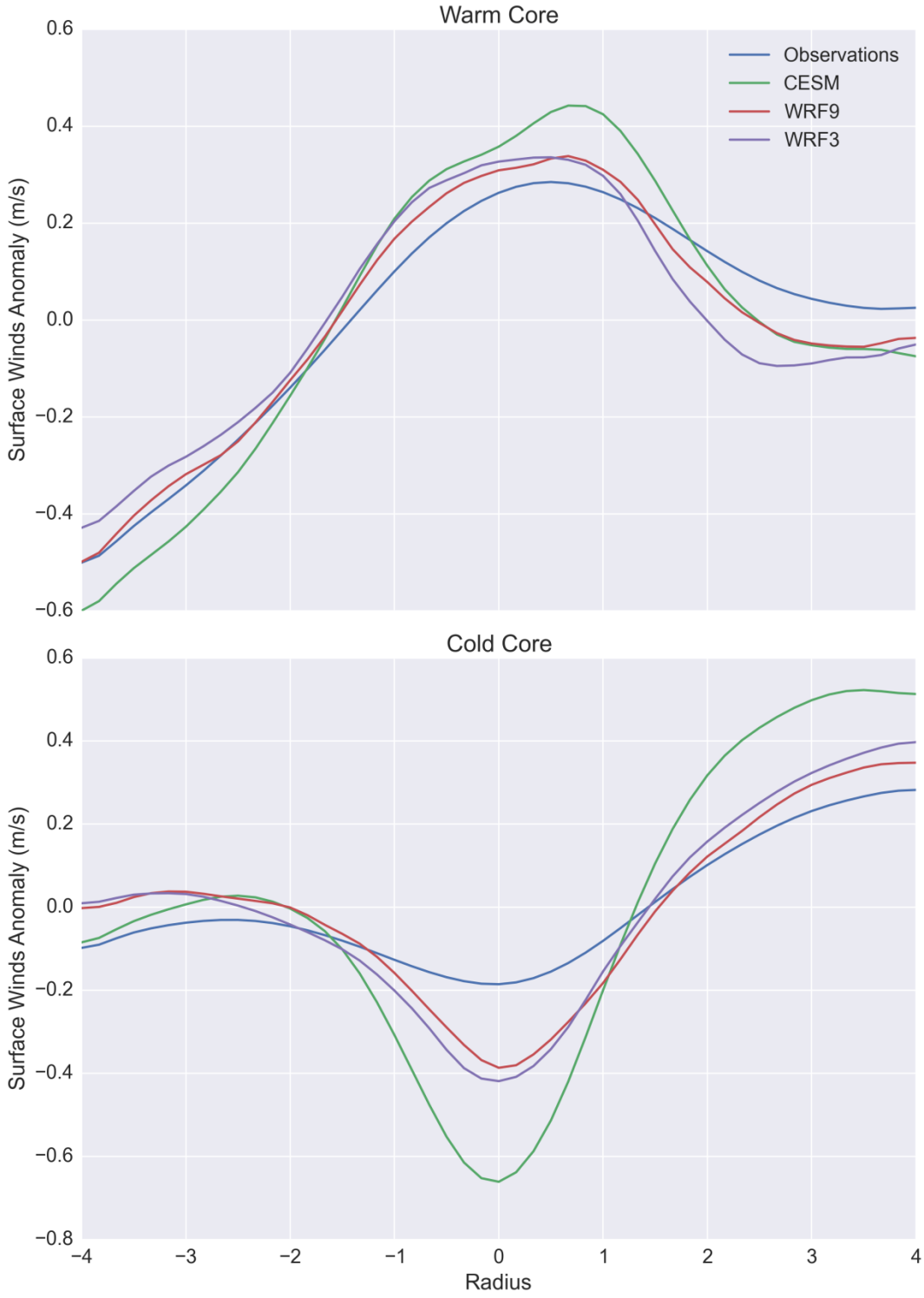

Figure 3.9. Similar to Figure 3.7 except for wind speed anomalies.

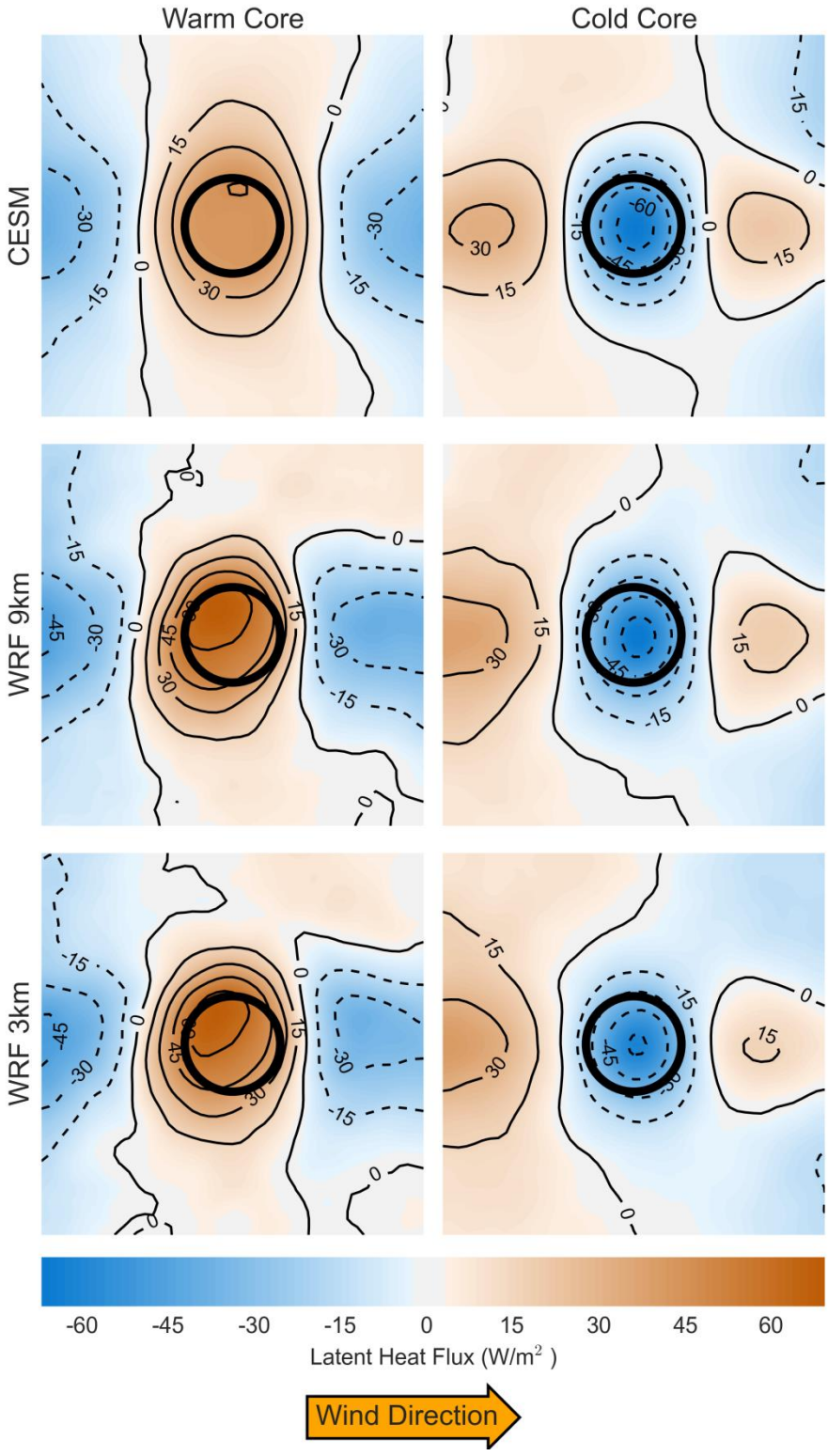

Figure 3.10. Same as Figure 3.6, except for latent heat fluxes. Contour lines are spaced at 15 W/m^2 intervals.

Boundary layer height data was available in the two coupled WRF runs only, so these two runs are compared in Figure 3.11. As observed in several other studies (Chelton et al. 2004, Seo et al. 2008, Bourras et al. 2004) and suggested as a possibility by Frenger et al. (2013), the modeling results seem to agree that mesoscale oceanic eddies can alter the boundary layer height. Warm core eddies raise the boundary layer height due to increased vertical mixing, while cold core eddies lower the boundary layer due to a reduction in vertical mixing. Warm core eddies had a stronger boundary layer height anomaly in the 9km run, with the anomalies being more balanced between eddy types in the 3km run.

Because the results were not as clear for cloud fraction/surface solar flux and rainfall data, the composites for warm core and cold core were instead subtracted from each other for the next two figures. In the case of rainfall differences, shown in Figure 3.12, the positive rainfall anomaly from the eddy is not located directly at the eddy center. However, there does seem to be a positive rainfall anomaly present in all cases on the downwind side of the eddy, including observations. This is a slightly different result than what Frenger et al. (2013) indicated, with their results showing the anomaly located directly over the eddy core. The results from Bourras et al. (2004) seem to indicate the local updraft/downdraft occurs downwind from the SST anomaly, concurring more with the findings seen in this study.

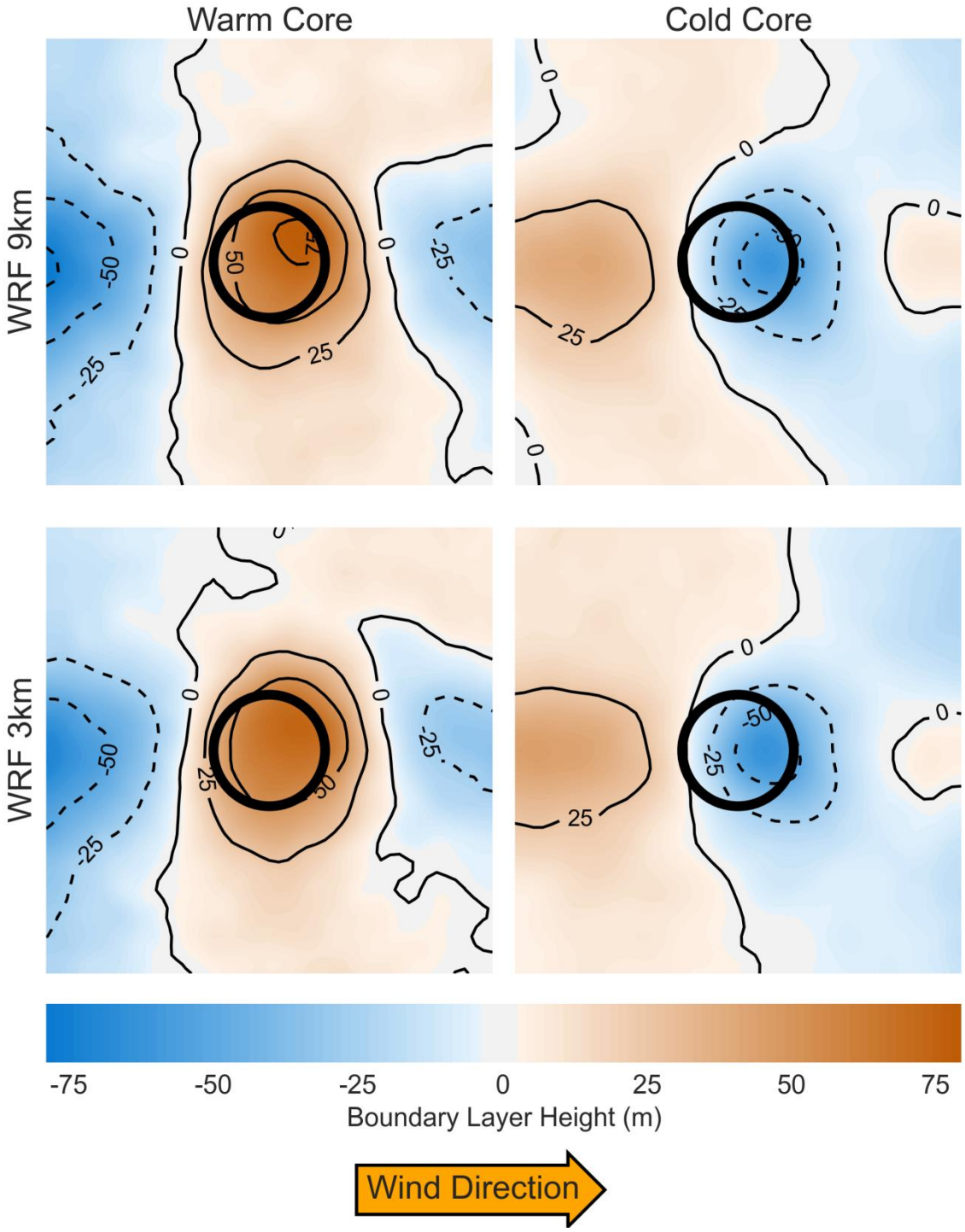

Figure 3.11. Same as Figure 3.6 except for boundary layer height. Contour lines are spaced at 25 meter intervals.

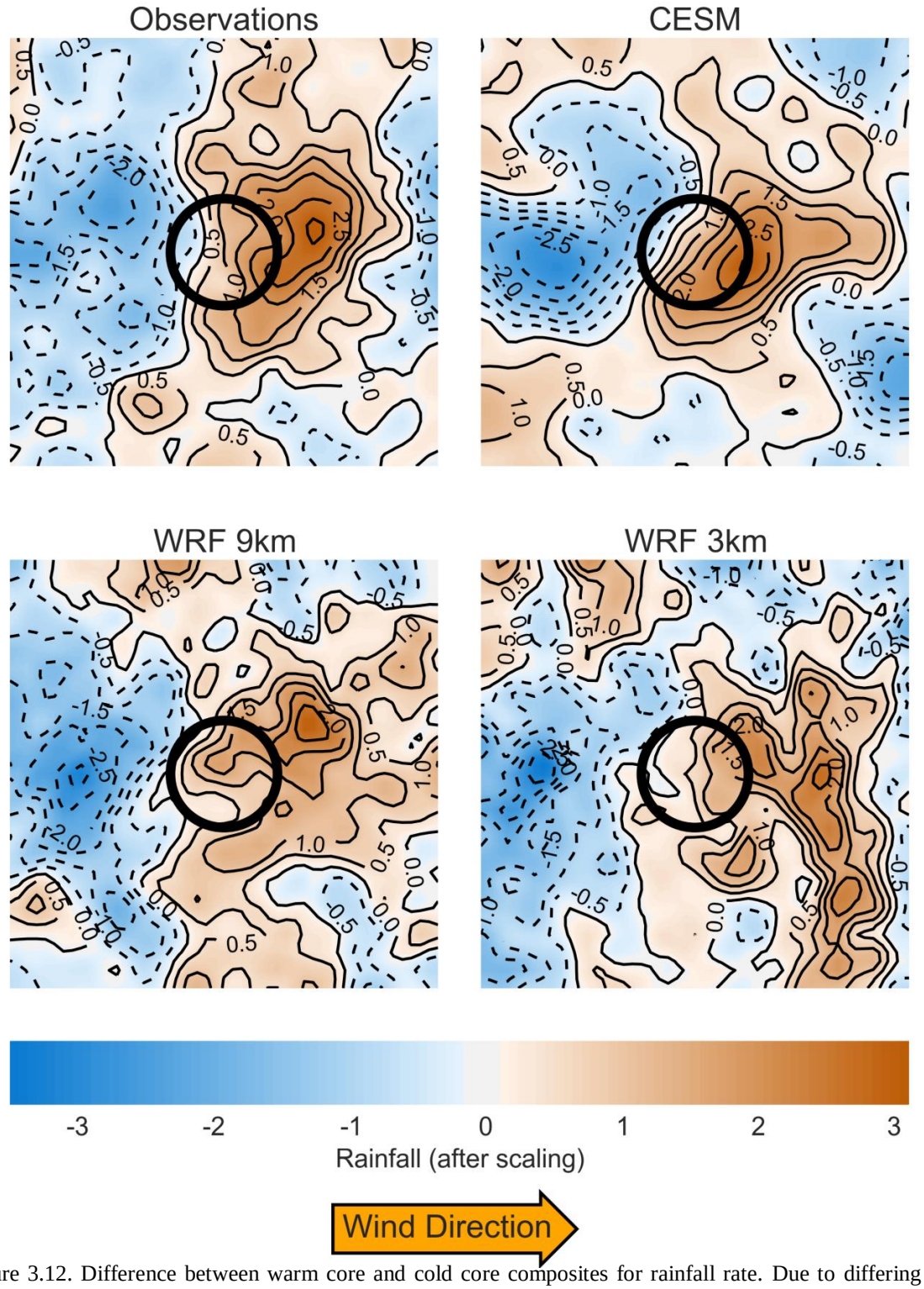

Figure 3.12. Difference between warm core and cold core composites for rainfall rate. Due to differing magnitudes between observations and model results, the composites are normalized to a mean of zero and standard deviation of one for better visual comparison. Note that the coupling coefficients were not considered statistically significant for the two WRF runs for rainfall rate as indicated by Table 3.1.

In J. Ma et al. (2015) results were more inconclusive with regard to rain rate. While their analysis found a rain rate maximum slightly downwind of the eddy center in CFSR data for warm core eddies, they did not find a downwind maximum in the Tropical Rainfall Measuring Mission's (TRMM) Microwave Imager (TMI) data. Given the consistency of a downwind maximum found in all four datasets, this study concludes a downwind influence of rainfall is a more likely result than directly over the eddy's core.

Investigating the rainfall composites with more precision, Figure 3.13 shows the peak in rainfall anomaly is clearly downwind of the eddy center. How far downwind the anomaly is at a maximum varies. CESM has a maximum anomaly at precisely one radius downstream of the eddy center, while observations show a local maximum at approximately 1.5 eddy radii downstream. The two WRF runs varied some, with the 3 km nest showing a peak at over two eddy radii downstream, while the 9 km run peaked closer to 1.3 eddy radii. Even though the location of the maximum rainfall anomaly varies, all four datasets show the maximum anomaly is not located directly over the eddy center.

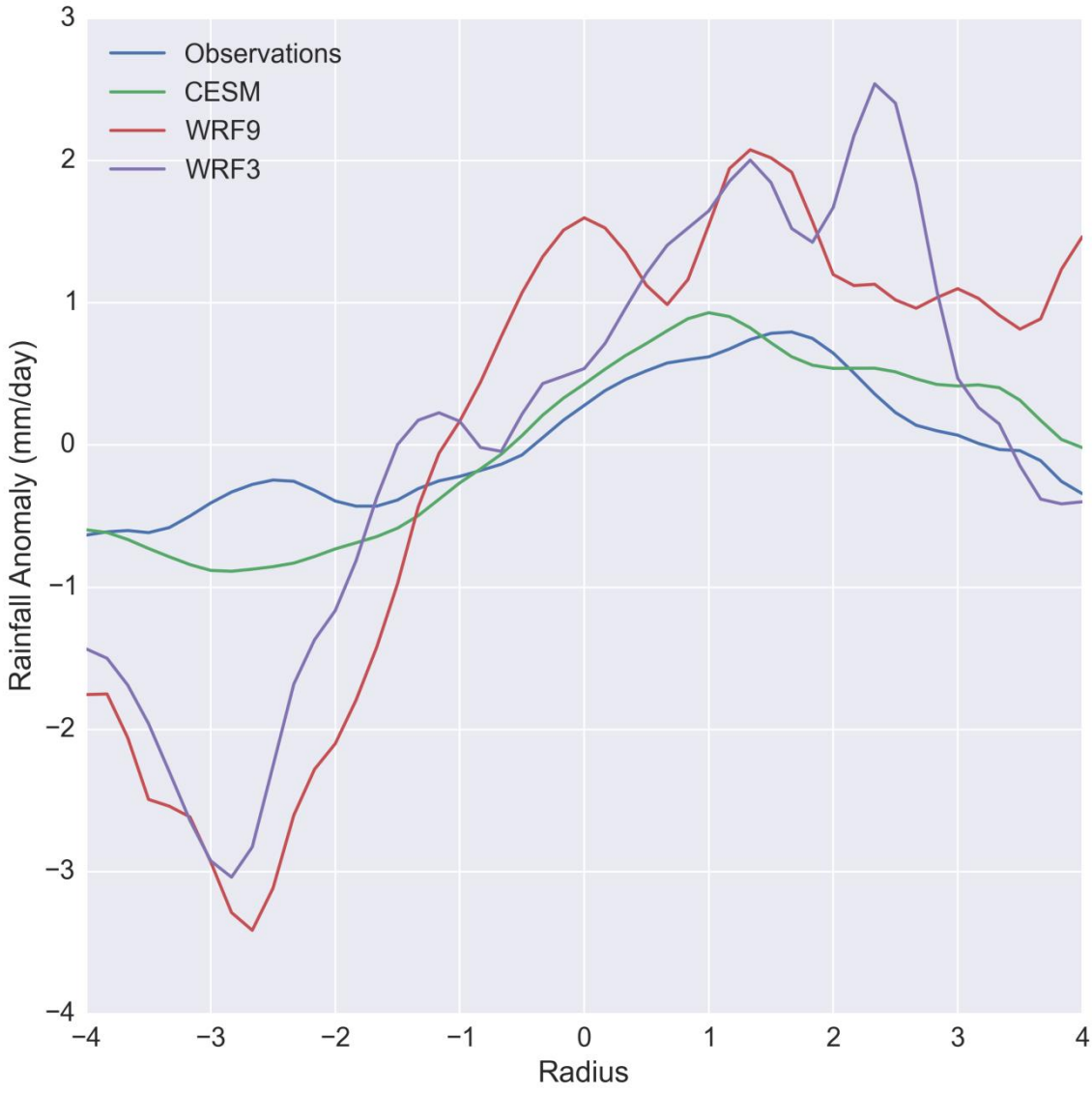

Figure 3.13. Similar to Figure 3.7, except for rainfall rate anomalies. Note that the coupling coefficients were not considered statistically significant for the two WRF runs for rainfall rate as indicated by Table 3.1.

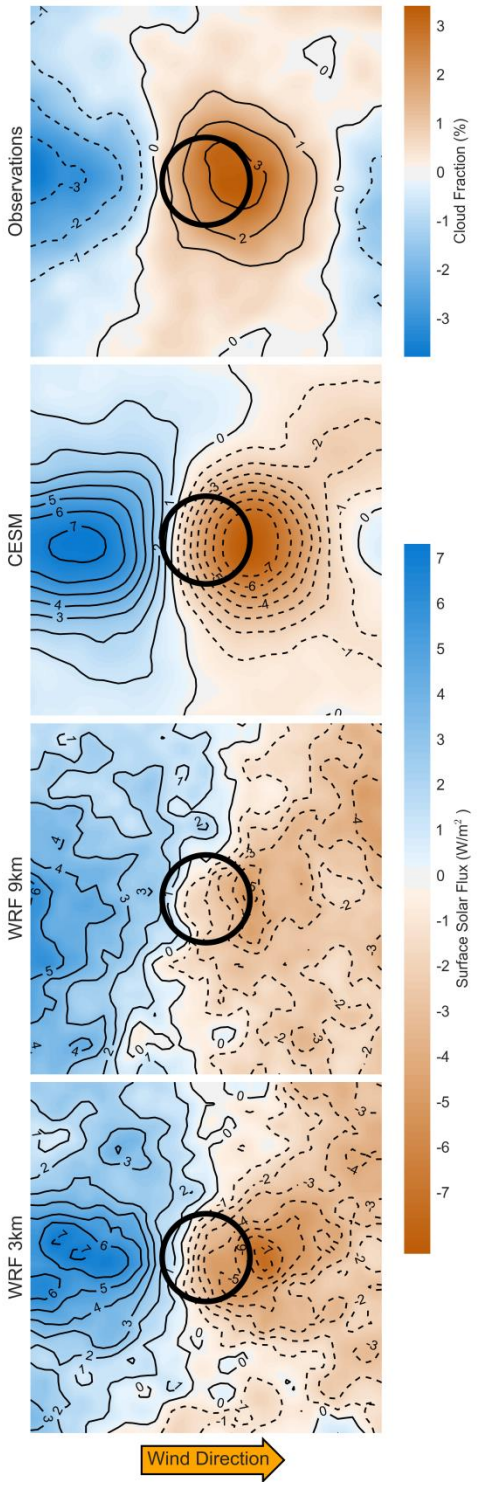

Figure 3.14. Shows the difference in eddy types for cloud influence, similar to Figure 3.12. In this case, the observations show the difference in cloud fraction while the three model results show surface solar flux as a proxy for cloud fraction. Contouring for the cloud fraction composite is spaced at 1% intervals, while the contouring for the solar fluxes is spaced at 1 W m^{-2} intervals.

Figure 3.14 seems to confirm this idea that clouds and rainfall development occur downwind from the eddy core. In the model results, surface solar flux is used as a proxy for cloud cover to compare with the observational data. Lower surface solar fluxes indicate greater levels of cloud cover, so the two are inversely related. These results concur with what J. Ma et al. (2015) found for cloud liquid water maxima occurring downwind, but Frenger et al. 2013 claims that maximum cloud development occurs directly in-phase with the SST anomaly, over the eddy's core. Byrne et al. (2015) seems to show similar downwind results, and posits this may be due to the wind conditions at the eddy's location. Greater wind conditions allow for the moisture to be more mixed, resulting in precipitation and cloud formation further downstream and out of phase with the maximum SST anomaly. Given that all three studies were done in different regions, it is possible the environmental background wind can explain the differences found between Frenger et al. (2013) and the other studies.

A more detailed investigation into cloud formation is shown in Figure 3.15. The local maximum in cloud cover seems to occur between 0.3 and 1 eddy radius downstream in observations, but the maximum anomaly is a full eddy radius downstream in the case of the CESM results. The WRF 9 km run showed a minimum in surface solar flux, which indicates clouds were more present, at one eddy radius downstream as well. These locations match up with the local maxima for rainfall found in Figure 3.13 for CESM, except observations and the two WRF runs seem to show the rainfall maximum further downstream than the cloud maximum.

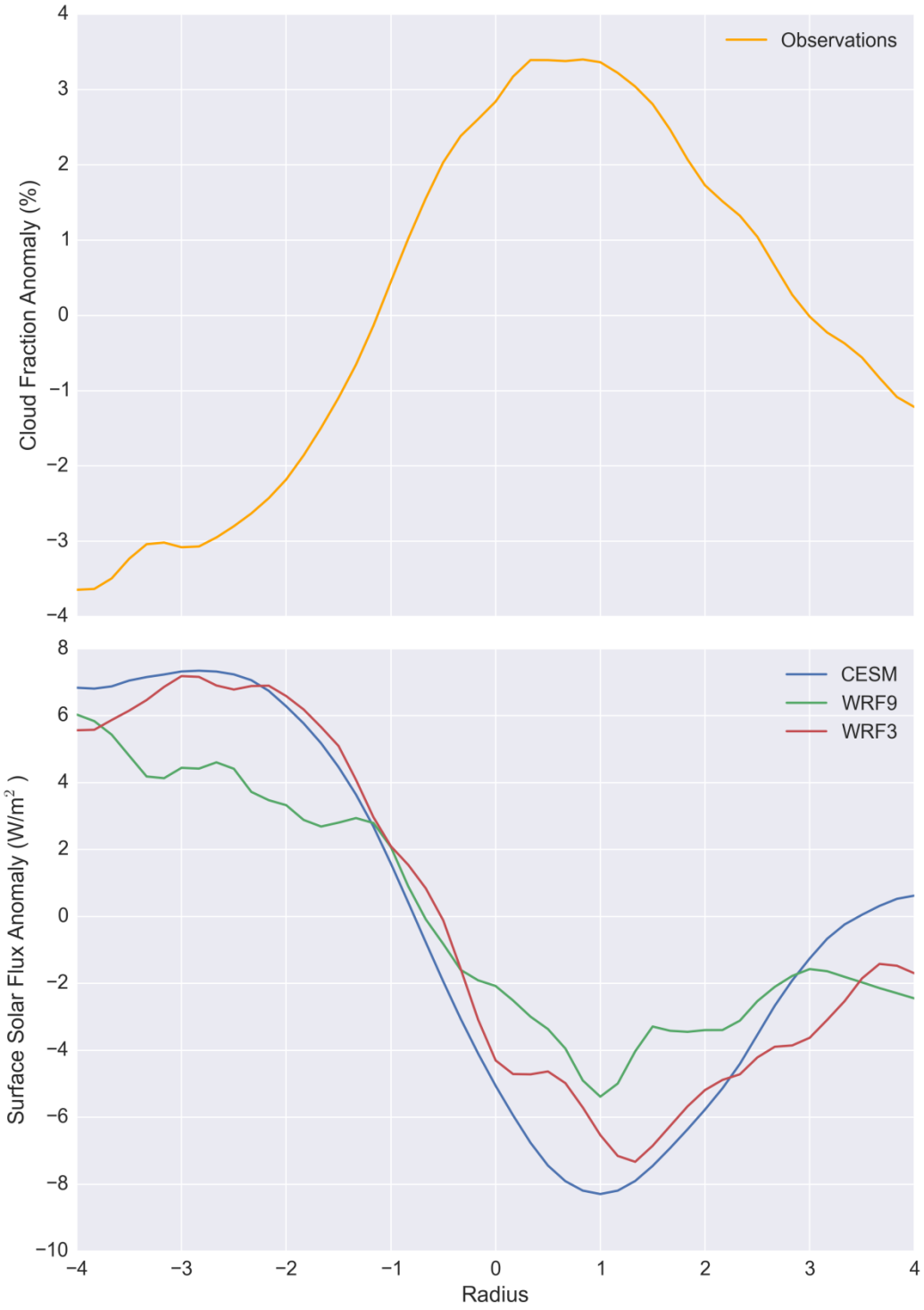

Figure 3.15. Similar to Figure 3.7, except for cloud fraction/surface solar flux anomalies.

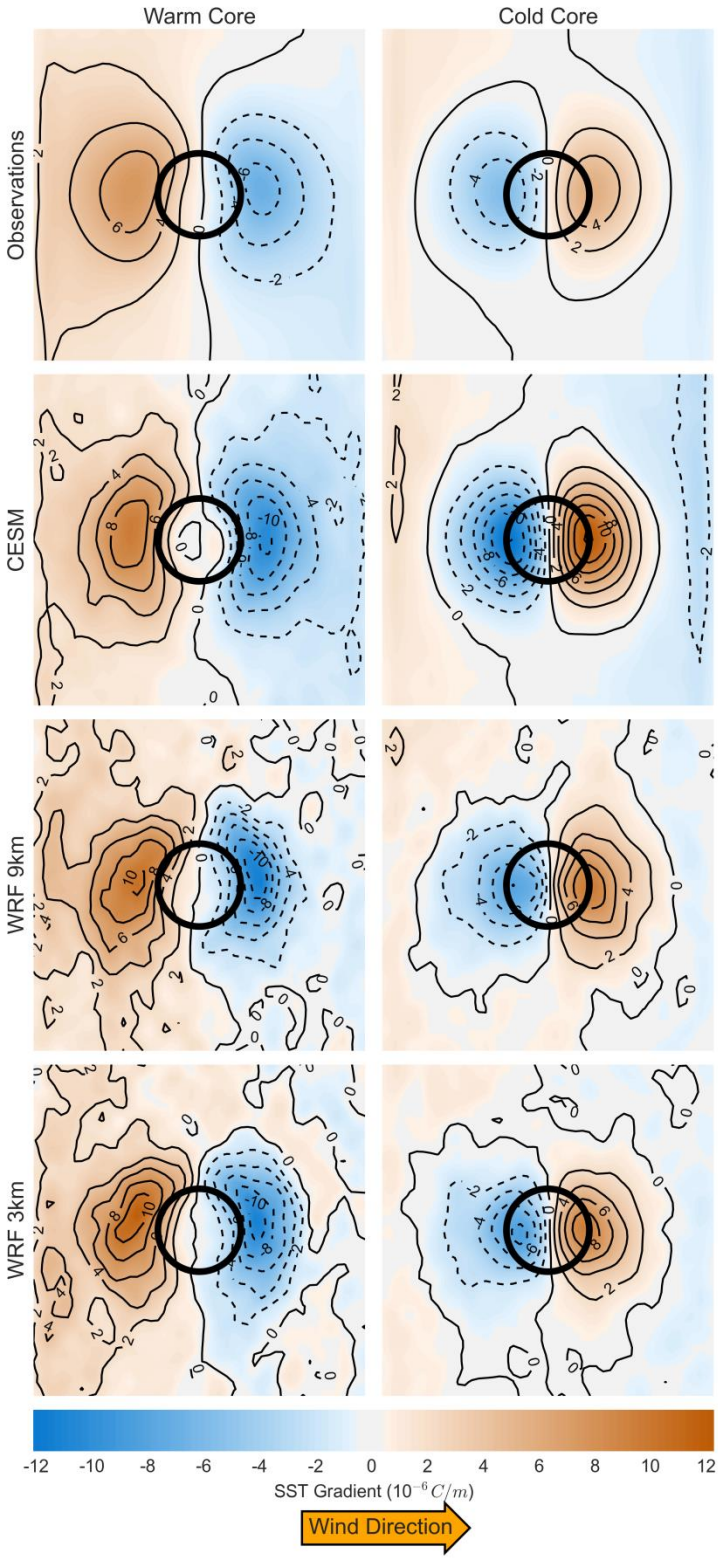

Figure 3.16. Horizontal SST gradients by eddy type. Contouring is spaced in $2x10^{-6}$ °C m^{-1} intervals.

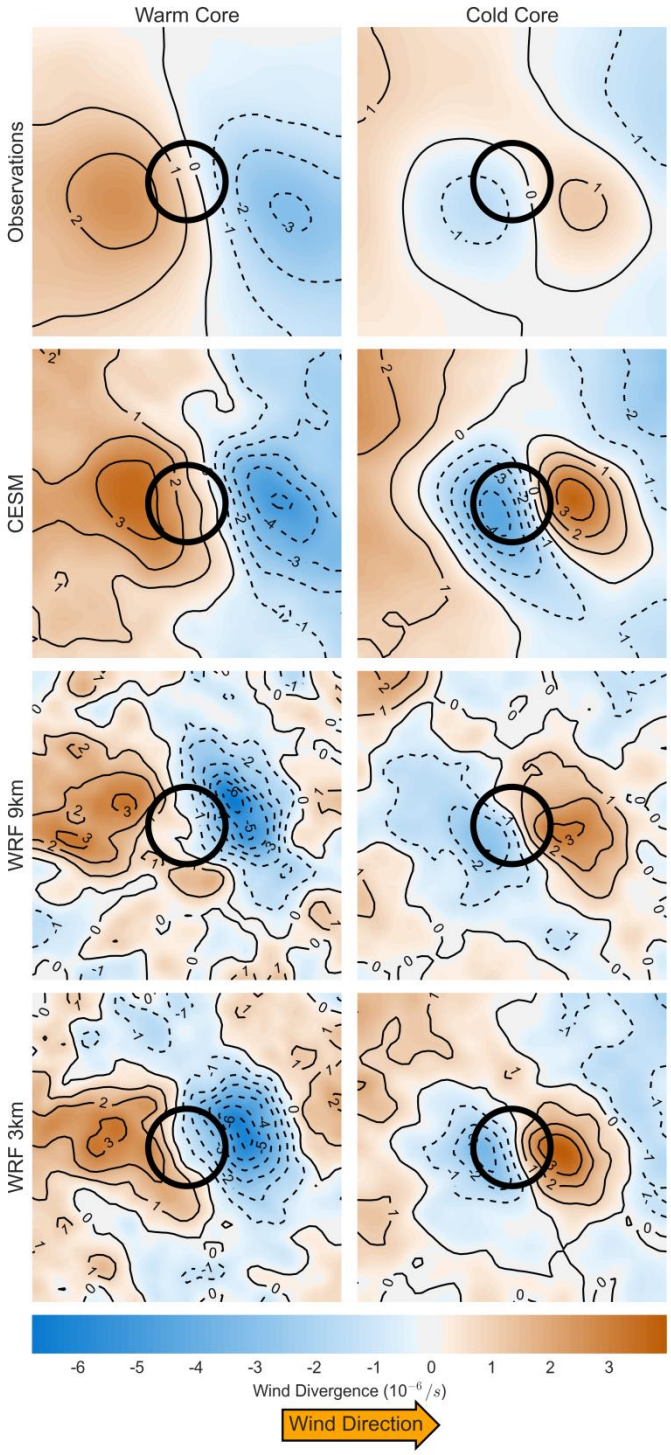

Figure 3.17. Surface wind divergence by eddy type. The CESM wind divergence is shown at the lowest model level (approximately 67 meters in altitude) while the other datasets are shown at 10 meters. Contouring is spaced in 10^{-6} s^{-1} intervals.

While sea level pressure anomalies were investigated in all models, the results were not significant enough to be shown, indicating no measureable pressure anomaly in response to the eddies. Studies such as Small et al. (2008) and Putrasahan et al. (2013) have posited that vertical mixing and pressure adjustment are both plausible mechanisms to explain the atmospheric response to these SST anomalies found in oceanic eddies. It was found in Lindzen and Nigam (1987) that positive sea surface temperatures anomalies could lead to a reduction in sea level pressure, causing convergence of winds at the center of pressure reduction.

The three major previous studies on interactions between oceanic eddies and the atmosphere (Frenger et al. 2013, Byrne et al. 2015, J. Ma et al. 2015) find that the vertical mixing mechanism is most likely dominant due to the dipolar pattern of wind divergence investigated. The same investigation was done for this study and is shown in Figures 3.16-3.17. As can be seen, a dipolar pattern of wind divergence and the SST gradient is found, and it occurs across both eddy types and in both observational and model results. If the pressure adjustment mechanism were dominant, there would be convergence directly over the eddy's center due to the pressure gradient, which would be indicated by a tripolar pattern in the wind divergence due to subtraction of the zonal mean. Because of vertical mixing, the pattern is dipolar with convergence of winds occurring downstream of the eddy center and divergence upstream.

Even though the pattern for boundary layer height changes overlaps with oceanic eddies closely, sea level pressure anomalies did not in any discernible way. This could be because of the results found in Lambaerts et al. (2013), which discovered that the

pressure adjustment mechanism only dominates in areas of low wind speeds. Because the wind speeds near the Gulf Stream are relatively strong, any pressure differences are distorted too quickly to allow for local pressure adjustment at the eddy's location.

3.4 Conclusion

So far, this study has shown that eddies impact the atmosphere at the surface, with warm core eddies increasing local surface wind speeds, latent heat fluxes, and boundary layer height. Warm core eddies also increase cloud cover and rainfall slightly downstream of the eddy center, while decreasing them upstream of the eddy center. The location of the local cloud and rainfall maximum partially depends on how strong the horizontal winds in the boundary layer are. Cold core eddies have an opposite effect.

What has not yet been shown is whether this influence is only near the surface, below the boundary layer, or whether this atmospheric influence can extend even further, beyond the boundary layer itself. J. Ma et al. (2015) found vertical velocity anomalies extending up to 750 hPa, for example. If warm core eddies can influence cloud formation, where in the atmosphere do these clouds form? Is moisture transported vertically? What does the vertical profile of atmospheric influence from an oceanic eddy look like? Can the vertical mixing mechanism be observed in another way? Answers to these types of questions will be the focus of the next chapter.

4. VERTICAL STRUCTURE OF ATMOSPHERIC RESPONSE

While the previous chapter focused on eddy influence of the atmosphere near the surface, this chapter explores the influence of oceanic eddies throughout the troposphere. Previous research has found that SST fronts have an influence that extends beyond the boundary layer. Vertical wind velocities can exist in the upper troposphere due to SST fronts in the North Atlantic (Minobe et al. 2008), and storm tracks can be altered based on the variability of the Kuroshio Extension's current (O'Reilly and Czaja 2015).

In terms of measuring the effects of eddies on the atmosphere beyond the boundary layer, research is more limited. J. Ma et al. (2015) found that vertical velocity anomalies exist beyond the boundary layer downstream of the eddy core, while X. Ma et al. (2015) found that eddies in the Kuroshio Extension can change rainfall variability on the northern Pacific U.S. coastline. It seems some eddy influence does exist beyond the boundary layer.

In order to determine the depth of atmospheric influence, vertical composites of the atmospheric data are generated, similar to the previous chapter. These composites will be used to analyze the strength of the coupling between the SST anomalies at the surface and the atmospheric profile above. Reanalysis datasets are used as a comparison to coupled model results.

4.1 Vertical Composite Methodology

Calculating the vertical composites requires a very similar technique to the surface composites. The prevailing wind direction is used to rotate the atmospheric data in a box the size of four eddy radii outwards, the same as before. This time, however, every vertical layer of data at a detected eddy feature's location is also rotated in the same direction. At each vertical level, a chord running down the center of each rotated composite is saved, parallel to the prevailing winds near the surface. These chords are then stacked upon each other for each pressure level in the atmospheric data. While the reanalysis data for both CFSR and YOTC was available at pressure levels, the WRF data was saved at sigma coordinate levels, which required the vertical levels to be interpolated to pressure levels. Since both the CFSR and YOTC are reanalysis datasets, the detected eddies from the observational SLA data are used again for the vertical composites in these two datasets. The WRF vertical composites use the same detected eddies as were used for the surface composites.

4.2 Vertical Composite Results

Investigating the potential temperature anomalies (Figure 4.1), it can be seen that influence on temperature does not primarily extend beyond the boundary layer. Most of the influence is confined close to the surface below 950 hPa, with some warming or cooling also occurring just above the boundary layer. The anomaly differences were larger in the two WRF runs than in the reanalysis datasets, and are consistently shifted slightly downstream of the eddy center. Given that the SST maximum or minimum is located directly over the eddy center, vertical mixing must be shifting the warming or cooling downstream. This result was also found in J. Ma et al. (2015) when their study investigated vertical potential temperature response to oceanic eddies. Given that the warming or cooling influence is restricted close to the surface, this implies a decrease or increase in stability downstream of the eddy, allowing vertical mixing to occur or not occur.

In order to visually identify the anomalies more clearly, a vertical profile at one eddy radius downwind of the center is plotted (Figure 4.2). The potential temperature anomaly absolute values are only greater than 0.1^{o}C up to 850 hPa, indicating that vertical mixing of the warmer temperatures at the surface in warm core eddies is limited to the boundary layer. The anomaly difference between eddy types was larger in the two WRF runs. The reanalysis datasets had much smaller anomaly differences on average at 1000 hPa of only approximately 0.3^{o} C. The vertical influence of the YOTC data seems to extend slightly higher in the atmosphere past 850 hPa than CFSR or model runs.

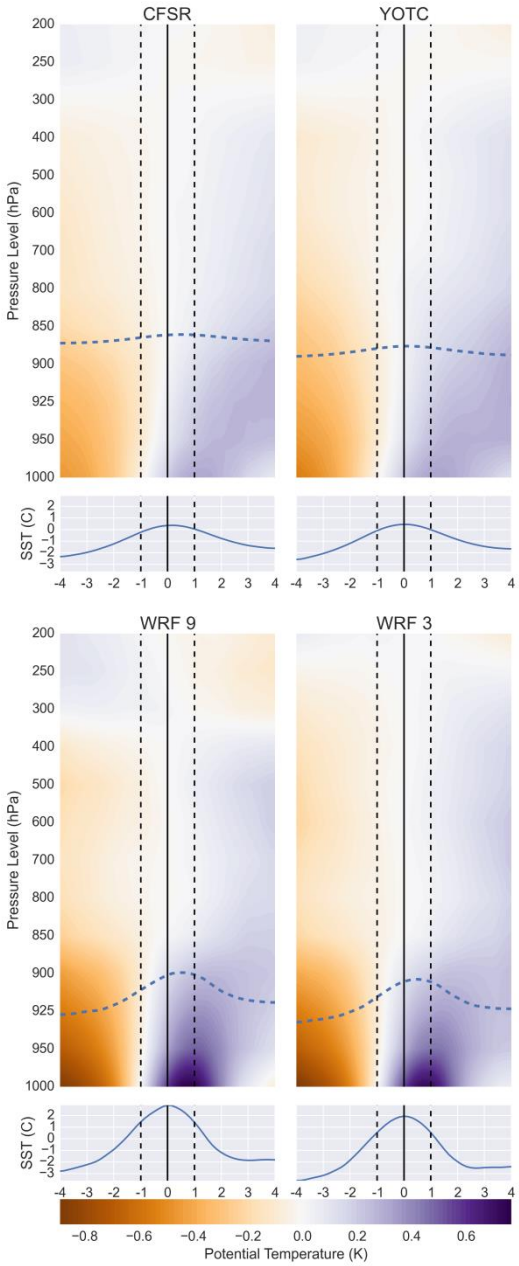

Figure 4.1. Vertical composites of potential temperature anomalies in response to the eddies. Zonal means have been subtracted in each vertical layer, and the difference between eddy types is shown (warm core minus cold core). The dotted blue line represents the difference between the boundary layer heights of each eddy type, which has been added to the average between the two in order to plot the boundary layer's position relative to the anomalies. The difference between eddy types for SST along a central chord is also shown at the bottom of the plot. The vertical dotted lines represent the outer edges of a single scaled eddy radii, with x-axis indicating the number of eddy radii outward from the center at the bottom of each subplot.

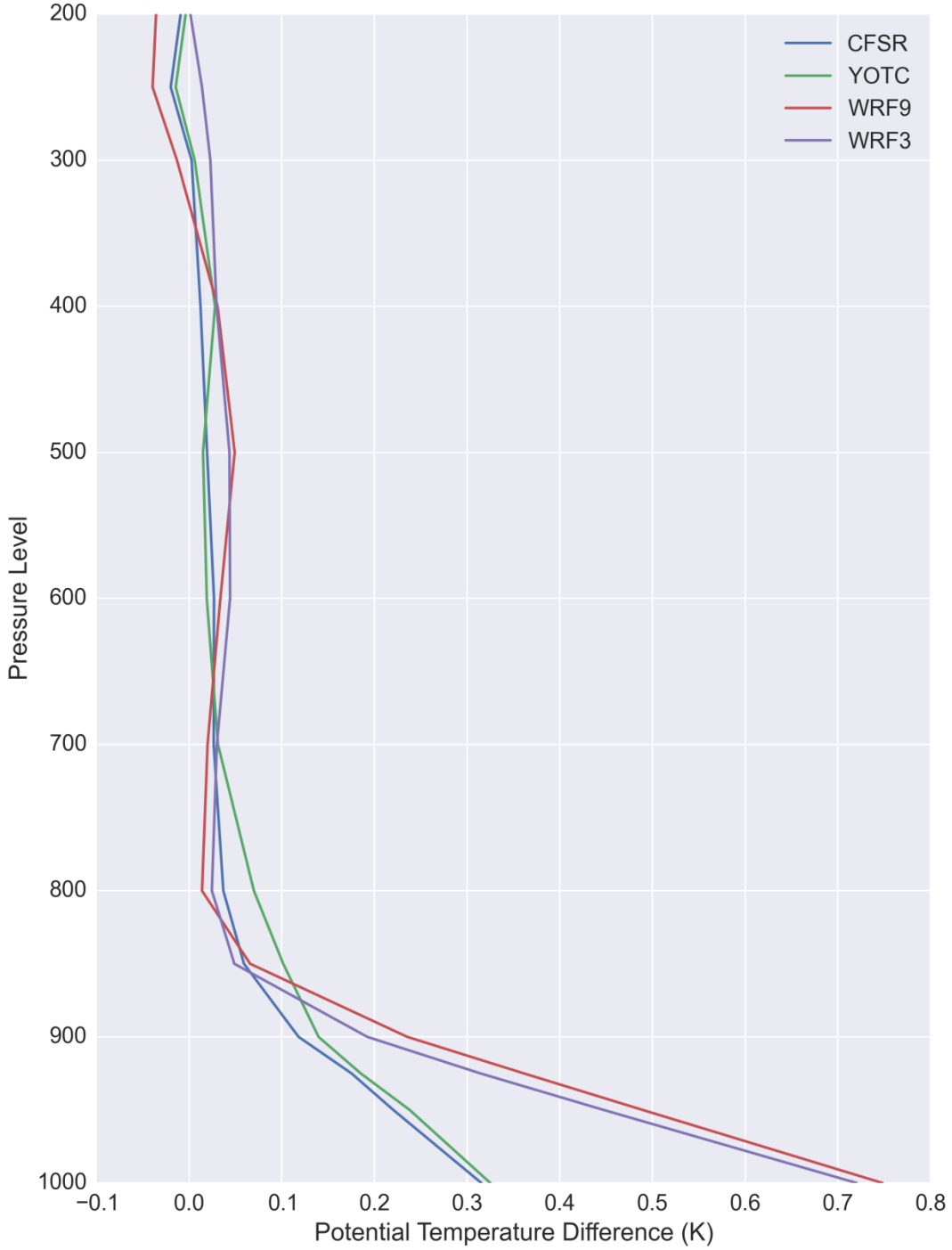

Figure 4.2. Difference in potential temperature anomalies between eddy types at a distance one eddy radius downstream of the eddy center throughout the atmosphere.

To further show the extent of vertical influence, coupling coefficients between the eddy SST anomalies and the potential temperature anomalies are calculated. Unlike Chapter 3, these coupling coefficients are a simple ratio, with the difference in potential temperature anomalies divided by the difference in the maximum SST anomalies at the eddy center. The potential temperature anomalies are taken, similar to Figure 4.2, along a vertical profile at one eddy radius downstream of the center. Figure 4.3 shows that the coupling coefficient weakens significantly past 900 hPa. There is remarkable agreement between the reanalysis and model results on the magnitude of the coefficients, especially near the surface. However, it seems the two WRF models actually underestimate the coupling strength compared to reanalysis data through the boundary layer. Resolution differences in the WRF runs had a negligible impact on the coupling strength, whereas the difference is more significant between YOTC and CFSR, especially between 850 and 700 hPa.

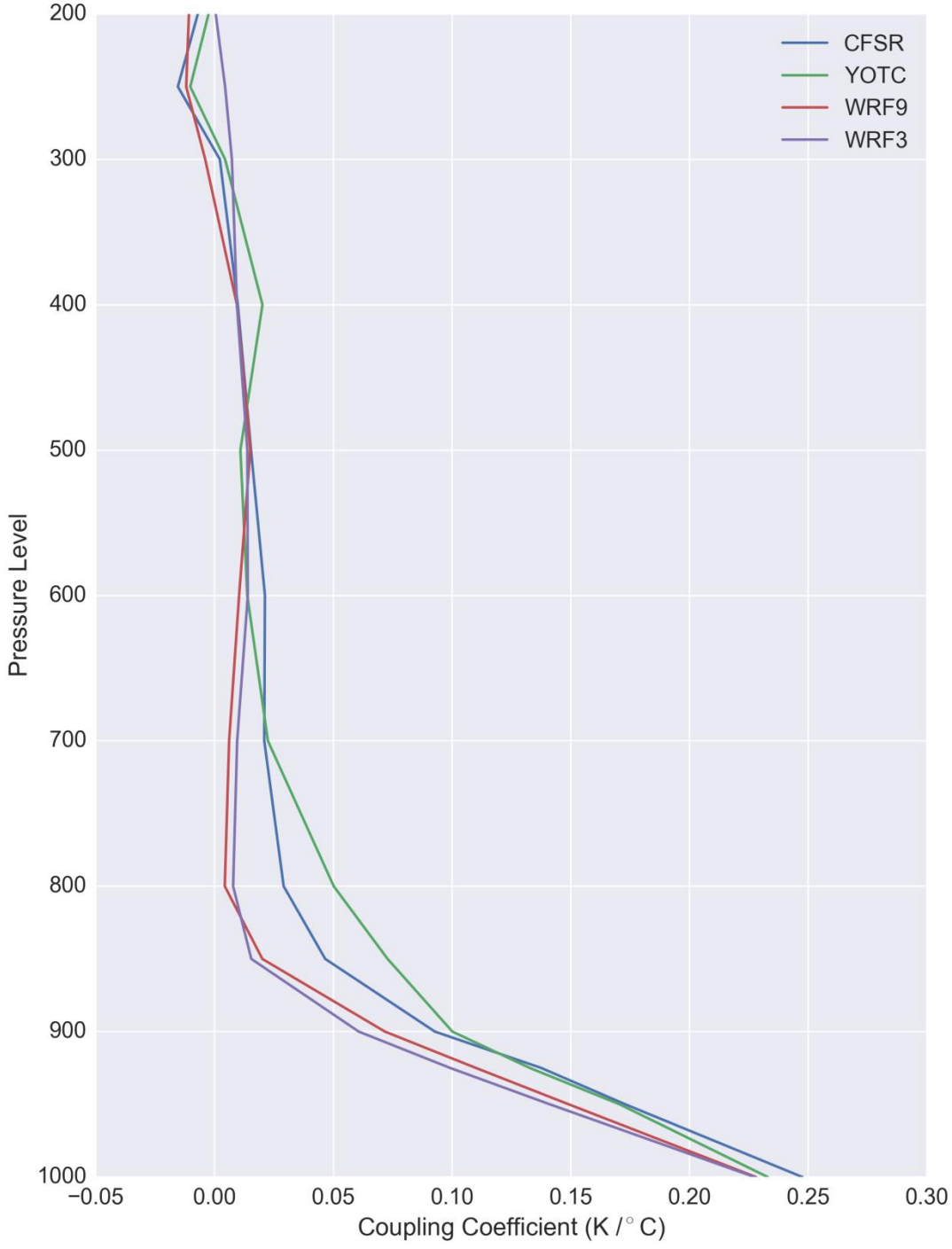

Figure 4.3. The ratio between potential temperature anomaly differences and SST anomaly differences between eddy types, which serves as a rough coupling coefficient.

The difference between eddy types for the U-wind component (Figure 4.4) shows the winds being increased close to the surface over the eddy's center. However, winds are being decreased at vertical levels 925 hPa to 800 hPa, beyond the boundary layer. This is a manifestation of the vertical mixing mechanism, and results in sinking air upstream of the eddy center and rising air downstream. A similar result can be found in Bourras et al. (2004), which studied the atmospheric response to an individual oceanic eddy. The anomalies are approximately 2.5% compared to the background mean, so they are not large, however.

A more detailed vertical profile of the U-wind component is shown in Figure 4.5. Unlike the potential temperature profile, this plot shows the vertical changes directly over the eddy center. The horizontal wind anomaly difference is strongest near the surface but then switches to being slightly negative above 925 hPa. Negative influence continues until 700 hPa for both reanalysis and model data, except for the WRF 3 km run. The model results are very similar to each other near the surface but differ some above the boundary layer, with less negative influence occurring in the WRF 3 km. A vertical dipole in horizontal wind speed is expected with the vertical mixing mechanism, since the horizontal momentum is being transferred down to the surface.

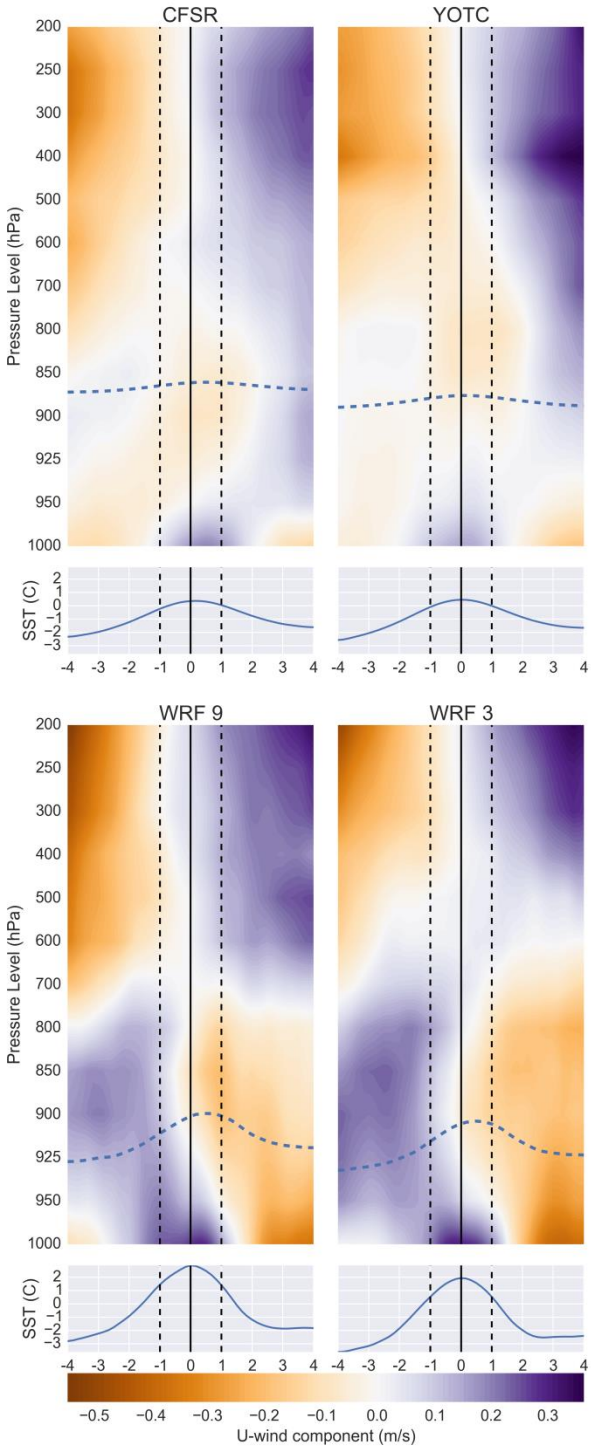

Figure 4.4. Same as Figure 4.1, except for the horizontal U-wind component.

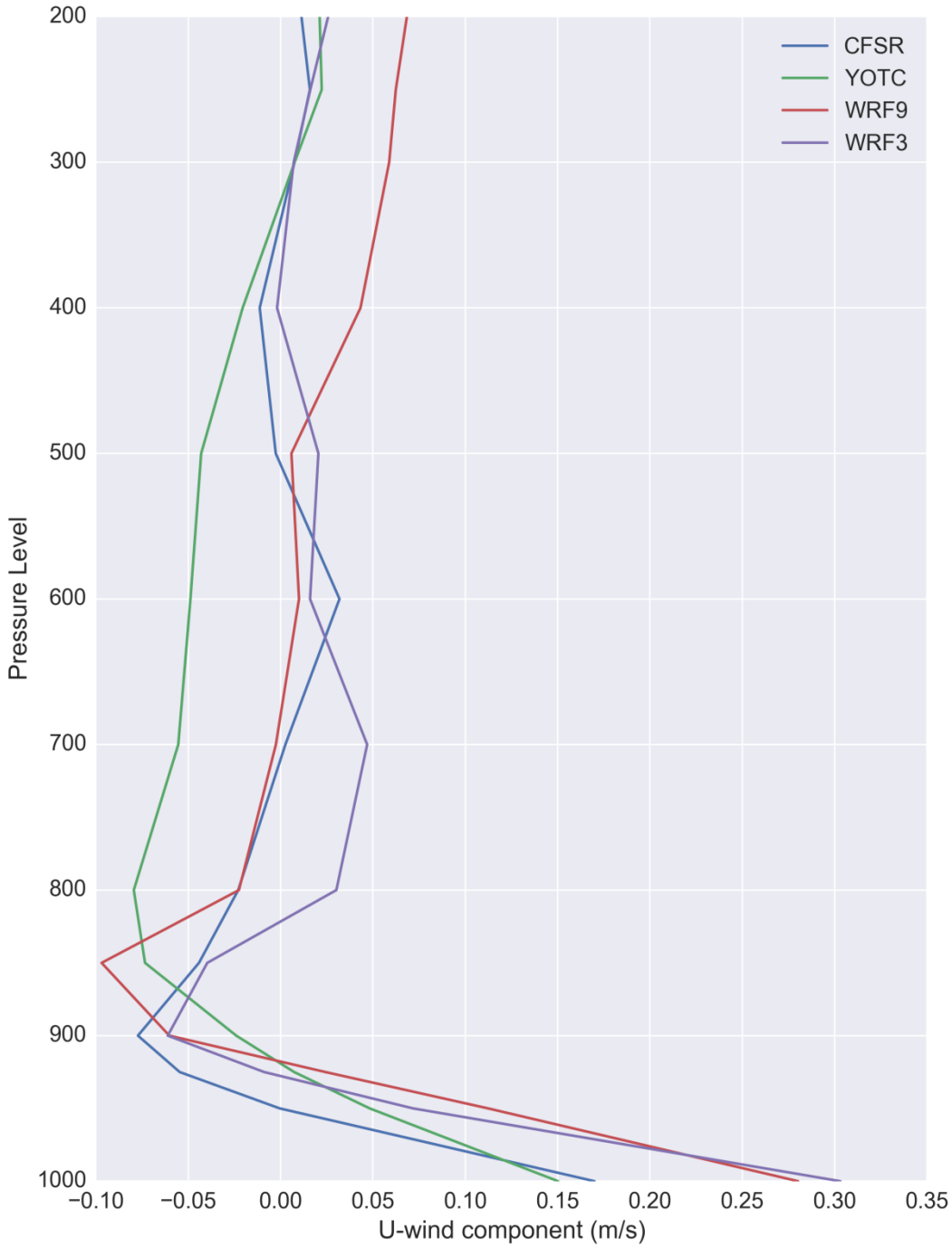

Figure 4.5. Same as Figure 4.2, except for the U-wind component and being directly over the eddy center.

For the associated coupling coefficients, the CFSR results were of the greatest magnitude in the lower atmosphere below the boundary layer (Figure 4.6). This is somewhat surprising, since the CFSR had the coarsest resolution of all at 0.5^{o} and lower resolutions tend to underestimate the wind coupling at the surface (Bryan et al. 2010). It also shows the vertical mixing more clearly, with winds being increased near the surface and decreased above 950 hPa. As expected, the strongest coupling strength is near the surface, with coefficients ranging from 0.08 to 0.13 at 1000 hPa and -0.02 to -0.06 at 900 hPa.

For the horizontal momentum, it is also informative to show these vertical composites separately by eddy type in order to gain further insight. Figures 4.7-4.8 show the vertical composites for warm core only and cold core only, respectively. To better display results near the surface, the color range has been limited so that values beyond the range are saturated. It can be seen in comparing the two figures that the response is actually asymmetrical in the WRF results. For warm core eddies, U-wind anomalies are positive throughout the boundary layer in the two WRF runs. However, in cold core eddies, U-wind anomaly influence is restricted to below 950 hPa. This may imply that the vertical mixing mechanism is less active in warm core eddies than cold core eddies since a reduction in horizontal momentum close to the boundary layer height is missing from these results. However, in the difference plot from Figure 4.4, warm core eddies have smaller horizontal momentum anomalies near the top of the boundary layer. This indicates horizontal momentum is still reduced in the atmosphere above warm core eddies.

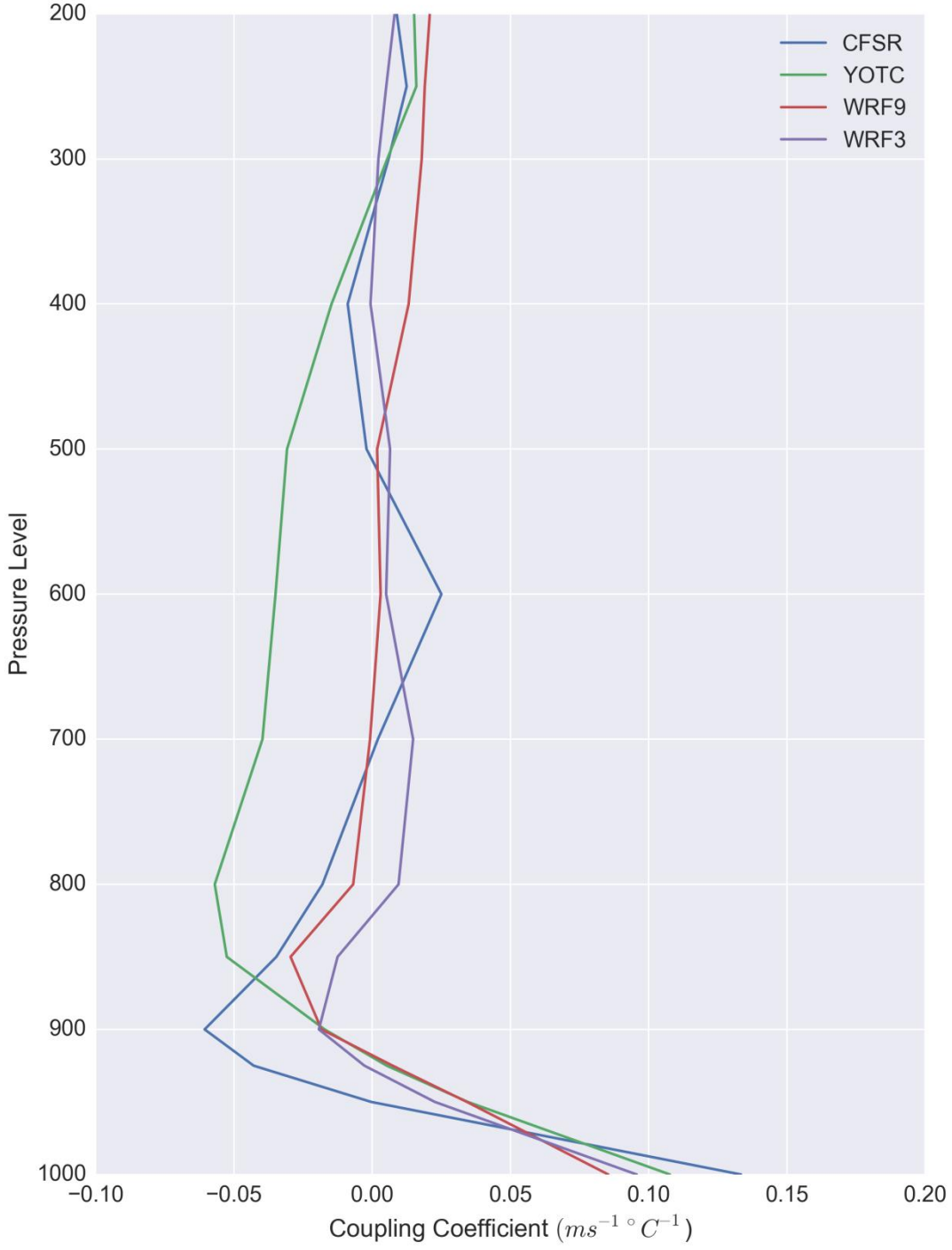

Figure 4.6. Same as Figure 4.3, except for the U-wind component and being directly over the eddy center.

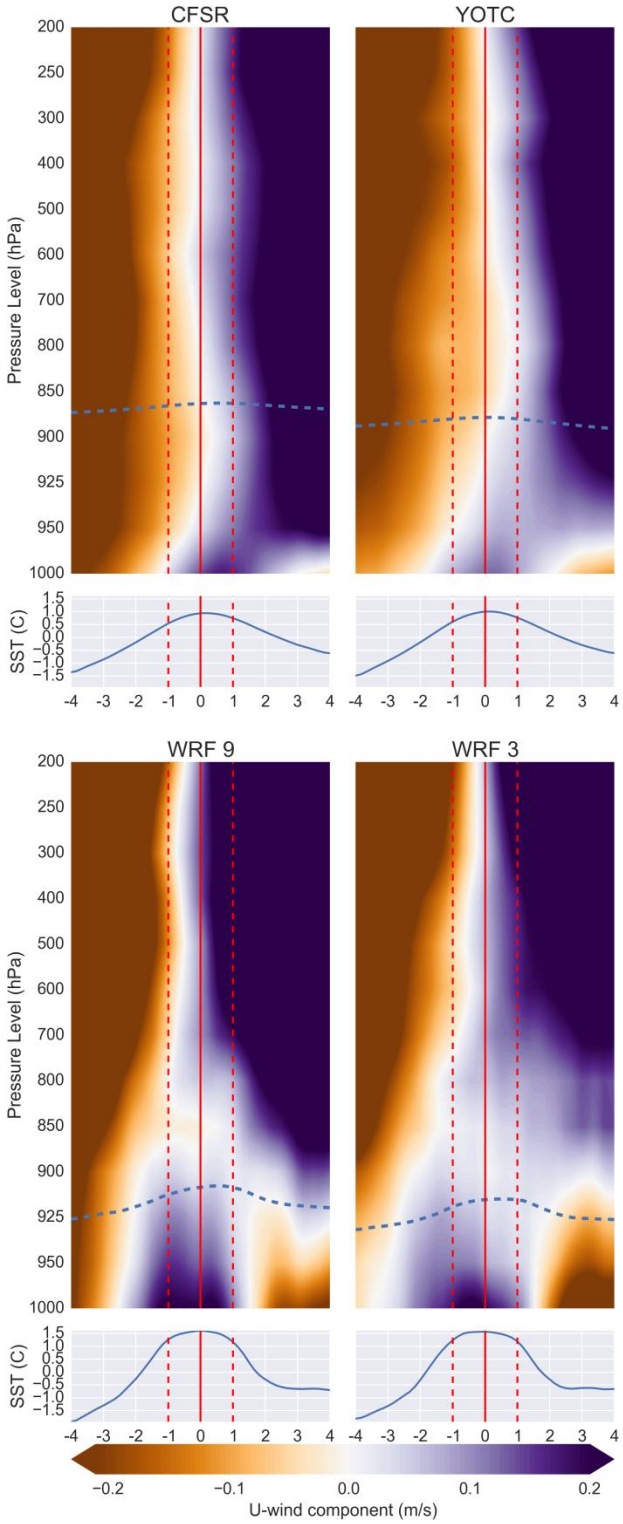

Figure 4.7. Same as Figure 4.4, except for warm core only. The range of contour values has been limited to better show results near the surface.

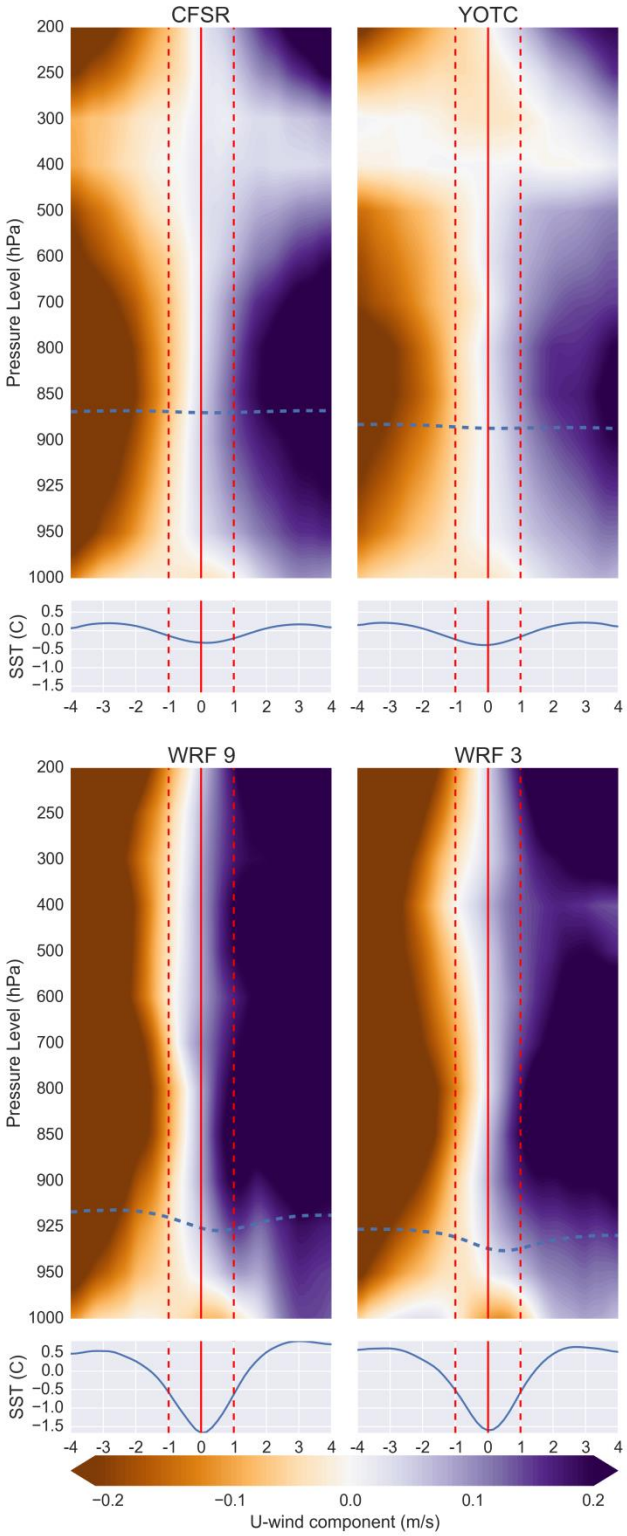

Figure 4.8. Same as Figure 4.7, except for cold core only.

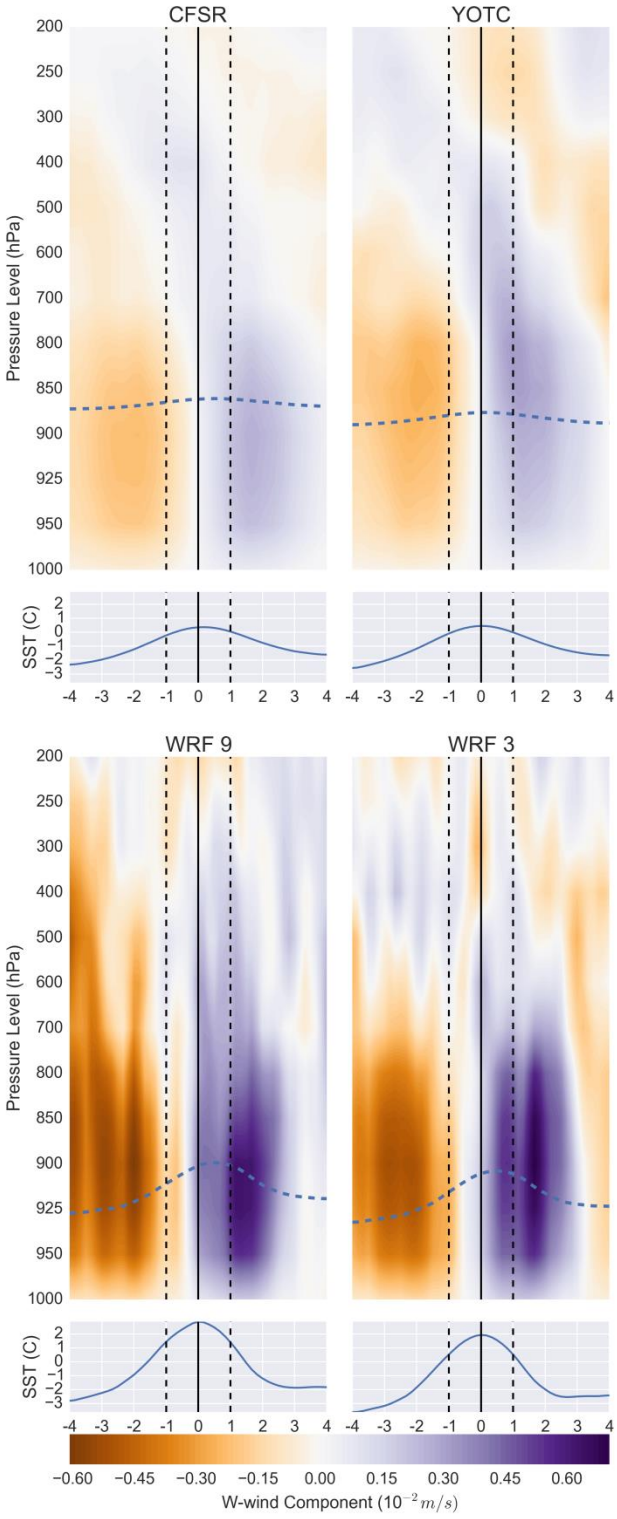

Figure 4.9. Same as Figure 4.1 except for the vertical (w) component of winds.

Vertical mixing as a result of subgrid-scale mixing by the boundary parameterization can be more easily seen in Figure 4.9, which shows anomalies in vertical motion. Negative vertical motion anomalies are dominant upstream of the eddy in terms of the difference between warm core and cold core types. A more concentrated local maximum exists downstream of the eddy, about one to two eddy radii outward. This area aligns well with the increased cloud and rainfall development seen in the previous chapter. The vertical motion anomalies extend primarily up to 800 hPa, beyond the boundary layer, with limited influence beyond 500 hPa. J. Ma et al. (2015) found a similar result, but the positive vertical motion anomalies were more spread out in their case. This is probably due to a difference in methodologies more than a difference in region or seasonality. Similar to the results shown so far, the anomalies were strongest for the high-resolution WRF runs.

The associated vertical profile of the W-wind component one eddy radius downstream of the eddy center is shown in Figure 4.10. The difference between the WRF runs is very small until 700 hPa where a difference between the two becomes more apparent. The WRF 9 km run especially seems to show an influence on the vertical profile well into the mid-troposphere, although the magnitudes are small (less than 1 cm/s). Three of the datasets show a maximum of influence at 900 hPa, while the YOTC peaks later at 800 hPa.

Coupling coefficients for the W-wind component at the same location are shown in Figure 4.11. Here the coefficients are very similar between the WRF runs and CFSR, especially below 900 hPa. The YOTC data had the strongest coupling coefficient

overall, and it peaks higher in the atmosphere at 800 hPa. Unlike the U-wind component, vertical velocity coefficients do not approach zero until much higher in the atmosphere (around 400 hPa), which shows that the eddy influence is more important for vertical mixing instead of horizontal flow at higher altitudes one eddy radius downstream.

Wind divergence (Figure 4.12) anomalies were not present with any significant magnitude in the upper troposphere, indicating a lack of deep convection. Most significant wind divergence is limited to below the boundary layer, although some convergence occurs just upstream of the eddy center at around 800 hPa. As indicated in the surface results in the previous chapter, divergence primarily occurs upstream of the eddy center, with convergence slightly downstream. The location of maximum convergence matches that found previously in the vertical motion anomalies, showing that the vertical motion is from this surface convergence. After investigating the wind and temperature patterns, the vertical mixing mechanism is now able to be seen clearly as the dominant mechanism for the wind response to SST anomalies. Pressure adjustment would not result in this bimodal pattern of divergence and vertical velocity anomalies, especially since these are not aligned with the SST anomaly.

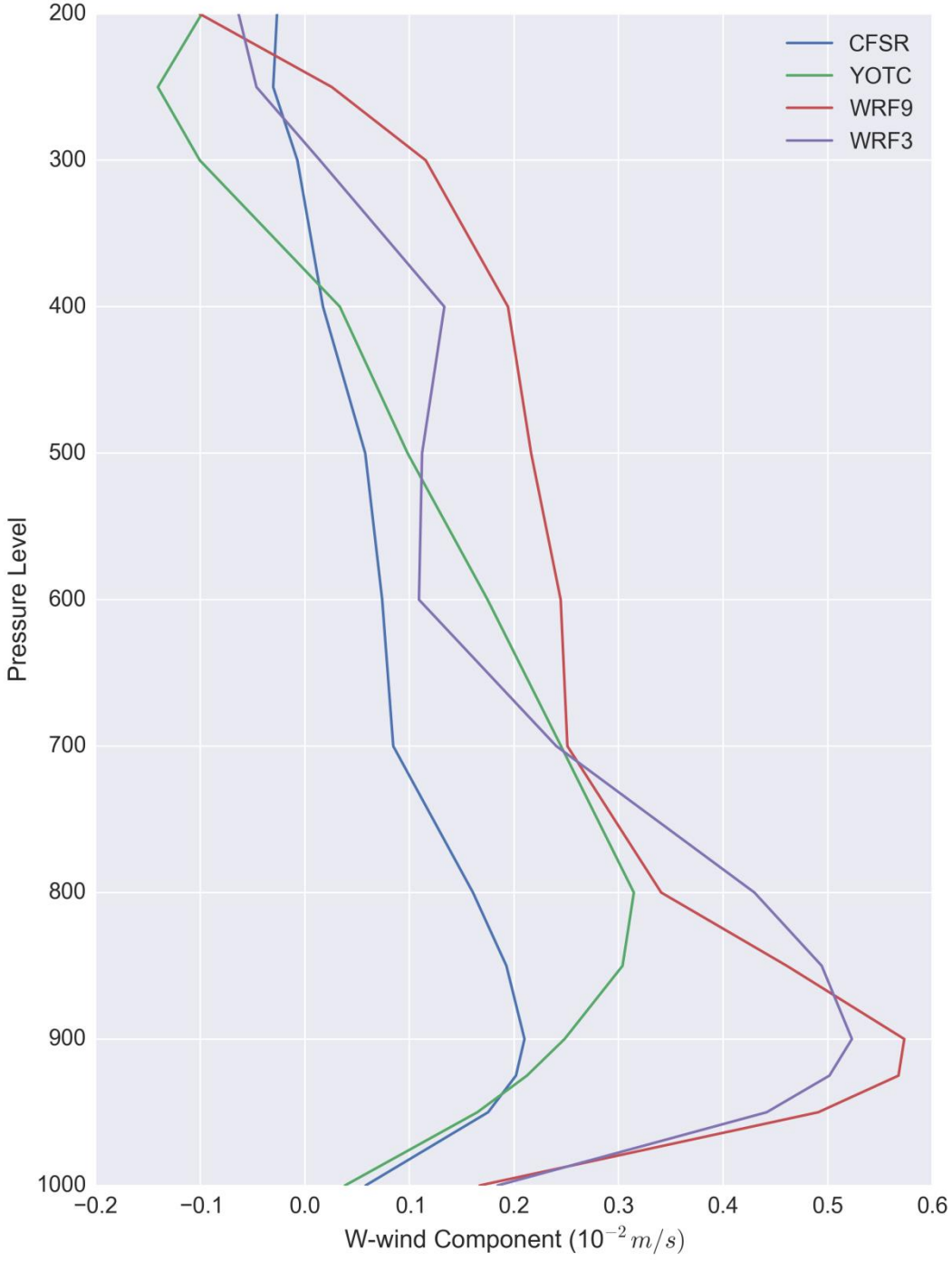

Figure 4.10. Similar to Figure 4.2, except for the W-wind component. The vertical profile is centered one eddy radius downstream of the eddy center.

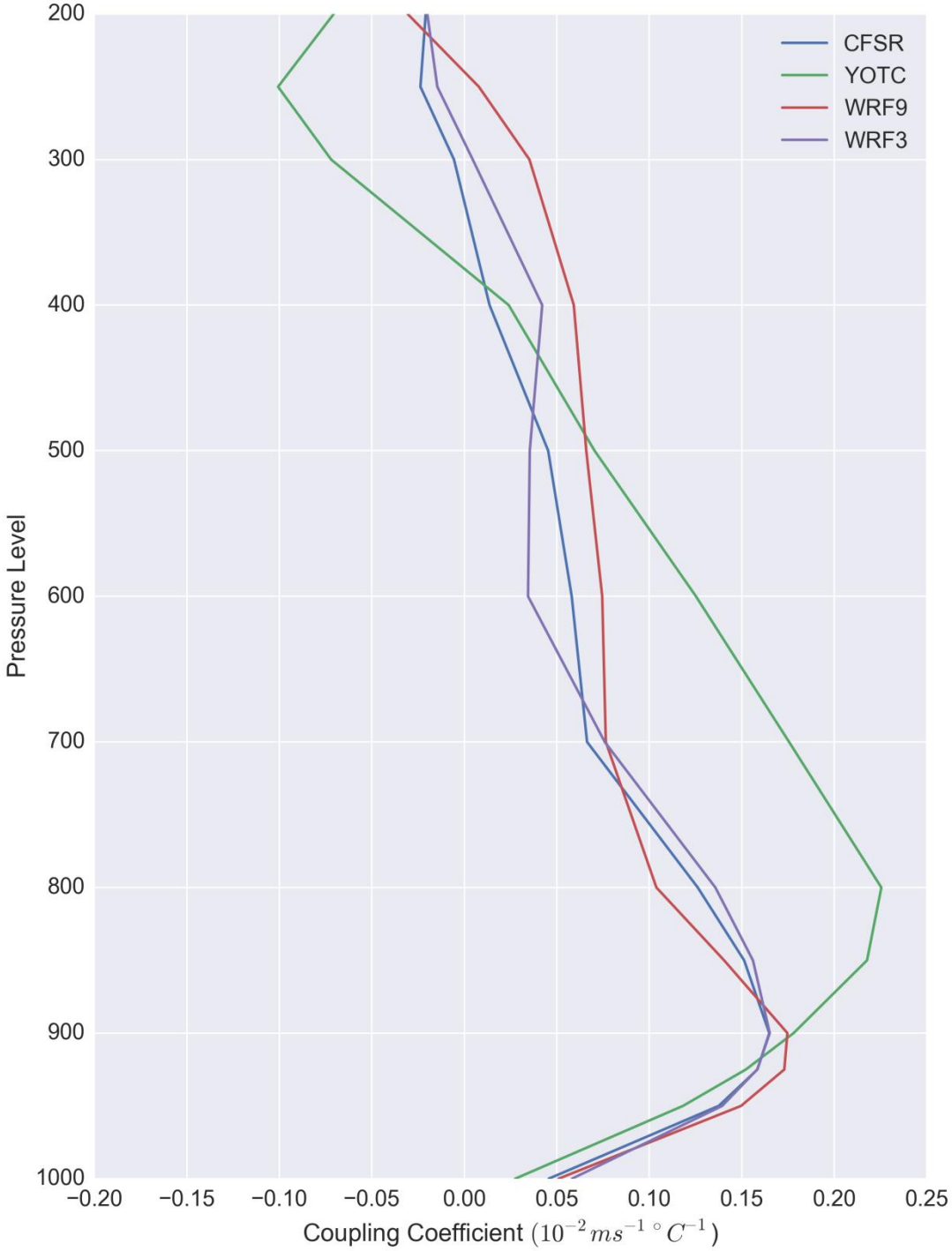

Figure 4.11. Similar to Figure 4.3, except for the W-wind component. The vertical profile is centered one eddy radius downstream of the eddy center.

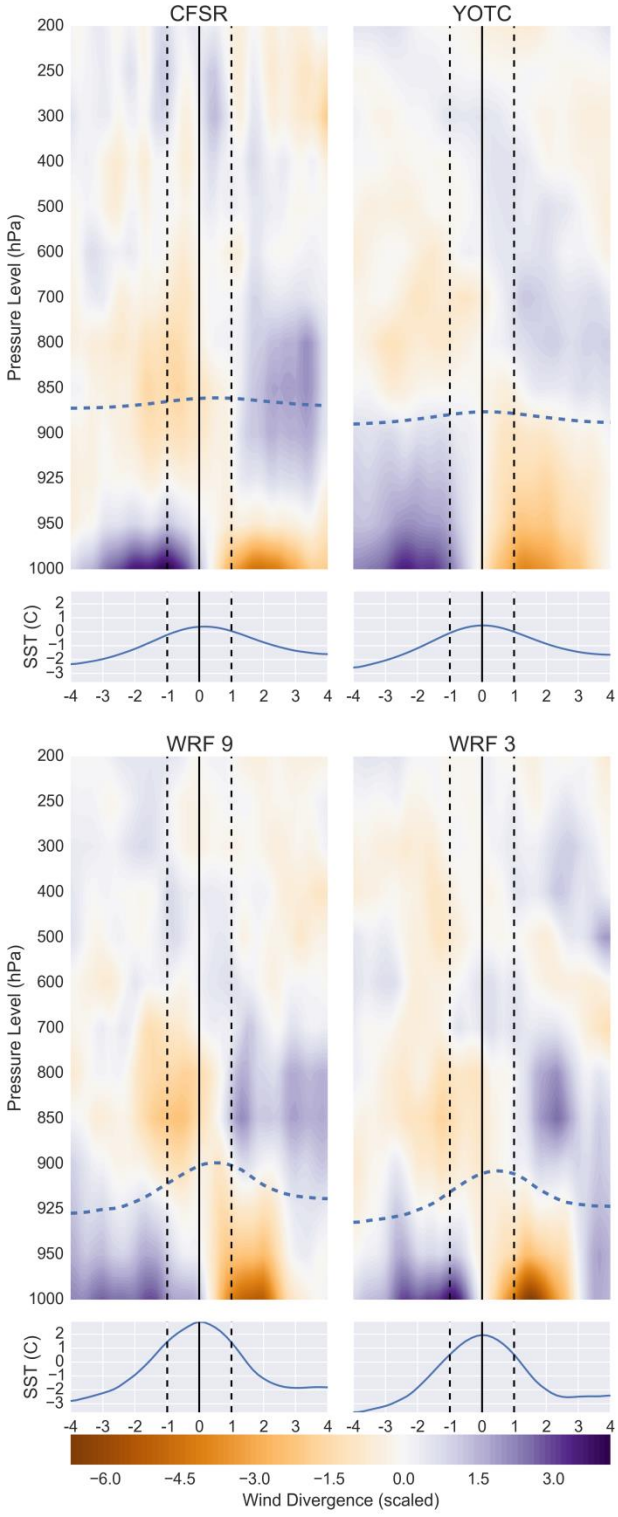

Figure 4.12. Similar to Figure 4.1 except for wind divergence. For visualization purposes, the anomalies were scaled to a mean of zero and standard deviation of one.

For further evidence of how deep the eddy influence goes into the atmosphere, it is useful to also examine convection and moisture. Specific humidity (Figure 4.13) anomalies show where moist air is being transported in response to the oceanic eddy. The two reanalysis sets, being of a more coarse resolution, show negative specific humidity anomalies upwind of the eddy and positive anomalies downwind, with a maximum in the anomaly centered at one eddy radii from the center. This result seems restricted to the boundary layer. By contrast, in the WRF results, it is possible to see a column of greater specific humidity anomalies more easily. The anomalies extend slightly deeper into the atmosphere in the WRF 9 km case, where convective parameterization was being used. In both WRF cases, the anomalies extend slightly above the boundary layer but end at approximately 875 hPa. These anomalies are 7 percent compared to the background, with slightly lower percentages of 5.9 and 4.5 for the CFSR and YOTC respectively.

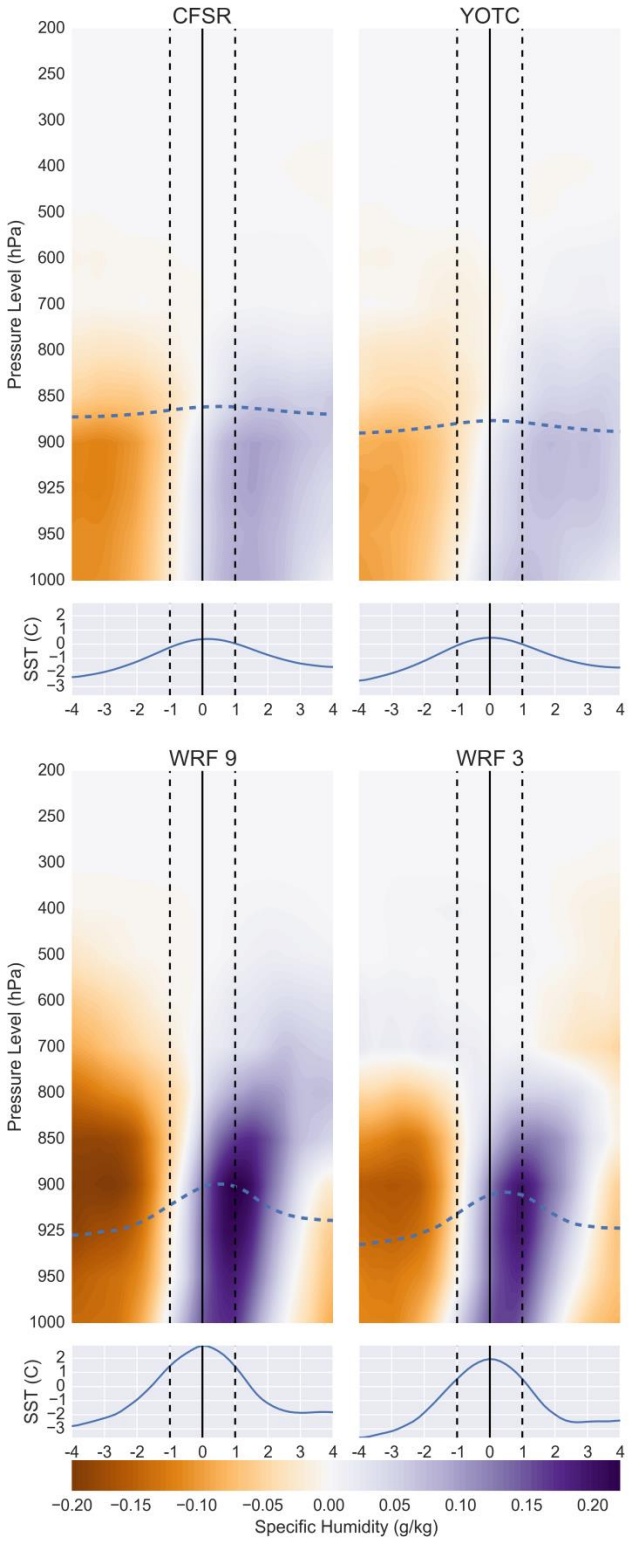

Figure 4.13. Similar to Figure 4.1 except for Specific Humidity.

The vertical profile of specific humidity centered at one eddy radius downstream is shown in Figure 4.14. Due to the greater SST anomalies at the surface, the two WRF model runs have the greatest difference in specific humidity anomalies, peaking at 900 hPa, very close to the top of the boundary layer. The greatest specific humidity difference in the reanalysis datasets is closer to the surface at 1000 hPa, indicating that the vertical transport of specific humidity is stronger in the models. The influence seems to drop sharply past the boundary layer, however, with the eddy influence decreasing to zero by 700 hPa.

For the coupling coefficients of specific humidity (Figure 4.15), CFSR shows the greatest coefficient, which peaks at about 925 hPa. Both models have a maximum influence at 900 hPa, but the maximum for YOTC was lower at 1000 hPa. Overall, YOTC showed the weakest coupling strength and CFSR showed the strongest. In this sense, the models were more similar to CFSR. At 700 hPa, WRF 9 km still shows a weak influence, whereas the other three datasets have approached zero.

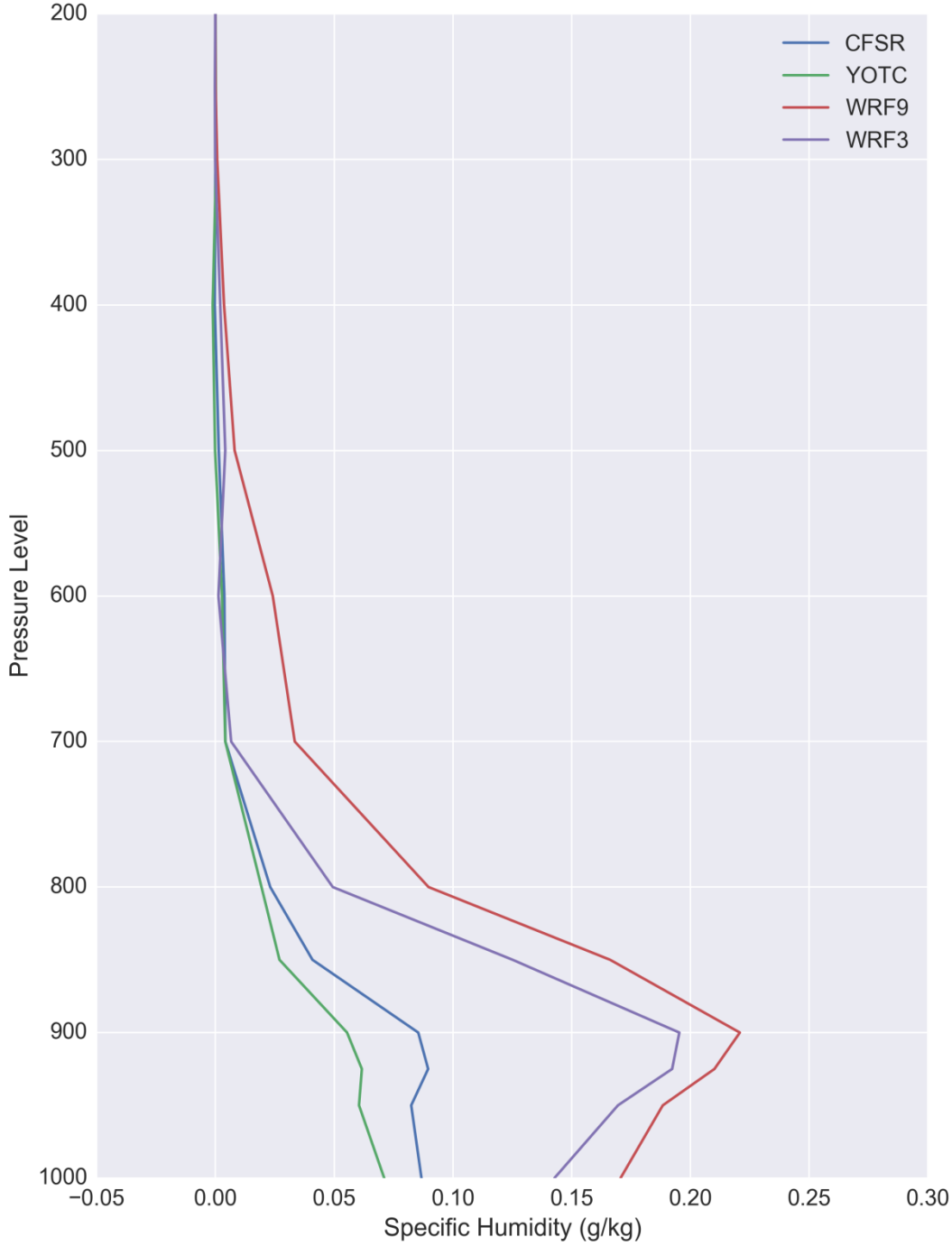

Figure 4.14. Similar to Figure 4.2, except for specific humidity. The vertical profile is centered one eddy radius downstream of the eddy center.

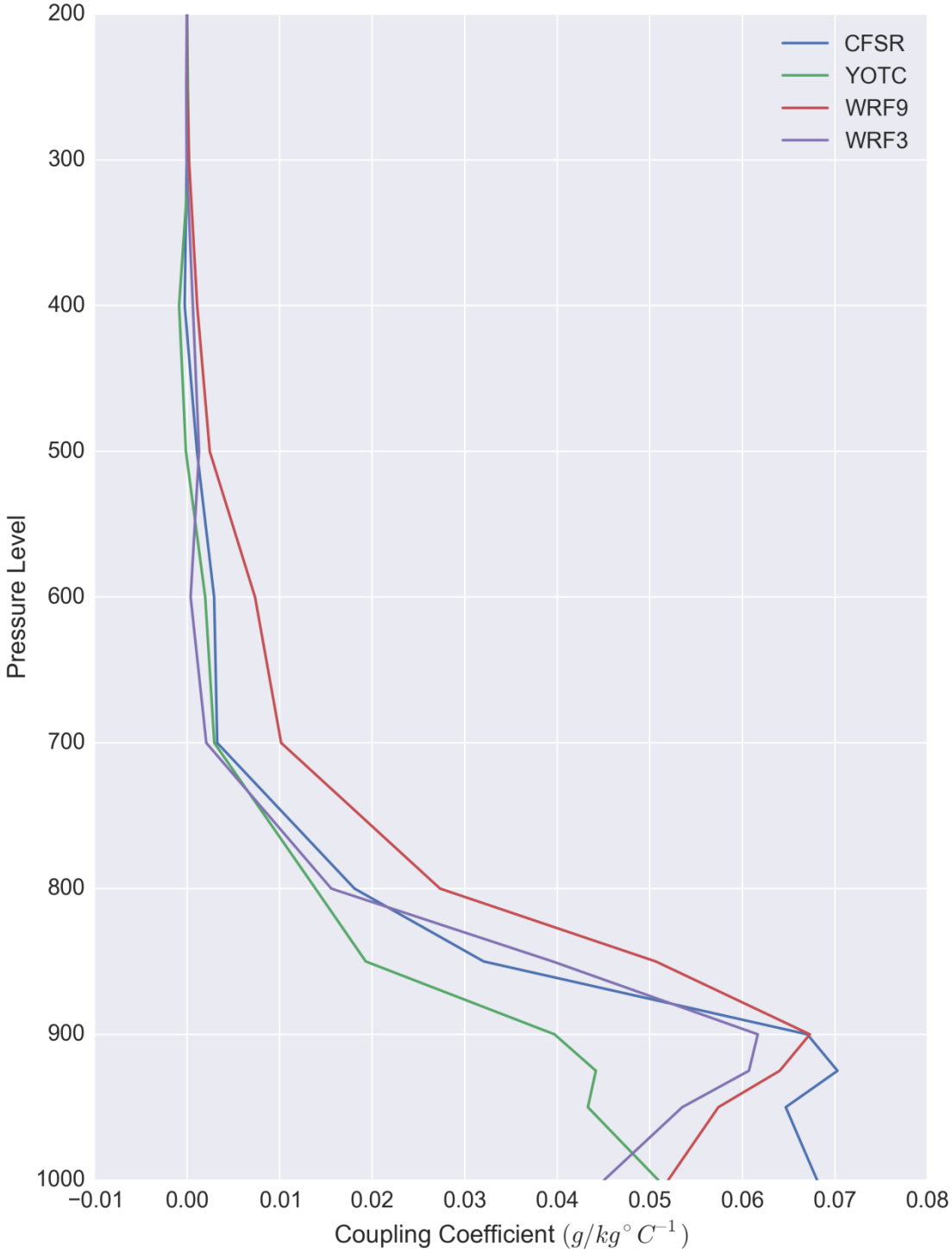

Figure 4.15. Similar to Figure 4.3, except for specific humidity. The vertical profile is centered one eddy radius downstream of the eddy center.

From the previous chapter, it was shown that the overall cloud fraction (solar surface flux) tended to have a maximum positive/negative anomaly just downstream of the eddy center in warm core eddies. However, the vertical level of cloud formation was not indicated in those results. Figure 4.16 shows the vertical profile of cloud fraction for both reanalysis sets and WRF runs. In CFSR, cloud fraction was not available at specific levels, so cloud vapor mixing ratio is used instead as a proxy. As indicated from the specific humidity figures, cloud formation response to the eddies is limited to just beyond the boundary layer centered at 850 hPa. The clouds form downstream of the eddy in all cases, matching the surface results found in the previous chapter.

While the CFSR data show a greater anomaly in cloud vapor mixing ratio slightly more downstream than the WRF results, the vertical level at which the clouds form is very consistent. The anomalies are slightly weaker in the WRF run with the 3 km inner nest, which could be due to convective parameterization being turned off and not triggering cloud formation as often. These anomalies are still of greater magnitude than the more coarse YOTC, although the locations of the anomalies are the same. This implies that an increase in resolution results in a stronger atmospheric response. The anomalies of warm core and cold core eddies separately, averaged together, in CFSR and the WRF 3 km were 17.5 percent compared to the background, with lower percentages of 11.6 and 14.9 in the YOTC and WRF 9 respectively.

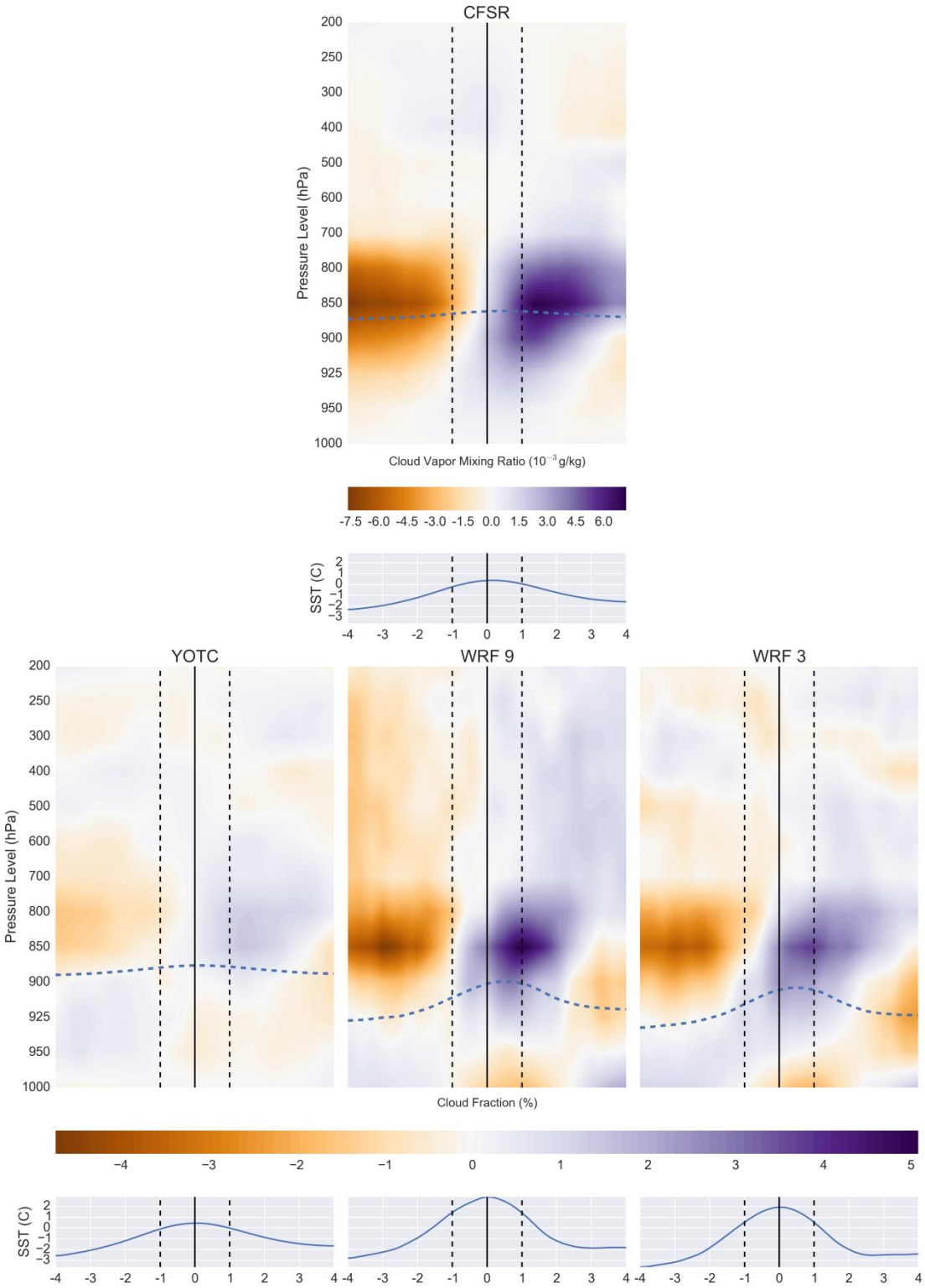

Figure 4.16. Similar to Figure 4.1 except for cloud fraction. Cloud vapor mixing ratio is displayed instead for CFSR due to a lack of cloud fraction data saved at each pressure level.

The vertical profile of cloud fraction at one eddy radii downstream is shown in Figure 4.17. In every case, the anomaly difference peaks at 850 hPa. This consistency between model results and reanalysis data is striking, giving greater confidence to the idea that warm core eddies increase low-level cloud development near the boundary layer. As with most of the other physical parameters investigated, the influence decreases to zero beyond 700 hPa. The influence for YOTC was much less than those found in the WRF results or CFSR.

The associated coupling coefficients for cloud fraction are shown in Figure 4.18. Since the SST anomaly magnitudes are smaller in the YOTC, the coefficients are more similar in magnitude now compared to the WRF model runs. The coupling strength is always greatest at 850 hPa, with the greatest coupling coefficient found in the WRF 9 km run of 1.6% $^{o}C^{-1}$. The magnitude of the YOTC's coupling coefficient is about half as much at 0.8% $^{o}C^{-1}$, so it is possible the WRF runs are overestimating the coupling strength.

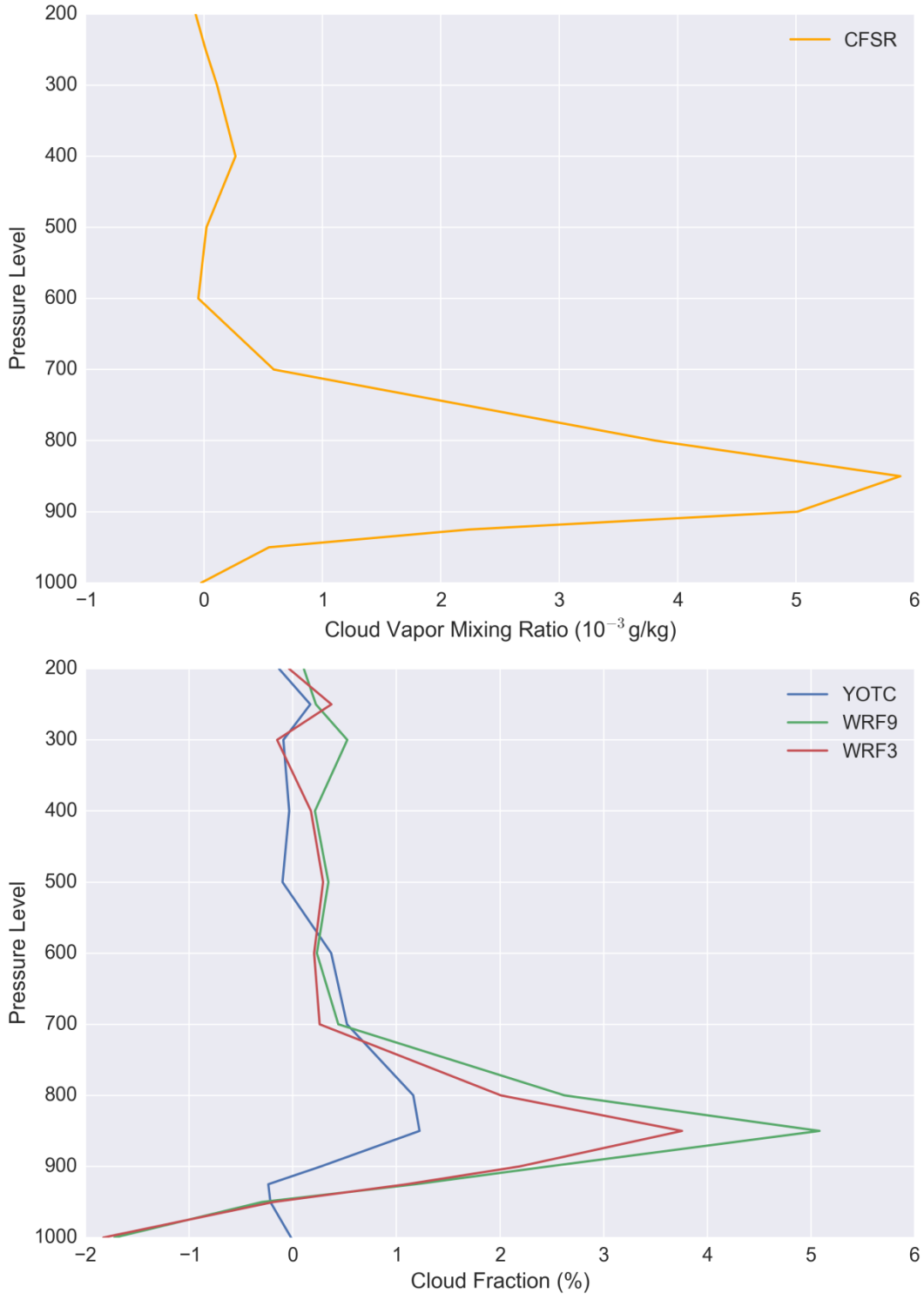

Figure 4.17. The vertical profile of cloud fraction (cloud vapor mixing ratio) anomaly differences between eddy types centered at one eddy radii downstream of the eddy center.

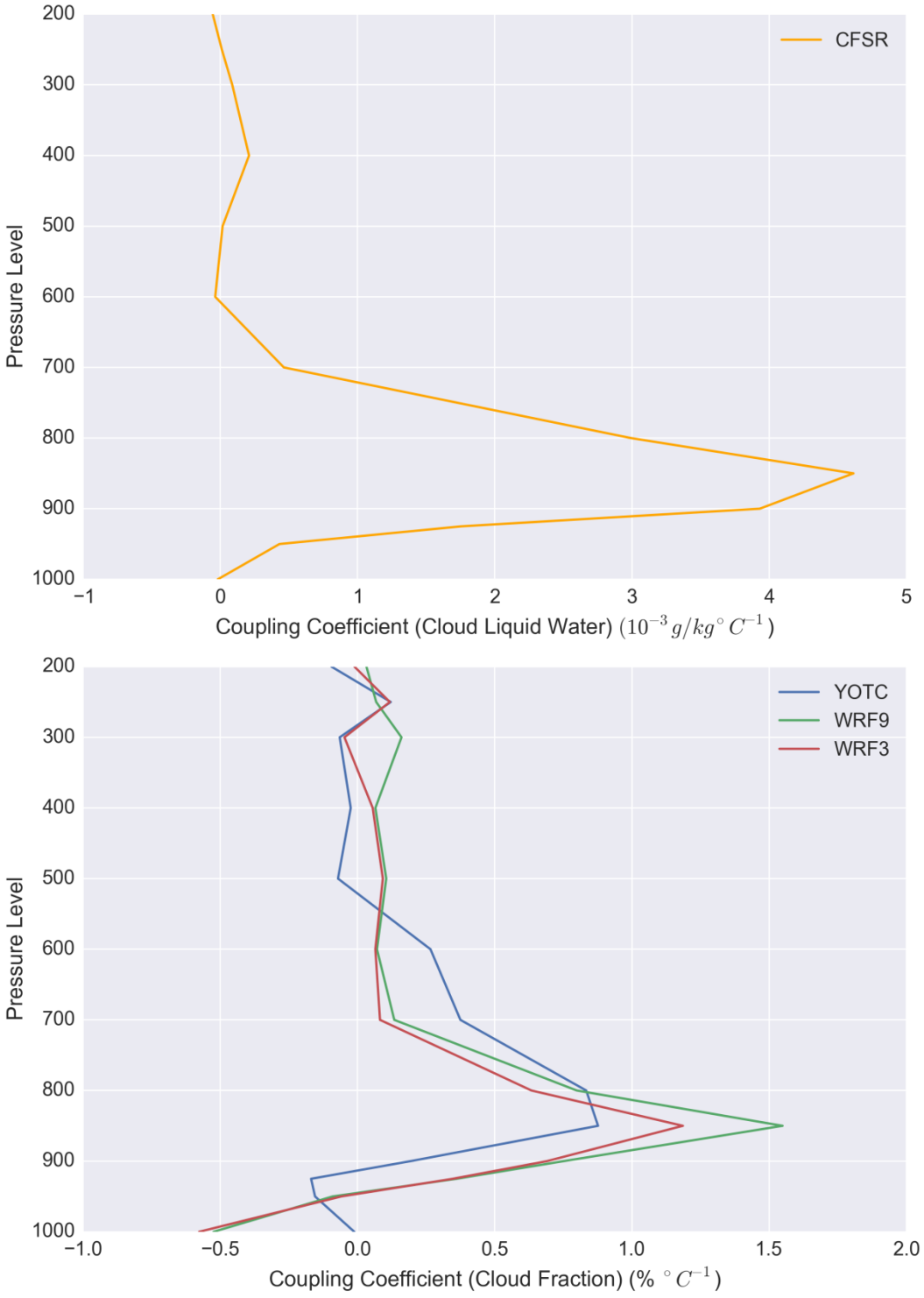

Figure 4.18. Similar to Figure 4.17 except for coupling coefficients.

Separate vertical composite profiles for warm and cold core are shown in Figures 4.19 and 4.20 respectively. The warm core shows a cloud layer increase at 850 hPa similar to the cold core showing a decrease in the cloud layer at the same pressure level. Negative anomalies for cloud formation extend downwards toward 900 hPa in cold core eddies. In warm core eddies, however, cloud formation influence is also found up to 800 hPa. This difference in the pressure level of influence is consistent with the deepening of the boundary layer found in response to warm core eddies and the shallowing of the boundary layer in response to cold core eddies.

4.3 Conclusions

This chapter showed the vertical profile of the atmosphere's response to oceanic eddies. Further confirming the work in the previous chapter, the vertical mixing mechanism can explain the wind response to SST anomalies located at the eddy's center. Warm core eddies result in an increase of wind speeds in both the horizontal and vertical directions downstream of the eddy center. This result can also be seen in the vertical transport of moisture and cloud formation over the same locations. Although the CFSR is at a much coarser resolution than the WRF models, it showed atmospheric responses at the same locations.

The vertical mixing mechanism was seen as the dominant mechanism for the wind response to SST anomalies. Given the positive vertical velocity anomalies downstream and negative vertical velocity anomalies upstream, it seems the winds

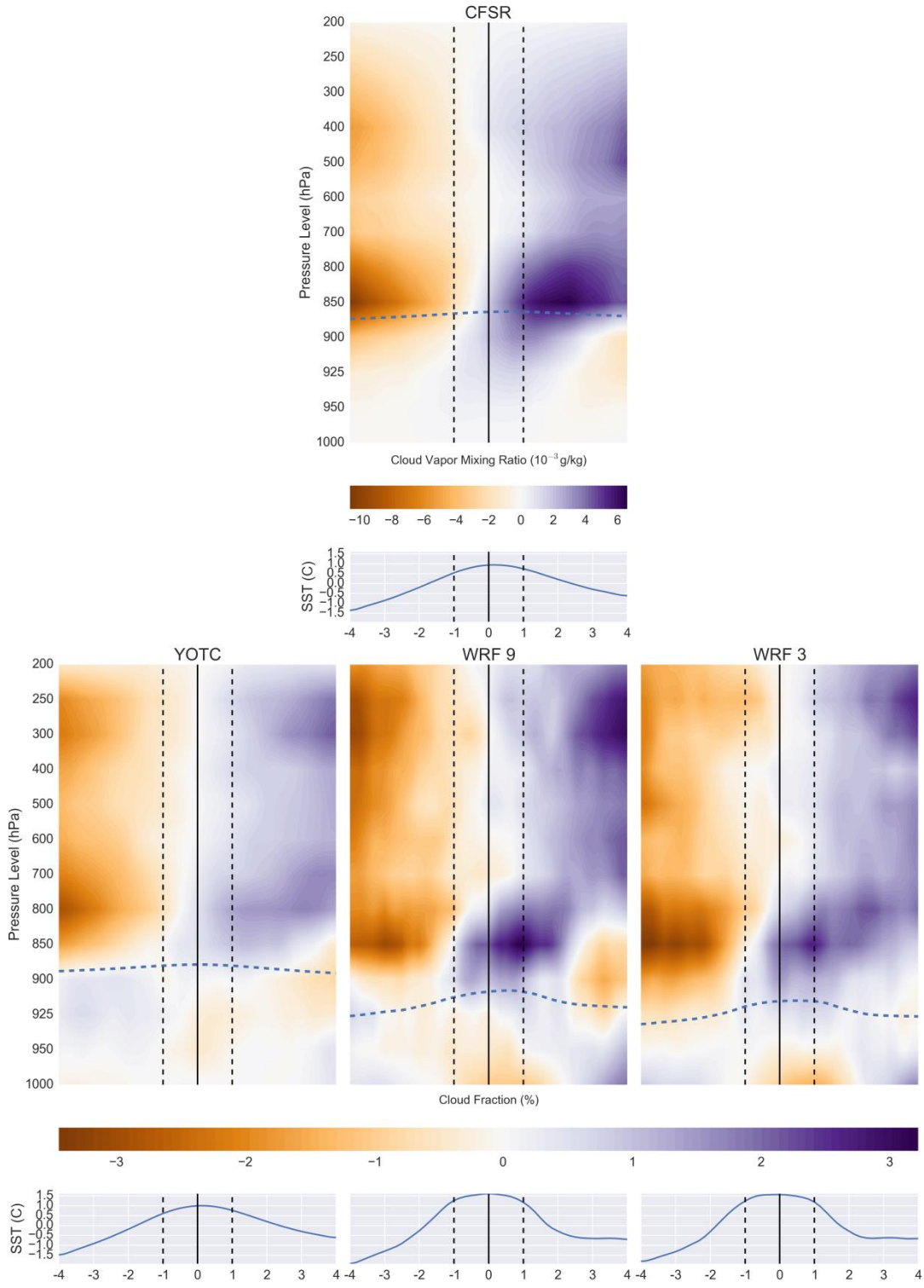

Figure 4.19. Similar to Figure 4.16, except for warm core only.

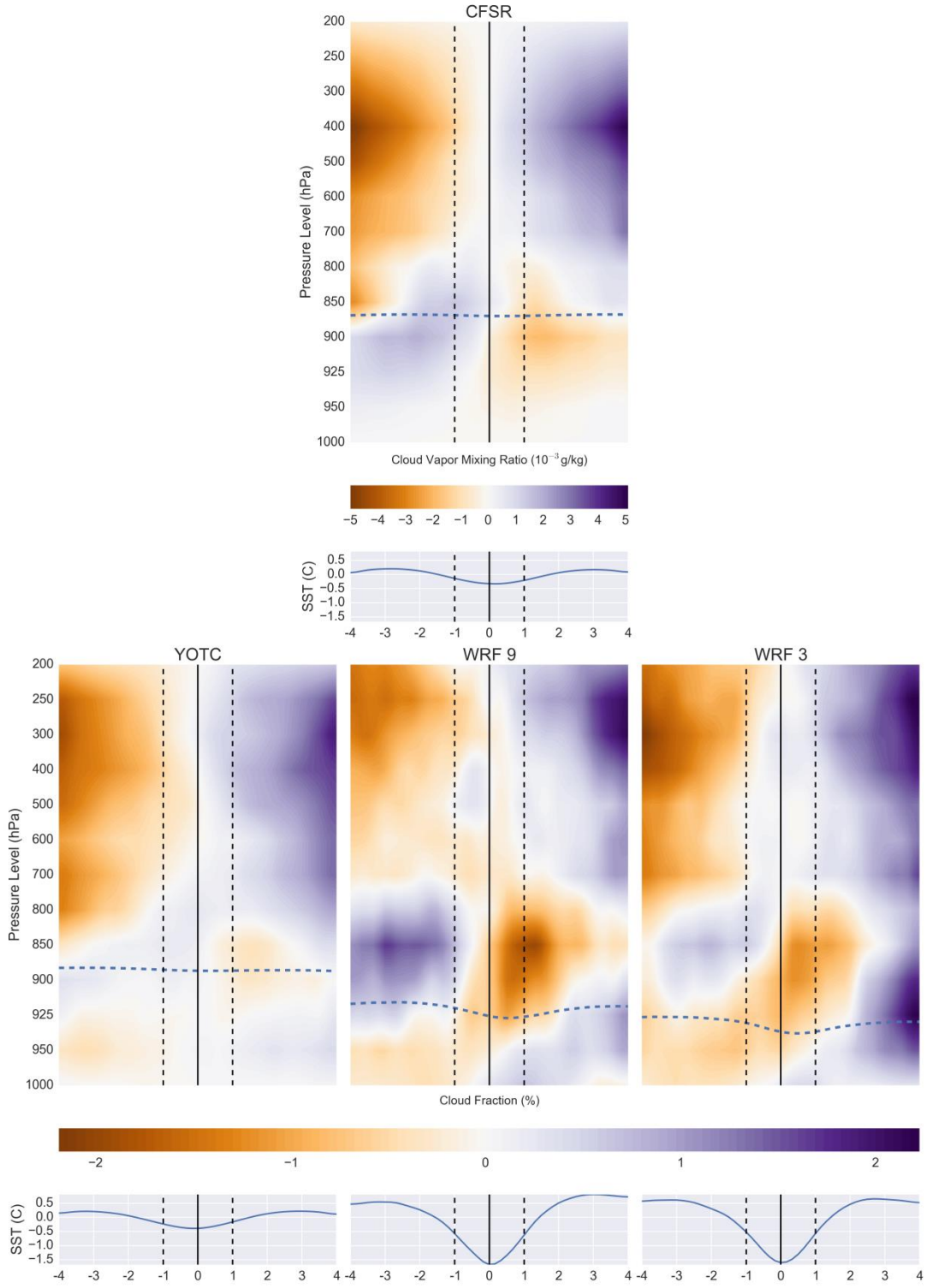

Figure 4.20. Similar to Figure 4.16, except for cold core only.

higher in the atmosphere, near the top of the boundary layer, are being moved down towards the surface. This helps explain why the horizontal cross-frontal winds over the SST anomaly are increasing near the surface but are decreasing in the top of the boundary layer. If the wind speed increase near the surface over the SST anomaly was simply due to pressure adjustment, there would be no noticeable change in wind speeds near the boundary layer height.

Although some atmospheric response was found beyond the boundary layer, such as with vertical velocity anomalies, most of the atmospheric response to oceanic eddies seems to be restricted to lower levels, near and within the boundary layer itself. Given the small spatial size of these individual eddies and the relatively small magnitude of the associated SST anomalies compared to much larger SST fronts, this is not surprising. A possible explanation is that the weaker winds near the surface allow greater vertical transport over the eddy's location, while stronger winds in the free atmosphere push the influence further downstream. However, an atmospheric response to oceanic eddies does exist, and it can be seen in winds, temperature, convection, and the transport of moisture.

5. CONCLUSIONS

This study's focus was an investigation of the atmospheric response to oceanic eddies. The North Atlantic region was chosen since oceanic eddy influence had not yet been thoroughly investigated here. Coupled models were used to investigate the response not only near the surface but also in the vertical beyond the boundary layer. In order to quantify this response, oceanic eddies were identified using an automated eddy detection algorithm based on SLA data. The original detection algorithm was originally too sensitive and had to be tuned for better performance. The tuning allowed smaller eddies to still be detected while keeping the detected features in relatively close proximity to the Gulf Stream.

Atmospheric data was then collocated with each detected eddy's location to investigate the response. The strength of the atmospheric response based on the SST anomaly found in each eddy was calculated, along with composites that highlight the difference in atmospheric response based on eddy type (warm core or cold core). The atmospheric response was measured in observations and reanalysis data, along with a global coupled GCM and a coupled regional model with varying atmospheric resolution. For the reanalysis data and models, vertical profiles of the response were generated to better analyze how deep into the atmosphere the eddy's influence exists.

While some influence from oceanic eddies on vertical motion was evident at greater altitudes, the oceanic eddy influence on the atmosphere is mostly limited to the boundary layer, as signs of deep convection were not found in this study. Low-level

clouds were found to develop at a greater rate in response to warm core eddies, with cloud fraction being reduced in response to cold core eddies. Clouds formed consistently at a height near 850 hPa in both the reanalysis datasets and both WRF runs. Given that low-level marine clouds are a primary source of uncertainty in climate model sensitivity (Sherwood et al. 2014), including eddy-resolving resolutions that can accurately model the atmospheric response to oceanic eddies may help to reduce some of the variance in model results.

In previous studies, if a model is not of an eddy resolving resolution, it tends to underestimate the coupling strength between SST and other atmospheric variables (Bryan et al. 2010, Iizuka 2010, Chelton and Xie 2010). In the case of the current study, the coupling strength between SST and the atmospheric response was actually overestimated compared to observations based on the surface wind and rainfall rate coupling coefficients. This could be due to the observational data in this study having a resolution that is effectively coarser, since the satellite data would need to be spatiotemporally averaged and blended. Both WRF runs, regardless of the inner nest or convective parameterization, were able to see the atmospheric response with little difference between the two. Therefore, parameterization of convection is sufficient to resolve the atmospheric response.

In terms of which mechanism dominated the wind response to SST anomalies, evidence for the vertical mixing mechanism was the strongest. There was a dipolar pattern to the SST gradient and wind divergence at the surface, indicating convergence that is not occurring directly over the eddy center. In addition, the vertical profile of

wind shows negative vertical velocity anomalies upwind of the eddy center, and positive vertical velocity anomalies downstream. Combined with the increased horizontal wind component near the surface and a reduced horizontal component near the boundary layer in the difference composites, the vertical mixing mechanism is given even further weight. Warm core eddies seemed to show limited support for the vertical mixing mechanism when viewed independently, however. No significant anomaly of sea level pressure was found as a response to the SST anomalies, concurring with the results in other studies on atmospheric response to oceanic mesoscale eddies (Frenger et al. 2013, Byrne et al. 2015, J. Ma et al. 2015).

In terms of the location of rainfall and cloud fraction anomalies in relation to the eddy's center, this study can be compared with previous work. Frenger et al. (2013) claims the anomalies occur directly over the eddy center, with J. Ma et al. (2015) seeing mixed results. Byrne et al. (2015) shows the cloud fraction and rainfall anomalies somewhat downstream of the SST anomaly, more so in the warm core case. The current study shows not only with surface composites but also in vertical composites that the cloud cover and rainfall maximum anomalies are located downstream of the eddy center by approximately a single eddy radius. Figure 5.1 summarizes the atmospheric response to warm core oceanic eddies.

While the magnitude of the influence is small, oceanic mesoscale eddies clearly produce an atmospheric response. To correctly simulate this response, it appears utilizing coupled models between the ocean and atmosphere is best, making sure that the oceanic component is eddy resolving (less than 0.25^{o}). Given how

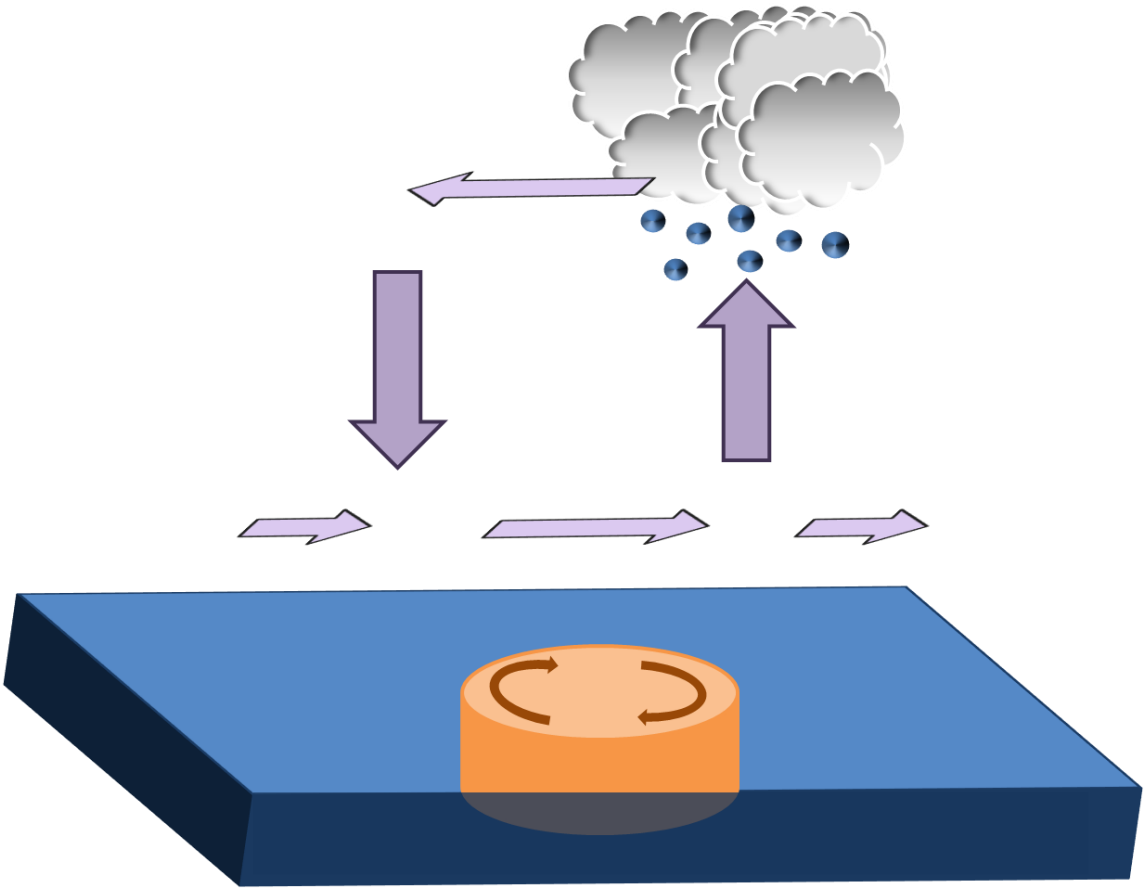

Figure 5.1. A summary of the atmospheric response to a warm core eddy is shown. In the Northern Hemisphere, most warm core eddies have anticyclonic rotation. Winds near the surface increase over the eddy's center, with positive anomalies in vertical wind velocity, cloud fraction, and rainfall downstream of the eddy center. Horizontal winds are decreased near the boundary layer, where cloud formation occurs. Negative anomalies in vertical wind velocity occur upstream of the eddy center. The direction of the mean wind is from the left side of the figure.

ubiquitous oceanic eddies are in several regions of the planet, along with their ability to transport large amounts of energy (Zhang et al. 2014), correctly quantifying the response to this energy transport is likely very important for climate models.

The choices of methodology used in this study could have consequences for the results shown when considering how they compare to previous work. The tuning parameters chosen in the eddy detection algorithm, for example, were optimized for the North Atlantic region only and require some subjectivity that could alter the number of eddies detected as well as their amplitude of SST anomaly. Utilizing the same settings on a different oceanic region could change the number of features that are detected. In addition, subtracting the zonal mean can introduce artifacts upstream and downstream of the maximum anomaly that have the potential to cause misinterpretations of the physical response in the atmosphere compared to no zonal mean subtraction.

Because of the imbalance towards cyclonic eddies seen in this study as well as Kang and Curchitser (2013), it is theoretically possible that the atmospheric response overall is dominated by cold core eddies in the North Atlantic. This would mean that cloud fraction would theoretically be decreased, along with a decrease in rainfall rate, over the Gulf Stream region if eddy formation was frequent. This may cause storm tracks to be shifted as locally colder SST decreases instability near the surface. However, the eddies are relatively small in size. Given the strong influence of the Gulf Stream itself seen by Minobe et al. (2008), and the relatively warm current of SST it carries, the negative influence of cold core eddies on cloud and rainfall production may be balanced

out entirely. This may be especially true in the North Atlantic compared to the Southern Ocean, given that air-sea fluxes are stronger here (Yu et al. 2007).

However, there are some unanswered questions. This study has not directly measured how much of an effect oceanic eddies have upon the atmosphere beyond the immediate area surrounding them, or for long time periods. In order to properly ascertain this, climate models need to be run for an extended period of time in order to measure long-term trends of climate response to oceanic eddies. While in theory the increased levels of low-level cloud formation from warm core oceanic eddies should reduce the overall energy gain of earth's atmosphere, there are also cold core eddies that decrease cloud formation as well to consider. Ideally the atmosphere would be simulated in a coupled GCM of eddy resolving resolution, with one run that allowed oceanic eddy formation and another that had no eddy formation. It would then be interesting to see if the difference in climate were, in fact, practically significant. If it was, this would motivate an effort to utilize coupled GCMs of eddy resolving resolution in the future to reduce the model's bias.

It is also unknown whether eddies in the North Atlantic are capable of altering storm tracks. While this phenomenon has been observed in other studies such as O'Reilly and Czaja (2015) in the Kuroshio Extension region, it has not been studied in the North Atlantic. Given that both regions have similar air-sea fluxes and ample production of eddies, the eddies should be capable of changing the storm tracks. Based on the downstream influence observed in X. Ma et al. (2015) over the U.S. west coast, perhaps oceanic eddies in the North Atlantic can also influence rainfall patterns in

Western Europe and the United Kingdom. Now that the basic mechanics of eddy influence on the atmosphere have been investigated, it can be determined whether this impact is truly local or whether it has far-reaching influence as well.

REFERENCES

Atlas, R., Hoffman, R.N., Ardizzone, J., Leidner, S.M., Jusem, J.C., Smith, D.K. and Gombos, D., 2011. A cross-calibrated, multiplatform ocean surface wind velocity product for meteorological and oceanographic applications. *Bulletin of the American Meteorological Society*, *92*(2), pp. 157-174.

Bourras, D., Reverdin, G., Giordani, H. and Caniaux, G., 2004. Response of the atmospheric boundary layer to a mesoscale oceanic eddy in the northeast Atlantic. *Journal of Geophysical Research: Atmospheres (1984–2012)*, *109*(D18).

de Boyer Montégut, C., Madec, G., Fischer, A.S., Lazar, A. and Iudicone, D., 2004. Mixed layer depth over the global ocean: An examination of profile data and a profile-based climatology. *Journal of Geophysical Research: Oceans (1978–2012)*, *109*(C12).

Bryan, F.O., Gent, P.R. and Tomas, R., 2014. Can Southern Ocean eddy effects be parameterized in climate models?. *Journal of Climate*, *27*(1), pp. 411-425.

Bryan, F.O., Tomas, R., Dennis, J.M., Chelton, D.B., Loeb, N.G. and McClean, J.L., 2010. Frontal scale air-sea interaction in high-resolution coupled climate models. *Journal of Climate*, *23*(23), pp. 6277-6291.

Byrne, D., Papritz, L., Frenger, I., Münnich, M. and Gruber, N., 2015. Atmospheric Response to Mesoscale Sea Surface Temperature Anomalies: Assessment of Mechanisms and Coupling Strength in a High-Resolution Coupled Model over the South Atlantic. *Journal of the Atmospheric Sciences*, *72*(5), pp. 1872-1890.

Carton, J.A., Chepurin, G. and Cao, X., 2000. A simple ocean data assimilation analysis of the global upper ocean 1950-95. Part II: Results. *Journal of Physical Oceanography*, *30*(2), pp. 311-326.

Chelton, D.B., Schlax, M.G., Freilich, M.H. and Milliff, R.F., 2004. Satellite measurements reveal persistent small-scale features in ocean winds. *Science*, *303*(5660), pp. 978-983.

Chelton, D.B., Schlax, M.G. and Samelson, R.M., 2011. Global observations of nonlinear mesoscale eddies. *Progress in Oceanography*, *91*(2), pp. 167-216.

Chelton, D.B., and S.-P. Xie. 2010. Coupled ocean-atmosphere interaction at oceanic mesoscales. *Oceanography*, 23(4), pp. 52–69.

Delworth, T.L., Rosati, A., Anderson, W., Adcroft, A.J., Balaji, V., Benson, R., Dixon, K., Griffies, S.M., Lee, H.C., Pacanowski, R.C. and Vecchi, G.A., 2012. Simulated climate and climate change in the GFDL CM2. 5 high-resolution coupled climate model. *Journal of Climate*, *25*(8), pp. 2755-2781.

Dong, C., Nencioli, F., Liu, Y. and McWilliams, J.C., 2011. An automated approach to detect oceanic eddies from satellite remotely sensed sea surface temperature data. *Geoscience and Remote Sensing Letters, IEEE*,*8*(6), pp. 1055-1059.

Faghmous, J.H., Styles, L., Mithal, V., Boriah, S., Liess, S., Kumar, V., Vikeb, F. and Mesquita, M.D.S., 2012, October. Eddyscan: A physically consistent ocean eddy monitoring application. In *Intelligent Data Understanding (CIDU), 2012 Conference on* (pp. 96-103). IEEE.

Ferrari, R. and Wunsch, C., 2008. Ocean circulation kinetic energy: Reservoirs, sources, and sinks. *Annual Review of Fluid Mechanics*, *41*(1), p. 253.

Frenger, I., Gruber, N., Knutti, R. and Münnich, M., 2013. Imprint of Southern Ocean eddies on winds, clouds and rainfall. *Nature Geoscience*,*6*(8), pp. 608-612.

Griffies, S.M., Winton, M., Anderson, W.G., Benson, R., Delworth, T.L., Dufour, C.O., Dunne, J.P., Goddard, P., Morrison, A.K., Rosati, A. and Wittenberg, A.T., 2015. Impacts on ocean heat from transient mesoscale eddies in a hierarchy of climate models. *Journal of Climate*, *28*(3), pp. 952-977.

Hausmann, U. and Czaja, A., 2012. The observed signature of mesoscale eddies in sea surface temperature and the associated heat transport. *Deep Sea Research Part I: Oceanographic Research Papers*, *70*, pp. 60-72.

Hong, S.Y., Noh, Y. and Dudhia, J., 2006. A new vertical diffusion package with an explicit treatment of entrainment processes. *Monthly Weather Review*, *134*(9), pp.2318-2341.

Iizuka, S., 2010. Simulations of wintertime precipitation in the vicinity of Japan: sensitivity to fine-scale distributions of sea surface temperature. *Journal of Geophysical Research: Atmospheres (1984–2012)*, *115*(D10).

Jin, X., Dong, C., Kurian, J., McWilliams, J.C., Chelton, D.B. and Li, Z., 2009. SST-wind interaction in coastal upwelling: Oceanic simulation with empirical coupling. *Journal of Physical Oceanography*, *39*(11), pp. 2957-2970.

Kanamitsu, M., Ebisuzaki, W., Woollen, J., Yang, S.K., Hnilo, J.J., Fiorino, M. and Potter, G.L., 2002. NCEP-DOE AMIP-II Reanalysis (R-2). *Bulletin of the American Meteorological Society*, *83*(11), pp. 1631-1643.

Kang, D. and Curchitser, E.N., 2013. Gulf Stream eddy characteristics in a high-resolution ocean model. *Journal of Geophysical Research: Oceans*, *118*(9), pp. 4474-4487.

Köhler, M., Ahlgrimm, M. and Beljaars, A., 2011. Unified treatment of dry convective and stratocumulus-topped boundary layers in the ECMWF model. *Quarterly Journal of the Royal Meteorological Society*, *137(654)*, pp.43-57.

Lambaerts, J., Lapeyre, G., Plougonven, R. and Klein, P., 2013. Atmospheric response to sea surface temperature mesoscale structures. *Journal of Geophysical Research: Atmospheres*, *118*(17), pp. 9611-9621.

Lindzen, R.S. and Nigam, S., 1987. On the role of sea surface temperature gradients in forcing low-level winds and convergence in the tropics. *Journal of the Atmospheric Sciences*, *44*(17), pp. 2418-2436.

Liu, W.T., Xie, X. and Niiler, P.P., 2007. Ocean-atmosphere interaction over Agulhas Extension meanders. *Journal of Climate*, *20*(23), pp. 5784-5797.

Liu, Y., Dong, C., Guan, Y., Chen, D., McWilliams, J. and Nencioli, F., 2012. Eddy analysis in the subtropical zonal band of the North Pacific Ocean. *Deep Sea Research Part I: Oceanographic Research Papers*, *68*, pp. 54-67.

Ma, J., H. Xu, C. Dong, P. Lin, and Y. Liu (2015), Atmospheric responses to oceanic eddies in the Kuroshio Extension region, *Journal of Geophysical Research: Atmospheres*, *120*, pp. 6313–6330.

Ma, X., Chang, P., Saravanan, R., Montuoro, R., Hsieh, J.S., Wu, D., Lin, X., Wu, L. and Jing, Z., 2015. Distant Influence of Kuroshio Eddies on North Pacific Weather Patterns?. *Scientific reports*, *5*.

Maloney, E.D. and Chelton, D.B., 2006. An assessment of the sea surface temperature influence on surface wind stress in numerical weather prediction and climate models. *Journal of Climate*, *19*(12), pp. 2743-2762.

Minobe, S., Kuwano-Yoshida, A., Komori, N., Xie, S.P. and Small, R.J., 2008. Influence of the Gulf Stream on the troposphere. *Nature*, *452*(7184), pp. 206-209.

Minobe, S., Miyashita, M., Kuwano-Yoshida, A., Tokinaga, H. and Xie, S.P., 2010. Atmospheric response to the gulf stream: seasonal variations. *Journal of Climate*, *23*(13), pp. 3699-3719.

Okubo, A., 1970. Horizontal dispersion of floatable particles in the vicinity of velocity singularities such as convergences. *Deep Sea Research and Oceanographic Abstracts*, *17(3)*, pp. 445-454.

Omand, M.M., D'Asaro, E.A., Lee, C.M., Perry, M.J., Briggs, N., Cetinić, I. and Mahadevan, A., 2015. Eddy-driven subduction exports particulate organic carbon from the spring bloom. *Science*, *348*(6231), pp. 222-225.

O'Neill, L.W., Chelton, D.B., Esbensen, S.K. and Wentz, F.J., 2005. High-resolution satellite observations of SST modification of the marine atmospheric boundary layer over the Agulhas Return Current. *Journal of Climate*, *18*, pp. 2706-2723.

O'Neill, L.W., Esbensen, S.K., Thum, N., Samelson, R.M. and Chelton, D.B., 2010. Dynamical analysis of the boundary layer and surface wind responses to mesoscale SST perturbations. *Journal of Climate*, *23*(3), pp. 559-581.

O'Reilly, C.H. and Czaja, A., 2015. The response of the Pacific storm track and atmospheric circulation to Kuroshio Extension variability. *Quarterly Journal of the Royal Meteorological Society*, *141*(686), pp. 52-66.

Park, K. and Cornillon, P.C., 2002. Stability-induced modification of sea surface winds over Gulf Stream rings. *Geophysical Research Letters*, *29*(24).

Park, K., Cornillon, P. and Codiga, D.L., 2006. Modification of surface winds near ocean fronts: Effects of Gulf Stream rings on scatterometer (QuikSCAT, NSCAT) wind observations. *Journal of Geophysical Research: Oceans (1978–2012)*, *111*(C3).

Perlin, N., De Szoeke, S.P., Chelton, D.B., Samelson, R.M., Skyllingstad, E.D. and O'Neill, L.W., 2014. Modeling the Atmospheric Boundary Layer Wind Response to Mesoscale Sea Surface Temperature Perturbations. *Monthly Weather Review*, *142*(11), pp. 4284-4307.

Putrasahan, D.A., Miller, A.J. and Seo, H., 2013. Isolating mesoscale coupled ocean–atmosphere interactions in the Kuroshio Extension region. *Dynamics of Atmospheres and Oceans*, *63*, pp. 60-78.

Reynolds, R.W., Rayner, N.A., Smith, T.M., Stokes, D.C. and Wang, W., 2002. An improved in situ and satellite SST analysis for climate. *Journal of Climate*, *15*(13), pp. 1609-1625.

Rouault, M., Reason, C.J.C., Lutjeharms, J.R.E. and Beljaars, A.C.M., 2003. Underestimation of latent and sensible heat fluxes above the Agulhas Current in NCEP and ECMWF analyses. *Journal of Climate*, *16*(4), pp. 776-782.

Saha, S., Moorthi, S., Pan, H.L., Wu, X., Wang, J., Nadiga, S., Tripp, P., Kistler, R., Woollen, J., Behringer, D. and Liu, H., 2010. The NCEP climate forecast system reanalysis. *Bulletin of the American Meteorological Society*,*91*(8), pp. 1015-1057.

Seo, H., Murtugudde, R., Jochum, M. and Miller, A.J., 2008. Modeling of mesoscale coupled ocean–atmosphere interaction and its feedback to ocean in the western Arabian Sea. *Ocean Modelling*, *25*(3), pp. 120-131.

Shchepetkin, A.F. and McWilliams, J.C., 2005. The regional oceanic modeling system (ROMS): a split-explicit, free-surface, topography-following-coordinate oceanic model. *Ocean Modelling*, *9*(4), pp. 347-404.

Sherwood, S.C., Bony, S. and Dufresne, J.L., 2014. Spread in model climate sensitivity traced to atmospheric convective mixing. *Nature*, *505*(7481), pp. 37-42.

Shimada, T. and Minobe, S., 2011. Global analysis of the pressure adjustment mechanism over sea surface temperature fronts using AIRS/Aqua data. *Geophysical Research Letters*, *38*(6).

Skyllingstad, E.D., Vickers, D., Mahrt, L. and Samelson, R., 2007. Effects of mesoscale sea-surface temperature fronts on the marine atmospheric boundary layer. *Boundary-Layer Meteorology*, *123*(2), pp. 219-237.

Small, R.J., Bacmeister, J., Bailey, D., Baker, A., Bishop, S., Bryan, F., Caron, J., Dennis, J., Gent, P., Hsu, H.M. and Jochum, M., 2014. A new synoptic scale resolving global climate simulation using the Community Earth System Model. *Journal of Advances in Modeling Earth Systems*, *6*(4), pp. 1065-1094.

Small, R.J., Xie, S.P., O'Neill, L., Seo, H., Song, Q., Cornillon, P., Spall, M. and Minobe, S., 2008. Air–sea interaction over ocean fronts and eddies. *Dynamics of Atmospheres and Oceans*, *45*(3), pp. 274-319.

Song, Q., Cornillon, P. and Hara, T., 2006. Surface wind response to oceanic fronts. *Journal of Geophysical Research: Oceans (1978–2012)*, *111*(C12).

Spall, M.A., 2007. Midlatitude wind stress-sea surface temperature coupling in the vicinity of oceanic fronts. *Journal of Climate*, *20*(15), pp. 3785-3801.

de Szoeke, S.P. and Bretherton, C.S., 2004. Quasi-Lagrangian large eddy simulations of cross-equatorial flow in the east Pacific atmospheric boundary layer. *Journal of the Atmospheric Sciences*, *61*(15), pp. 1837-1858.

Taguchi, B., Nakamura, H., Nonaka, M. and Xie, S.P., 2009. Influences of the Kuroshio/Oyashio Extensions on Air-Sea Heat Exchanges and Storm-Track Activity as Revealed in Regional Atmospheric Model Simulations for the 2003/04 Cold Season. *Journal of Climate*, *22*(24), pp. 6536-6560.

Vecchi, G.A., Xie, S.P. and Fischer, A.S., 2004. Ocean-Atmosphere Covariability in the Western Arabian Sea. *Journal of Climate*, *17*(6), pp. 1213-1224.

Waliser, D.E., Moncrieff, M.W., Burridge, D., Fink, A.H., Gochis, D., Goswami, B.N., Guan, B., Harr, P., Heming, J., Hsu, H.H. and Jakob, C., 2012. The "year" of tropical convection (May 2008-April 2010): Climate variability and weather highlights. *Bulletin of the American Meteorological Society*, *93*(8), pp. 1189-1218.

Weiss, J., 1991. The dynamics of enstrophy transfer in two-dimensional hydrodynamics. *Physica D: Nonlinear Phenomena*, *48*(2), pp. 273-294.

White, W.B. and Annis, J.L., 2003. Coupling of extratropical mesoscale eddies in the ocean to westerly winds in the atmospheric boundary layer. *Journal of Physical Oceanography*, *33*(5), pp. 1095-1107.

Xie, S.P., 2004. Satellite observations of cool ocean-atmosphere interaction. *Bulletin of the American Meteorological Society*, *85*(2), pp. 195-208.

Yi, J., Du, Y., He, Z. and Zhou, C., 2014. Enhancing the accuracy of automatic eddy detection and the capability of recognizing the multi-core structures from maps of sea level anomaly. *Ocean Science*, *10*(1), pp. 39-48.

Yu, L. and Weller, R.A., 2007. Objectively analyzed air-sea heat fluxes for the global ice-free oceans (1981-2005). *Bulletin of the American Meteorological Society*, *88*(4), pp. 527-539.

Zhang, Z., Wang, W. and Qiu, B., 2014. Oceanic mass transport by mesoscale eddies. *Science*, *345*(6194), pp. 322-324.